

MAGNETIC ANALYSIS OF REACTIONS LEADING TO
EXCITED STATES IN Li^6 AND B^{11}

Thesis by
David Eiben Groce

In Partial Fulfillment of the Requirements
For the Degree of
Doctor of Philosophy

California Institute of Technology
Pasadena, California

1963

ACKNOWLEDGMENTS

The author is happy to express his thanks to all the faculty and technical staff of the Kellogg and Sloan Radiation Laboratories. In particular, special thanks must go to Professor W. Whaling for his guidance and encouragement in this project and especially for his painstaking scrutiny of all the facets of this thesis. To Professor T. Lauritsen, special thanks are also due for the opportunity to first work with him in this laboratory and for the continued interest he has held in this work. Special gratitude goes to Mr. J. McNally for help with many of the experimental details and the long, all-night vigils.

The magnetic spectrometer was not a one-man project. Credit must be given to Professors W. Whaling, T. Lauritsen, and R. W. Kavanagh for much of the initial design work. Mr. V. F. Ehrgott carried through on most of the mechanical design work from the basic ideas presented to him. Mr. A. Bacher made the ray-tracing box and took part in the ray-tracing measurements. Mr. J. McNally built the NMR magnetometer, without which the spectrometer would not have been such a precise instrument; he also made most of the magnetic field profile measurements.

It is a pleasure to give extra special thanks to my wife, Barbara, without whose encouragement, help, and breakfasts at 6:00 a. m. during all-night runs, this thesis would not have been completed. Special thanks go also to Mrs. V. J. Ondrasik for the rough-draft typing.

Thanks for financial assistance go to Convair-Astronautics and General Atomics for fellowship grants during the course of this work, as well as to the Office of Naval Research and the United States Atomic Energy Commission for the actual support of this experiment.

ABSTRACT

A double-focusing magnetic spectrometer of 24-inch radius has been installed at the California Institute of Technology for use with the ONR Tandem Van de Graaff accelerator. The design, alignment, and testing of this instrument is described, and the performance is compared with the theoretical design predictions. A $\text{Be}^9(p, \alpha)\text{Li}^{6*}$ reaction was investigated with this spectrometer. Excited states in Li^6 were seen at 2.19-, 3.57-, 4.50-, and 5.36-MeV, confirming previous work. Intense alpha particle background from the breakup of Li^{6*} , Be^8 , and Be^{9*} limit the information that can be obtained from the alpha particle spectrum. The $\text{Be}^9(\text{He}^3, p)\text{B}^{11*}$ and $\text{B}^{10}(d, p)\text{B}^{11*}$ reactions were used to investigate the excited states in B^{11} . All known states between 8.9- and 15.0-MeV excitation were observed except for states at 11.0- and 14.0-MeV excitation. In addition, two new states were found at 11.27- and 12.57-MeV excitation. It is believed that the 11.27-MeV state has isotopic spin $T = 1/2$ and that the 12.57-MeV state has isotopic spin $T = 3/2$.

TABLE OF CONTENTS

<u>Part</u>	<u>Title</u>	<u>Page</u>
I.	INTRODUCTION	1
II.	MAGNETIC SPECTROMETER	2
	A. Introduction	2
	B. Design Parameters and General Description	5
	C. Magnet Current Electronics	11
	D. Field Measurements	13
	E. Beam Handling Equipment	14
	F. Vacuum Box	15
	G. Spectrometer Entrance Slits	17
	H. Initial Alignment	18
	I. Ray Tracing	20
	J. Target Chamber	26
	K. Final Alignment	28
	L. Detector and Associated Electronics	30
	M. Measurements with Radioactive Sources	31
	N. Relative Calibrations	36
	O. Aberrations	37
	P. Summary	39
III.	EXCITED STATES IN B ¹¹	41
	A. Introduction	41
	B. Experimental Details	44
	C. Results	45
	D. Isotopic Spin Test	46
	E. Q-Value and Width Measurements	48

<u>Part</u>	<u>Title</u>	<u>Page</u>
	F. Angular Distributions	50
	G. Conclusions	50
IV.	EXCITED STATES IN Li^6	52
	A. Introduction	52
	B. Experimental Details	52
	C. Results	53
	D. Coincidence Experiment	54
	E. Conclusions	56
APPENDIX 1:	Performance Characteristics for Magnetic Spectrometer and Its Power Supply	58
APPENDIX 2:	Computer Programs	61
APPENDIX 3:	180° Reactions	63
APPENDIX 4:	Preparation of Beryllium Foils	65
TABLES		68
REFERENCES		80
FIGURES		83

I. INTRODUCTION

With the advent of the 10-MeV tandem accelerator at the California Institute of Technology, additional auxiliary equipment had to be prepared. The design, testing, and alignment of a double-focusing magnetic spectrometer and its auxiliary equipment will be described in Section II of this thesis. The remaining parts of the thesis will be concerned with two of the first experiments performed on this instrument. In these experiments, reactions leading to the highly excited states in B^{11} (Section III), and Li^6 (Section IV), were investigated in hopes of obtaining new information about these two important light nuclei.

II. MAGNETIC SPECTROMETER

A. INTRODUCTION

A 180° , 24-inch radius double-focusing magnetic spectrometer has been recently put in operation as a charged particle analyzer for use with the 12-MeV Office of Naval Research tandem Van de Graaff accelerator. It is the purpose of this section to:

- (1) review the considerations that went into the design of this spectrometer,
- (2) describe the finished magnet and its associated apparatus,
- (3) evaluate the performance of this spectrometer as a laboratory instrument.

The theory on which the design of this spectrometer is based has evolved from 1941 when Kerst and Serber first put forth the proposal that charged particles can be focused in a non-uniform magnetic field. In chronological order the development has been:

1941: Kerst and Serber

Focusing in field of form: $B = B_0(r/r_0)^{-n}$

1946: Siegbahn and Svartholm

Double-focusing with $n = \frac{1}{2}$; source and collector inside field

1947: Shull and Dennison

Expansion of field: $B = B_0 \left(1 - \alpha \left(\frac{r-r_0}{r_0} \right) + \beta \left(\frac{r-r_0}{r_0} \right)^2 + \dots \right)$

First-order double-focusing for $\alpha = \frac{1}{2}$, other coefficients are free to vary

Second order focusing: $\beta = 1/8$ for r focusing

$\beta = 3/8$ for z focusing

1947: Coggeshall

Fringing field corrections for uniform field

1949: Hintenberger

Circular entrances for uniform field magnets

1950: Judd

First-order double-focusing properties for source and collector outside of field

1950: Rosenblum

Second-order double-focusing properties for source and collector outside of field

1957: Judd and Bludman

Consideration of third-order terms, and fringing field

1958: Ikegami

Second-order terms and circular entrances for non-uniform fields

The design of this spectrometer has been primarily based on the work of Ikegami (1958).

Following the evolution of the theory of double-focusing, there have been many spectrometers built which incorporate this concept:

1946: Siegbahn and Svartholm

Double-focusing; source and collector inside field;

angle of deflection = $\sqrt{2} \pi$

- 1950: Snyder, Rubin, Fowler, and Lauritsen
10 $\frac{1}{2}$ -inch radius; source and collector external to field;
angle of deflection = 180°
- 1951: Li, Rubin, and Whaling
16-inch radius; 180°; improved magnetic circuit
- 1955: Rubin and Sachs
12-inch radius; adjustable poles and pole edges for
empirical adjustment of astigmatism and to minimize
aberrations
- 1956: Asaro and Perlman (as discussed by Judd and Bludman)
13.8-inch radius; 180°; field parameters adjusted to
third-order including corrections for fringing field;
 $\alpha = \frac{1}{2}$, $\beta = 0.209$
- 1961: Cohen, Cookson, and Wankling
24-inch radius; adjustable poles; $\alpha = 0.497$, $\beta = 0.23$

Other instruments have been built, but they have been either copies or scaled up versions of the above magnets.

Even today the magnetic spectrometer has many advantages over other types of charged particle detectors, including the newly developed solid-state detectors. The solid-state detector, in fact, has enhanced the usefulness of the spectrometer, since a charged particle detector must be used at the focus of the spectrometer. The combination of the two provides an energy determination in the solid-state detector simultaneously with the momentum resolution of the magnet.

The magnetic spectrometer has the highest resolution that is available. Moreover, it eliminates all particles not within the prescribed resolution limits from the particle detector, and thereby eliminates pileup at high counting rates. At the high excitation energies in nuclei that are available with the tandem accelerator, many decay channels are open. This means that there may be several different reaction products with the same energy or dE/dx to be analyzed. The momentum measurement by the magnet helps to distinguish these particles from each other in conjunction with the conventional detector. The spectrometer has an additional advantage in that the particle detector is located several feet away from the target, so that the background caused by gamma rays and neutrons is negligible while maintaining the same efficiency for charged particles. Compared to the spectrograph, the spectrometer permits coincident detection of the analyzed particle and other radiations. The "live-time" data analysis is also a very desirable advantage of the spectrometer over the spectrograph.

B. DESIGN PARAMETERS AND GENERAL DESCRIPTION

When a spectrometer was first considered for use with the tandem accelerator, there were three specific areas it was felt that it should cover:

- (1) medium energy and solid angle with high resolution,
- (2) large solid angle and low resolution,
- (3) high energy and low solid angle.

Rather than having three separate magnets, a compromise had to be made.

A radius of 24 inches was chosen since the most magnetically rigid particle expected was a 10-MeV triton (312 kilogauss-inches). Also, since the tandem beam is 69 inches above the floor, a greater radius would necessitate laying the magnet on its side. A 180° angle of deflection was chosen since it was the largest angle obtainable if one wished to machine mirror parts at the same time. A large angle of deflection provides higher dispersion, plus shorter image-object distances than a smaller angle of deflection.

The choice of aperture size represents a compromise between several conflicting criteria:

- (1) Aberrations in the focus are proportional to $(R^2 + Z^2)$ where

R is the radial dimension of the aperture and Z is the dimension of the aperture parallel to the field. For minimum aberrations, this implies $R = Z$.

- (2) The magnetic field B is approximately proportional to NI/Z where NI are the ampere turns creating the field.

For lower input power:

$$Z \text{ small}$$

- (3) The useful solid angle is not determined by the full area between the poles since the field at the edges is reduced due to leakage of the field lines. If one assumes that this edge effect extends $\frac{1}{2}$ gap width inward, the solid angle is proportional to $(R-Z)Z$. For the greatest percentage of useful solid angle, this implies

$$Z = \frac{1}{2}R$$

- (4) In most nuclear reactions the energy of the emitted particles varies rapidly with angle. For high resolution, the angle in this direction should be kept small. In this case,

$$Z \text{ small.}$$

However, R also contributes some width (Section II. G.) at all angles except 90° ; therefore

$$R \text{ not "too" large.}$$

With the consideration of all these criteria, an aperture of $R \times Z = 12 \text{ in.} \times 3.5 \text{ in.}$ (nominal; 3.85 in. maximum and 3.14 in. minimum) was chosen. This aperture would give a solid angle of 0.015 steradians (if $9 \frac{3}{4}$ inches are useful in the r direction and the object distance is 26 inches).

The image and object distances are related by Judd's (1950) first order formula:

$$\tan^{-1}(\sqrt{.5} d_o / r_o) + \tan^{-1}(\sqrt{.5} d_{r,z} / r_o) = (1 - \sqrt{.5})\pi$$

where d_o is the object distance and $d_{r,z}$ is the r or z image distance (angle of deflection = 180° and $\alpha = \frac{1}{2}$). In choosing the object-image distances, there are again several conflicting criteria to consider:

- (1) It is desirable to have the detector assembly outside of the magnet coils because of space limitations. This means

$$d_{z,r} > 7 \text{ inches.}$$

If a scintillation crystal and a photo-multiplier are used as the detector (e. g., to detect 20-MeV protons), the photo-tube must be shielded from the magnetic field. If one wishes to avoid the use of a light-pipe, it is desirable to

locate the scintillator and photo-tube outside the stray field:

$$d_{r,z} \geq 11 \text{ inches for } B/B_0 \leq 1\% .$$

- (2) The solid angle Ω is related to the object distance d_0 by Judd's (1950) formula:

$$\Omega = \frac{Z R}{(2 r_0^2 + d_0^2)}$$

where r_0 is the mean bending radius. Thus, for a large solid angle:

$$d_0 \text{ small .}$$

- (3) It is important to be able to detect particles emitted at large backward angles. With the configuration used for the target chamber, no angle greater than 155° is possible. In order that the beam pipe clear the side of the magnet, it follows that

$$d_0 \geq -\frac{1}{2}W \tan(155^\circ)$$

where W = width of magnet.

With a $3 \frac{1}{2}$ inch slot cut into the side of the magnet, and with $d_0 = 26.2$ inches, the full back angle of 155° could be realized. This sets the image distance at 9.0 inches (2 inches beyond the coils, and where $B/B_0 \sim 2\%$). However, the magnet support allows one to set d_0 at any value between 9.0 inches and 26.2 inches.

If one expands the magnetic field as Shull and Dennison (1947),

$$B = B_0 \left(1 - \alpha \left(\frac{r-r_0}{r_0} \right) + \beta \left(\frac{r-r_0}{r_0} \right)^2 + \dots \right) \quad (1)$$

$\alpha = \frac{1}{2}$ is required for double-focusing. For $\alpha = \frac{1}{2} + \epsilon$, the resulting astigmatism is

$$d_r - d_z \sim 150 \text{ } \epsilon \text{ .}$$

A small amount of astigmatism is not objectionable since a line detector may be used at the r focus. A tolerance of ± 0.02 was placed on α ; this limits the astigmatism to be less than 3 inches; the z width at the r focus would be less than 0.2 inches.

$$\alpha = 0.50 \pm 0.02$$

To pick values for the remaining parameters, we must turn to the analysis of Ikegami (1958). He considers a field of the form given by equation (1), but adds a circular entrance and exit to the field. This is similar to the treatment by Hintenberger (1949) for uniform fields. The aberration δr in the r direction is given for a point source by:

$$\delta r = M_{11} \bar{\phi}^2 + N_{11} \Theta^2 \text{ ;}$$

$\bar{\phi}$ is the angle of the deviation of a ray from the mean ray in the direction perpendicular to the field,

Θ is the angle of the deviation of a ray from the mean ray in the direction parallel to the field,

δr is the displacement at the focus of the ray that leaves the target spot at angles Θ and $\bar{\phi}$ with respect to the mean ray.

N_{11} depends on the field parameters α and β plus other fixed parameters (angle of deflection; image and object distances), but not on the radii of the entrance or exit pole tips. M_{11} , on the other hand, does depend on these radii as well as on the other parameters. The aberrations due to N_{11} and M_{11} are plotted versus β for the design values of the other parameters in Figure 1. From the figure it is obvious that the aberration due to N_{11} is zero for $\beta = 0.34$. The ability to design pole pieces that would yield the desired value of β is

very difficult and no commercial supplier would undertake to guarantee β to a high degree of precision. However, the tolerance of β need not be as strict as the one on α since at the edges of the field $|\frac{r-r_o}{r_o}| \sim 1/5$. Thus any uncertainty in β is only 1/5 as effective in changing the field from the "ideal shape" as the uncertainty in α , and thus the tolerance on β may be five times as large:

$$\beta = 0.34 \pm 0.10.$$

Having picked β , the only other adjustable parameters left are the radii of the entrance and exit pole tips. For a $\beta = 0.34$ and a pole tip radius of 14.5 inches, M_{11} goes to zero. However, some empirical adjustment is desirable to correct discrepancies that may develop between the theory and the actual fabricated instrument. To achieve this, the pole tips were made on separate removable pieces in such a manner that radii could be changed if necessary after testing the instrument (see Figure 3). The field parameters α and β were to be optimized at a field of 10 kilogauss. It was felt that with Armco iron pole faces the effects of saturation would not distort the profile at lower fields. With 10 kilogauss at the mean orbit, the field at the inner radius is approximately 11 kilogauss.

An additional feature desired was a removable slot in the rear to allow for the possibility of observations at angles near 180° . This requirement is discussed in Appendix 3.

Since the California Institute of Technology does not have provision for machining and grinding of heavy steel pieces up to 8 feet in diameter, it was decided to seek an outside supplier. Spectromagnetic Industries of Hayward, California was selected on the basis of bidding

and experience. The specifications are given in Appendix 1.

The general appearance of the magnet (see Figures 2 and 3) is that of half of a cylinder 86 1/4 inches in diameter and 38 3/4 inches thick. The kidney-shaped coils surround the pole pieces and lead to a current and water manifold on the top. Three adjustable studs, which support the magnet, are located on the radial carriage which provides motion to and from the axis of rotation. The radial carriage rests on rollers that are placed on top of the main support carriage. This support carriage is pivoted at the axis of rotation in a self-aligning thrust bearing and is supported above a circular track by two 12-inch diameter wheels. The track has been bolted and grouted to the floor. Additional details will be presented in Section II. H.

C. MAGNET CURRENT ELECTRONICS

The magnetic field is produced by thirty-two coils of six turns each. These coils are made of 0.467-inch square copper tubing with a 0.184-inch diameter hole in the middle. These coils are connected in series such that the maximum current of 800 amperes produces a magneto-motive force of 150,000 ampere-turns. The total resistance is 0.141 Ω ; thus, the total power dissipated is 90 kilowatts at full load. Sixteen gallons per minute of cooling water is provided to cool the magnet. In the water cooling circuit, the thirty-two coils are connected in parallel by means of insulating hoses. A pressure drop of 50 pounds per square inch across the magnet produces a total flow of 16 gallons per minute. At full load the temperature rise is 50°F. The current is fed to the magnet through six flexible welding cables from a 100-kW generator powered by a 100-horsepower induction motor. See Figure 4

for details.

The current to the magnet passes through an oil-filled, water-cooled resistor. This resistor consists of seventy-four parallel 21-inch lengths of No. 10 Manganin wire. Manganin was chosen because of its low temperature coefficient.

The voltage drop across this resistor is compared with a voltage supplied from a set of heated mercury reference cells. The difference signal is amplified through a Brown chopper-amplifier and fed to a phase-sensitive rectifier which supplies the exciting field for the amplidyne generator. The amplidyne supplies the exciting field for the 100-kilowatt generator. The amplidyne output is also fed to a derivative feedback amplifier which prevents rapid changes of the amplidyne output voltage.

The current regulation ($\Delta I/I$) was initially 1/350 to 1/2000. The trouble was traced to the fact that thirty-four of the Manganin wires in the regulation resistors were not soldered into place. After this was corrected, the regulation was 1/3100 to 1/26,000 with ΔI approximately a constant.

Numerous safety devices are incorporated in the circuitry to protect the magnet, the M-G set, electronics, etc. These include (see Figure 4):

- (1) AC current overload,
- (2) DC current overload (> 800 amperes),
- (3) insufficient water for cooling (< 10 gallons/minute),
- (4) thermo-switches on each coil ($> 58^{\circ}\text{C}$),
- (5) reference cell heater not on,
- (6) operation of reversal switch with load on.

D. FIELD MEASUREMENTS

Measurements of the magnetic field profile were made to test its conformance to specifications and to permit the comparison of theory and performance. These measurements were made with a Hall emf generator (see, for example, Zingery 1961) with its temperature stabilized to 0.1°C . The accuracy of these measurements was limited by the poor current regulation in the magnet due to the poorly constructed sensing resistor.

The fringing field at the entrance to the magnet was measured in the plane $z = 0$, perpendicular from the face of the magnet for several values of r ($r = 21, 22, 23, 24, 25, 25$, and 27 inches). Each measurement was referenced to a common point to minimize the uncertainty due to the poor current regulation. The result for $r = r_0 = 24$ inches is presented in Figure 5. This result was used to determine the path of the mean ray ($r = r_0$) through the fringing field and thereby fix position of the magnet with respect to the target position. The face of the magnet must be tipped backward 4.8° from vertical and lowered $5/16$ inch as shown in Figure 5.

After removing the $r^{-\frac{1}{2}}$ dependence of the field at various values of r , lines of constant field had approximately the radius of the curved entrance pole tip. This method is not very accurate, but at least it offers some encouragement that the field strength follows the iron boundaries.

The field profile was measured by Spectromagnetic Industries. The results are shown in Figure 6 along with the pole piece profile (see also Table 1). The data measured is in terms of the logarithmic

derivative:

$$-\frac{r_o}{B(r)} \frac{\partial B}{\partial r}.$$

This measurement was made by a triple flip coil arrangement, and it readily gives α and β at $r = r_o$ (as shown in Table 2). The field profile was measured at three fields -- 6, 10, and 12.5 kilogauss-- and at three different places (the 85° and the two 45° ports).

The field was also measured at $r = r_o$ as a function of angle. It proved to be constant to $\pm 1/2000$ to within four gap widths of the entrances. A previously-measured mechanical runout in the gap width of 0.013 inches at the entrance has been removed with 0.001-inch shims placed in a stair-step fashion.

The field profile was remeasured after the magnet was installed at the California Institute of Technology at only the 85° port. With the Hall probe, the true field profile was measured at four different fields; 3.2, 6.3, 8.5, and 11.3 kilogauss; with and without the stainless steel vacuum box (see Section II. F.) in place. These results are also presented in Figure 6. Notice the distortion of the profile due to saturation at 11.3 kilogauss. Results of a least squares analysis for α and β over the useful range of the profile are presented in Table 2. Little or no difference was caused by the presence of the vacuum box.

E. BEAM HANDLING EQUIPMENT

The apparatus used to deliver the beam from the tandem switching magnet to the target chamber is shown in Figure 3. Only a few points need be discussed, since the components are reasonably standard.

The quadrupole lens is a standard, two-element magnetic lens (Enge 1959) obtained from High Voltage Engineering Corporation. The

lens will focus the diverging beam into a spot on the target. With help of steering magnets, this beam can be made to go through both sets of beam defining slits; thus, the maximum size of the beam spot and the direction in which the beam enters the target chamber are fixed. The beam is intercepted during unwanted periods by the beam chopper to save the targets and reduce background. The vacuum system is shown schematically in Figure 7, and the characteristics of its components are shown in Table 3.

F. VACUUM BOX

Several proposals were made for the vacuum chamber between the poles of the magnet:

- (1) Non-magnetic plates could be welded to the pole pieces to form a box in which the pole pieces compose two sides. This has the serious disadvantage that the welding will stress the pole pieces and tend to pull them together. This displacement of the poles could distort the field considerably.
- (2) O-ring seals between the pole pieces and added side plates would be very difficult to achieve. This seal would extend for 14 feet over surfaces that are not accessible for inspection. By having the entrance and exit pole tips removable, any vacuum seal would be uncertain.
- (3) A thin-walled box with walls glued to the pole faces was considered. To obtain a reliable bond between two large metal surfaces would require curing at elevated temperatures. The box would be fragile and subject to damage during installation, and once installed it could not be removed.

- (4) A heavy-walled box would overcome the objections mentioned above, but would reduce the useful solid angle. To achieve the largest solid angle one must consider two conflicting criteria. First, the thickness of the sides between the pole pieces will reduce the solid angle; therefore, they should be as thin as possible. Second, if these pieces are too thin, atmospheric pressure will deflect them inward further reducing the solid angle. It was determined that 7/32-inch thick stainless steel would have the smallest total reduction of the solid angle (thickness plus deflection due to atmospheric pressure). The final cross section is shown in Figure 8.

The vacuum box was constructed out of 304L low carbon stainless steel. This type of steel has a very low tendency to form carbides and quasi-martensite at elevated temperatures (Scharschu, 1935), i. e., during welding. This is desirable to prevent formation of any residual magnetic material in the weld. The field measurements previously mentioned detected little or no effect on the field due to the welds. The box was welded in a heavy jig and stress relieved in a furnace before the jig was removed.

Baffles to reduce the scattering of particles that strike the walls of the vacuum box were installed just outside the extreme stable orbits as shown in Figure 8. The baffles are made by soft soldering tabs of 0.016-inch thick phosphor-bronze to a long (64.8 inches on the inside radius and 95.2 inches on the outside) strip of phosphor-bronze. The strips were inserted inside the vacuum box and fastened at both ends

with screws. The strips are flexible for installation but rigid enough to be supported in place by the screws at the ends. Phosphor-bronze was chosen because of its mechanical and magnetic properties.

The path lengths from the target through the vacuum box to the detector are

- 2.53 meters for the inner orbit,
- 2.81 meters for the mean orbit,
- 3.13 meters for the outer orbit.

These distances are needed in the calculation of flight time through the spectrometer for coincidence experiments.

G. SPECTROMETER ENTRANCE SLITS

Figure 9 shows the spectrometer entrance slit assembly. It is composed of four independently pivoted 0.020-inch thick tantalum pieces. Using the coarse and fine adjustments, a slit may be reproducibly set by the slit angle reading. These readings may be converted to true degrees from the target center by means of Figure 10. Table 4 gives the numerical conversions for these readings. By independently setting each of the four slits, a rectangle of any size may be positioned anywhere in front of the spectrometer aperture.

The slits were initially set with an alignment telescope centered on the slit box. This, however, was not completely accurate in the case of the ϕ slits since the height is subject to the positioning of the magnet. After the spectrometer had been aligned (see Section II. H.) and all apparatus installed, the zeros were established by means of the beam.

With the spectrometer set at 0° , the beam from the accelerator was allowed to pass through a pin hole of ≤ 0.005 inches diameter at the

target position. For these measurements, neither the quadrupole lens nor the steering magnets were used. The beam was observed on a quartz plate at the image of the spectrometer. The Φ slits were individually closed until the beam was cut off. The top slit read $+0^{\circ} 50'$ at cutoff (true angle $+0.2^{\circ}$); the bottom slit read $-1^{\circ} 10'$ at cutoff (true angle -0.2°).

Then the Θ slits were each set at $+0^{\circ} 30'$ (true angle 0.066°), and the magnet was rotated to locate the angles at which the spot on the quartz was cut off. The track readings were -0.28° and -0.10° at cut off. The window observed with the protractor is larger than the setting of the slits by the size of the beam spot. The center of this window defined by the Θ slits corresponds to an angle that differs from the fiducial mark on the protractor by -0.19° . The Θ slits were each set at $+0^{\circ} 15'$; the beam now came through centered at -0.20° on the protractor. The spectrometer is capable of being set reproducibly to 3 minutes.

At all angles except 90° , the width of the aperture in the Φ direction contributes to the width in the Θ direction, as shown in Figure 11 and tabulated in Table 5. A knowledge of this is important when calculating the kinematic broadening of a line.

H. INITIAL ALIGNMENT

Before the magnet could be aligned into proper position, a certain amount of preparation and modification of the support was necessary.

The central self-aligning thrust bearing was fixed into place at a hole through the floor on the north 20° targetleg as shown in Figure 12. The circular track was centered about the bearing with a runout on

the protractor scale of ± 0.003 inches and bolted into place a distance of one inch above the floor. Its height from the floor was adjusted within $\pm .005$ inches with a sensitive level referenced to the center bearing. Embeco grout was tapped into place under the track. After the grout had cured, the vertical runout of the track is shown in Figure 13. The increased runout of ± 0.015 inches was apparently caused by forcing the grout under the track unevenly; this runout was enough to demand a modification to the support carriage.

The supports for the two 12-inch diameter wheels were modified as shown in Figure 12 to allow the support carriage to be raised or lowered with respect to the wheels. The fineness of the adjustment is such that one turn of the adjustment screw changes the height by 0.040 inches. Twenty-second (20") level vials were installed on each side of the magnet on lines parallel to the axles of the wheels. These levels in conjunction with the variable wheel supports enable one to correct the effects of the vertical runout of the track.

When the level bubbles are centered, the support carriage and consequently the magnet has the same orientation with respect to the central bearing, independent of the rotational angle. The central bearing is assumed fixed, but calculations indicate that the floor will settle a maximum of 0.050 inches over a long period of time. This motion can be compensated by lowering the beam entrance slits or by raising the magnet on its carriage. Figure 13 shows the effects of the uneven track on the positioning of the target chamber with and without the correction available with the levels and variable wheel supports.

Shimming and remachining of several parts helped to flatten out

the critical surfaces of the carriages which were received in a severely warped condition. These places are indicated in Figure 12.

From the fringing field measurement, the orientation of the magnet was determined, i. e., to be tipped back 4.8° and lowered $5/16$ inch with respect to the beam line (69 inches from the floor). The height was set with a transit referenced to fixed bench marks on the walls of the target room. The backward tip was set with an adjustable incline level to $4.80 \pm 0.08^\circ$. The magnet was set perpendicular and square to a plumb line running through the center of the support bearing to within $\pm 1/64$ inch. The design value of 26.2" for the object distance could not be realized because the magnet hit the rear of the support carriage at $25 \frac{49}{64}$ inches. This was the value adopted for d_o . The jack screws were sealed to prevent any unauthorized movement.

The vacuum box was positioned between the poles by loosening the bolts that hold the magnet together while pushing the pieces apart with three pusher bolts. A gap of $1/4$ inch was all the clearance necessary to allow for easy placement of the vacuum box. The box was so positioned that the entrance face was vertical. This positioning was asymmetrical with respect to the magnet (4.8° at the entrance and 5.2° at the exit) but did no harm. Additional information will be presented in Section II. K.

I. RAY TRACING

The techniques for the measurement of the ion optic properties of magnetic devices have evolved into a very accurate method. The evolution has been:

1946: Siegbahn and Svartholm

Radioactive deposit on screen as source; film at the image position.

1950: Snyder, Rubin, Fowler, and Lauritsen

AC magnet at the object position; beam size and position observed on a quartz at the image.

1951: Crane

Lambertson

Stretched current-carrying wire to simulate particle trajectories.

1960: Alvarez, Brown, Panofsky, and Rockhold

Deflection magnet and beam as point source with a quartz at the image to find the emerging beam spot.

1961: Westermarck

Radioactive source retarded and advanced by potential to give dispersion on film at the image.

1961: Wolicki and Knudson

Deflection magnet as point source with slit and quartz to find emerging beam axis; dispersion measurement by varying magnet field for fixed beam momentum.

The technique used on this spectrometer was that of Wolicki and Knudson (1961).

An auxiliary bending magnet with $4\frac{3}{8}$ -inch diameter poles spaced $1\frac{1}{16}$ inch apart was placed at the target position, as shown in Figure 14. A piece of $1\frac{1}{2} \times 1$ -inch copper wave guide connected with

bellows formed the vacuum link through the auxiliary magnet from the beam pipe to the spectrometer entrance slits.

By this time, a proton nuclear magnetic resonance magnetometer had been installed to measure the spectrometer field. The inhomogeneous portion of the field was cancelled out by using four direct-current compensating coils as described by Vincent, King, and Rowles (1959). This magnetometer, with two different probe heads, covers the range of magnetic fields from approximately 2 kilogauss to 10 kilogauss. The locations for these are shown in Figure 8. Outside of this range, a controlled-temperature Hall emf generator is used (Zingery, 1961).

In order to locate the emerging beam at the image, a box was constructed that incorporated two slits and a quartz plate. The r slit was a horizontal slit formed from two pieces of tantalum, 0.020 inch apart, located 8.54 inches from the magnet exit, as shown in Figure 15. Its position relative to the top of the box could be measured to 0.002 inches with a height gauge. The z slit was a vertical slit located 7.90 inches from the pole ends. An $1/8$ -inch thick quartz plate, 6×1 inch, was located 14.92 inches from the exit. The position of the beam spot on the quartz could be measured relative to the top of the box with a depth gauge to better than $\pm 1/64$ inch.

With the quadrupole lens off, the defining slits (see Figure 14) will produce a parallel bundle of particle rays from the tandem accelerator. The bundle of rays can be deflected up or down along paths which diverge from a point source by means of the cylindrically-symmetric auxiliary magnetic field. Simple geometrical considerations show that

if the beam enters the auxiliary field radially it will also leave radially. Thus, a point source can be generated one ray at a time. The spectrometer slits can be used to determine the angle at which the ray enters the spectrometer. At the image of the spectrometer, the combination of the slit and quartz measurements will determine the axis of the emerging ray, as shown schematically in Figure 15. With the assumption of straight particle paths beyond the slit ($B/B_0 < 3\%$), a series of ray diagrams may be plotted.

It is desirable to measure the ion optic properties of the spectrometer at several different fields; thus, the following beams and nominal fields were chosen:

2.0-MeV protons	-	3.37 kilogauss
2.0-MeV α^+	-	6.71 kilogauss
3.0-MeV α^+	-	8.22 kilogauss
4.5-MeV α^+	-	10.03 kilogauss
5.5-MeV α^+	-	11.13 kilogauss .

The central ray at $r = r_0$ was found by introducing a rod through the 85° port of the magnet, and by varying the magnetic field until the image of the beam on the quartz plate showed the shadow of the tip of the rod. Now with the spectrometer field set, the auxiliary magnet was varied to generate different rays. The entrance angle was measured, and resulting foci were determined and plotted as in Figures 16 and 17.

After determining the focal point for a given field, the spectrometer field was changed by a known amount and the new focal point found; note that this has the same effect as leaving the field fixed and changing the incident beam momentum. In this way, the focal plane may be generated as shown in Figures 18, 19, and 20.

With the auxiliary magnet off, or set to a fixed value, the spectrometer could be rotated about the target axis to locate the z foci as shown in Figure 21.

The results from the ray tracing with the 14.5-inch radius pole tips (Figures 16 and 18) were quite enlightening. One can readily see that the extreme rays ($\theta \sim 5.1^\circ$) are deflected too much and thus intersect off of the mean orbit towards smaller values of r . The obvious solution was to reduce the radius of the pole tips so that these rays would be in the full magnetic field for a shorter distance. Pole tips shims that reduced this radius to 9 inches were tried, producing the desired effect. With this encouragement, the removable pole tips were cut back to a 9-inch radius (the smallest radius allowed by the 12-inch width of the pole pieces). The results for the 9-inch radius pole tips are presented in Figures 17, 18, 19, and 20. Table 6 compares the focal points and diameters of the circles of least confusion for both the 9-inch and 14.5-inch radii. On the whole, the 14.5-inch foci appear to have the smaller circles of confusion, but the maximum entrance angles obtained are only $\sim 5.1^\circ$ compared with $\sim 5.8^\circ$ obtained with the 9-inch radius. Comparing equal deflection angles, the 9-inch radius gives smaller aberrations than the 14.5-inch radius. The best focus was obtained at 10 kilogauss in accord with design specifications.

The focal planes are shown in Figures 18, 19, and 20. One can calculate the tip of these planes from perpendicular to the mean orbit by the approximate formulas given by Judd and Bludman (1957). The calculated result of 57° disagrees with the measured result of $48 \pm 3^\circ$. This discrepancy may be due to the reason that Judd and Bludman

neglect the fringing field and consider only the case of equal image and object distances.

From the z foci shown in Figure 21 and summarized in Table 6, it is apparent that there is approximately 1.9 inches of displacement between the r and z foci. This is close to the value of 2.06 inches calculated from the difference $(\alpha - \frac{1}{2})$. This astigmatism will not cause any undesirable effects, since the rays have only diverged less than 0.1 inches by the time they reach the r focus.

The dispersion D of the spectrometer is defined by Judd (1950) as:

$$D = \frac{\delta r / r_o}{\delta p / p} ,$$

where δr is the distance a ray moves when its momentum p is changed by an amount δp . The dispersion is quite important to know, since it relates the momentum resolution $\delta p / p$ to the detector slit size. Figure 22 shows a typical dispersion measurement along with the results at other fields. The dispersion shows a slow increase to 10 kilogauss with a fall off at higher fields. The predicted momentum and energy resolutions for various detector slit sizes are shown in Table 7. Aberrations will reduce these somewhat, but this is not readily predictable since the measured circle of least confusion only sets an upper limit to the resolution.

The saturation of the magnetic field is quite apparent in Figure 17 at 11.13 kilogauss. The inner (high field) rays are not deflected enough with respect to the outer (low field) rays. Even though the focus is the best at 10 kilogauss (the optimized field), the effects of the non-linearity of the iron already are apparent when one compares the 10-

kilogauss focus with that of the 6.7 or the 8.2 kilogauss.

The solid angle may be calculated from the maximum entrance angles. The value of 0.014 steradians obtained is probably a little low since the extreme rays were taken to be the last ones before the intensity on the quartz diminished. The uncertainty of where the cutoff occurred is such that smaller values of the solid angle would be obtained.

J. TARGET CHAMBER

The target chamber was based on the design used with the 16-inch radius spectrometer. It is shown in Figure 23. It is possible to rotate the body of the chamber (including the exit port to the spectrometer) with respect to the entrance beam pipe without breaking the vacuum seal. This allows the spectrometer to be set at any angle to the beam from -10° to $+155^{\circ}$. The unique arrangement that allows such a motion consists of a 3/8-inch, 190° , slot milled into the side of a heavy wall tube. Around this slot an O-ring is glued^{*} in a groove. Clock spring, 0.006-inch thick, is held against the O-ring with a pressure pad. The amount of squeeze on the lubricated[†] O-ring is only 0.007 inch to reduce sliding friction. The entrance beam pipe, which is rigidly fixed to a solid support, is sealed with thin teflon to the clock spring. The entrance beam pipe stays stationary as the entire target chamber and spectrometer are rotated about the target center.

This chamber differs from the one used on the 16-inch spectrometer primarily in the size of the tubing used in the chamber wall. By increasing the height and thickness, the reduction of the slot width due

* L-110 cement (Caram Mfg. Co., Monrovia, Calif.) thinned with toluene.

† Mixture of Molkote (MoS_2 ; Alpha Molykote Corp., Stamford, Conn.) and diffusion pump oil (e.g., Octoil-S; Consolidated Vacuum Corp., Rochester, N. Y.).

to atmospheric pressure on both ends was eliminated. The exit port to the spectrometer has been enlarged to accommodate the larger acceptance angles.

Though it would be desirable to have a larger diameter chamber, there are several factors that hinder this:

- (1) The chamber walls would have to be thicker to withstand the increased pressure on the ends due to atmospheric pressure.
- (2) The greater length of the O-ring and clock spring would produce more friction between them.
- (3) The exit port would have to be larger because of the diverging rays.

The target chamber is pumped from below through a 5-inch line to a 5 1/4-inch diameter diffusion pump - cold trap combination. See Figure 7 for a schematic representation of the vacuum system and Table 3 for the characteristics for each vacuum component.

An evaporation furnace is located below the target center. It is also shown in Figure 23. Two different evaporations can be made without opening the vacuum system.

The target holder (a standard design to this laboratory) permits the vertical position of the target to be set to $\pm 1/64$ inch and target angle to be set to $\pm 0.1^\circ$ on a well-defined axis. The holder is insulated from ground in order to be able to integrate the total charge that falls upon the target. On the holder are also located (see Figure 23):

- (1) movable quartz viewer,
- (2) Faraday cup for charge collection of beam that goes through the target,
- (3) auxiliary surface barrier detector.

The auxiliary detector is the only item that needs a few remarks. A commercial solid-state detector up to 1/4 inch in diameter is insulated from the target holder by a lucite support located 1 1/8 inch from the target center. Its angular position can be set to $\pm 0.1^\circ$. The auxiliary detector is useful in three different ways:

- (1) monitor to supplement the current integrator and measure target condition;
- (2) rapid surveys of the energy spectrum of the emitted particles;
- (3) coincidence work with the particle analyzed by the spectrometer.

K. FINAL ALIGNMENT

After the ray tracing had determined the image distance and optic properties, the target chamber and associated apparatus could be installed and aligned. Much of the following discussion will be in reference to the arrangement shown in Figure 12.

The correct position of the target chamber is such that its axis coincides with the vertical line running through the point of rotation of the spectrometer. Its height must also be set so that its center is 69 inches from the floor. An "A frame", whose base is anchored to the support carriage, supports the chamber; two horizontal braces from the face of the magnet add extra rigidity to the top of the "A frame". A height adjustment shim between the "A frame" and the chamber determines the final height of the chamber, as shown in Figure 23.

In order to position the target chamber on axis, the following procedure was used. First, the axis of a Brunson alignment telescope was made to coincide with the axis of the chamber by means of a specially ground holder. A set of quartz cross hairs were positioned at the center of the main support bearing so that they coincided with the axis of rotation. A pan filled with mercury was placed beneath these cross hairs on the cellar floor as shown in Figure 12. The quartz cross hairs and their reflection in the pool of mercury form a vertical line which passes through the center of the support bearing. By the placing of shims under the base of the "A frame", the axis of the telescope was made to coincide with the axis of rotation (this is true only when both the quartz cross hairs and their image line up on the internal cross hairs of the telescope). The height of the chamber was measured with respect to the fixed bench marks on the target room wall. With this information, the height adjustment shim was ground down by an amount to put the chamber center at 69 inches from the floor. After the alignment was rechecked, the base of the "A frame" and the horizontal support braces were fastened into place with taper pins. The collinearity of the two axes was rechecked again. The axis of the telescope was less than 0.003 inch from the quartz cross hairs, and less than 0.004 inch from their image, for all angles of the magnet on its track. A more accurate direct measurement was made with a dial indicator on the side of the target chamber. The results shown in Figure 13 indicate that the chamber is concentric to the axis of rotation within 0.001 inches when using the variable wheel supports and level vials.

The beam-defining entrance slits shown in Figure 3 were made

independent of the target chamber position by means of the bellows shown in Figure 23. The beam entrance tube is subjected to a large torque when the spectrometer angle is changed. Even though it is fixed by a rigid horizontal arm, its position cannot be assured to remain fixed. The mechanical decoupling will assure that the entrance slits are not displaced by this torque.

L. DETECTOR AND ASSOCIATED ELECTRONICS

The detector assembly is identical with the one used on the 16-inch spectrometer. It consists of an arrangement that allows slits of five different widths ($\delta r_c = 1/2, 1/4, 1/8, 1/16, \text{ and } 1/32$ inch) and six different foils to be placed in front of the charged particle detector without opening the vacuum. The resolution is a function of the slit size as given in Table 6. The foils are used to eliminate particle groups from the detector, or to identify particles by their characteristic energy loss in the foils.

Either a CsI(Tl) crystal and a photomultiplier or a solid-state detector may be used. The solid-state detector has turned out to be more useful than the CsI for three reasons:

- (1) Higher energy resolution.
- (2) The effective thickness may be changed by changing the bias across the detector. This enables one to use it as a dE/dx detector if need be, or to separate groups that have the same energy and rigidity. An example of this is shown in Figure 24.
- (3) The pulses produced are proportional to the energy of the particle. This allows a simultaneous measurement

of energy and momentum. See also Figure 24.

The electronics used is standard. A typical set up is shown in Figure 25. The data is monitored on a "live time" basis from the scalers. However, the 400-channel analyzer printouts are usually brought out on paper tape to be reduced later by the Burroughs 220 computer. See Appendix 2 for details of the reduction program.

Coincidence detection of the magnetically-analyzed particle and one detected in the auxiliary detector employs the circuitry described by Pearson (1963). An additional delay must be given the pulse from the chamber, since the analyzed pulse requires approximately

$$t = 202.0 \sqrt{A/E} \quad \text{nanoseconds}$$

to travel the distance from the target along the mean orbit to the detector, where A is the atomic weight and E is the energy in MeV. The extreme outer and inner orbits are approximately 10 per cent longer and shorter respectively. This time difference will limit the time resolution of the coincidence.

The design of a multi-detector array consisting of sixteen solid-state detectors lying on focal plane is under way. It will use a Nuclear Data 1024-channel, two-dimensional analyzer in the 16×64 mode to accumulate data.

M. MEASUREMENTS WITH RADIOACTIVE SOURCES

A Thorium B radioactive source is prepared by collecting Thoron gas recoils on the end of a polished stainless-steel rod in the manner described by Rutherford, et al. (1930). The decay scheme for Thoron is shown in Figure 26 along with a solid-state detector spectrum of the decay products of its daughter Thorium B (10.64-hour half-life). Three

intense alpha particle groups result from the branching of Thorium C.

According to Wapstra (1960) these energies are:

$$\text{ThC}' \rightarrow \text{ThD} : 8.7841 \pm .0028 \text{ MeV}$$

$$\text{ThC} \rightarrow \text{ThC}''(\alpha_1) : 6.0876 \pm .0020 \text{ MeV}$$

$$\text{ThC} \rightarrow \text{ThC}''(\alpha_0) : 6.0485 \pm .0020 \text{ MeV}$$

$$(\text{intensity ratio } \alpha_0/\alpha_1 = 2.57 \pm 0.01)$$

A typical ThC' momentum spectrum is shown in Figure 27 and for ThC in Figure 28. Care must be used in preparing a source for calibration purposes. If the collection time is more than a few half-lives, the observed peak is shifted to lower energies and broadened as shown in Figure 29. The reason for this is not readily apparent; it may be due to the collection of "dirt" on the surface and/or diffusion of the nuclei into the stainless steel.

From a spectrum such as shown in Figure 27, the magnetometer may be calibrated. Accurate positioning of the source at the same spot the beam would hit a target is vital. If the positioning is off by ϵ inches, then the error in energy would be

$$\frac{\delta E}{E} = \frac{2M}{D} \frac{\epsilon}{r_o} ,$$

where M is the magnification (0.84) and D is the dispersion (~ 3.8). The source width in the r direction, δr_s , should be no greater than $\delta r_c/M$ where δr_c is the detector slit width (usually 1/32 inch for the finest resolution).

The observed line shape results from the folding together of:

- (1) The natural line shape plus any broadening due to energy losses in the stainless steel rod. The residual nucleus of ThB will have been driven into the stainless

steel by two successive 6-MeV α recoils. The resulting energy distribution should be nearly rectangular plus a linear tail on the low energy side (Briggs, 1932).

- (2) δr_s , the vertical dimension of the source, reduced by the magnification factor, 0.84.
- (3) Resolution shape of the spectrometer. This is composed of the rectangle formed by the detector slit width and the aberrations of the spectrometer. The resolution has the general appearance of a rectangle with a low energy tail that increases as the acceptance angle is increased.

If the width of the natural line shape and recoil broadening is much less than either of or the combination of the other two shape widths, then the peak of the spectrum is taken to be the calibration point. If the natural line and recoil width is much greater than the combination of the other two, then half high point on the front edge of the spectrum is taken to be the calibration point (Snyder, 1950).

In actual practice, neither of the above criteria hold. For the line shown in Figure 27:

width of δr_c : 0.0096 Mc/s ,

width of $M\delta r_s$: 0.0080 Mc/s ,

width of the α
line plus
abberations : ~ 0.011 Mc/s .

The natural width was deduced by extrapolating the triangular shape to the base line. The base line width should equal the sum of all the con-

tributing widths. The true calibration point lies somewhere between the half height point and the peak. However, if one consistently picks on all spectra a given point, such as a peak, the error in doing so should be of second order. Therefore, as in previous calibrations the peak was chosen to be the calibration point.

From such a measurement the calibration constant K may be calculated from:

$$K = \frac{E_{\alpha}(M_{\alpha}/M_p)}{4f^2 \left(1 - \frac{E_{\alpha}}{2M_{\alpha}C^2} \right)}$$

E_{α} = energy of the observed α line

M_{α} = mass of the α particle

M_p = mass of the proton

f = observed frequency of the calibration point

Note that the constant K (0.011393 ± 0.000004) applies to protons. For other particles, the energy is given by

$$E_i = K f^2 \left[\frac{Z^2}{M_i/M_p} \right] \left[1 - \frac{E_i}{2M_i C^2} \right]$$

as shown in Figure 30.

The combination of the hysteresis of the spectrometer and that of the NMR magnetometer is shown in Figure 29 under extreme conditions. One curve was taken after bringing the field slowly from zero. The other curve was taken after the field had been at ~ 15.5 kilogauss for five minutes. The shift in the peak position is approximately $1/3000$. The first curve could be reproduced within experimental accuracy after the field had been returned to zero.

A measurement of the spectrometer aberrations was first at-

tempted by measuring the counting rate of the ThC' peak as a function of the $\bar{\theta}$ slit angle. The results are shown in Figure 28. Each of the curves has a linear portion which then becomes constant at some value of $\bar{\theta}$. The explanation for general behavior of the curves is that after a certain value of $\bar{\theta}$ is reached, any additional particles that go into the spectrometer aperture are prevented by the aberrations from going through the detector slits. The difference between the behavior at the inner radii and the outer radii was not immediately understood.

A second type of measurement was undertaken; the spectrum shape was measured for three different $\bar{\theta}$ windows, one at the center of the aperture and one each in the upper and lower portion of the aperture. The results are shown in Figure 31. These were quite disturbing. The spectrum from the upper third of the aperture was at higher frequency than the middle third. From the ray tracing measurements it is obvious that the aberrations shift the spectrum towards lower frequencies only (e.g., Figure 17). The results shown in Figure 31 can only be due to locating the detector slits 10.0 inches from the magnet. After moving the detector slits 0.5 inches towards the magnet (image distance = 9.47 ± 0.02 inches), the previous measurements were repeated. The results presented in Figure 31 are now consistent with the ray tracing measurements. The reason for the behavior when removing the $\bar{\theta}$ slits is also apparent. The upper third of the aperture (low field region) has considerably worse aberrations than either of the other thirds; the spectrum's full width at half maximum (FWHM) is larger, and the spectrum has a larger low energy tail. The reason for this is not apparent from either the field profiles or the ray tracing.

The Θ and Φ aberrations were compared by opening the Θ slits full while the Φ slits were narrow and vice versa. These spectra were compared to the one taken with both Θ and Φ narrow. The results are shown in Figure 32.

The solid angle size was measured; with a small aperture (0.0700-inch hole at 2.063 inches) between the radioactive source and the spectrometer aperture, a spectrum was measured. The aperture was removed, and with all the slits wide open, the spectrum was again measured. After correcting for the effects of the 10.64-hour half-life of ThB, the two spectra were compared. By this means the solid angle of the spectrometer was measured to be

.0151 steradians.

N. RELATIVE CALIBRATIONS

Instead of calibrating the spectrometer with a radioactive source, it is possible to determine its calibration constant by comparing it with the beam analyzer on the tandem accelerator. The 90° analyzer should be quite linear since the magnetic field is uniform and has been carefully calibrated against well-known (p, n) thresholds [see Marion (1961) for accelerator calibrations].

The most direct procedure was to run the beam directly into the spectrometer at 0° . A pin hole (≤ 0.005 inches in diameter) in a sheet of tantalum was placed at the target location. The 90° analyzer slits and the beam-defining slits (Figure 3) were closed down to improve beam resolution and to limit the total beam current. Care must be taken to protect the solid-state detector from too much beam. The observed momentum spectrum has the width of the detector slit and there-

fore the midpoint was taken to be the calibration point. This method has the advantage that aberrations cannot affect it since the beam is confined to the mean ray. The calibration constant K obtained in this manner is 0.011384 ± 0.000005 .

Elastic scattering is another way to compare the two magnets; however, this method has the disadvantage that contaminants on the surface of the target can introduce errors in the calibration. Elastic scattered particle profiles from gold are shown in Figures 33, 34, and 35. These profiles exhibit the rounding at the upper edge as one would expect from the measurements made previously (i. e., Figures 17, 28, 31, and 32). By reducing the solid angle in the Φ direction, the resolution (slope of front edge) is noticeably improved. The resolution limits for the beam were determined by Judd's (1950) first order formulas for a uniform field magnet. The beam energy seems to have a smaller spread than would be predicted from the slit settings. This confirms the long held belief of some members of this laboratory. The value of the calibration constant K obtained in this manner is 0.01138 ± 0.00001 .

O. ABERRATIONS

From the radioactive source measurements shown in Figure 32 and the elastic scattering shown in Figures 33, 34, and 35, it is quite apparent that the effects of aberrations are noticeable at sufficiently large apertures.

The values of Ikegami's (1958) aberrations parameters M_{11} and N_{11} are slightly changed from the original design (mainly, the measured

α is 0.51 instead of 0.50). The final values of the aberrations $M_{11}^{\oplus^2} r_o$ and $N_{11}^{\oplus^2} r_o$ are shown in Figure 1. From the ray tracing measurements, a qualitative dependence of M_{11} on β (or field) may be derived. The divergence of the beam in the \oplus direction was small enough to make the contribution of $N_{11}^{\oplus^2} r_o$ negligible compared with $M_{11}^{\oplus^2} r_o$. From the ray tracing foci (Figure 17), M_{11} has the form

$$\begin{aligned} M_{11} &\geq 0 && \text{for low fields} && (\beta \geq 0.4) \\ M_{11} &\simeq 0 && \text{for 10 kilogauss} && (\beta \simeq 0.4) \\ M_{11} &\leq 0 && \text{for high fields} && (\beta \leq 0.4). \end{aligned}$$

This is the behavior predicted by Ikegami (1958).

From the radioactive source measurements the contributions from both M_{11} and N_{11} could be measured independently, as shown in Figure 32. At this field (~ 7.5 kilogauss), β is near 0.50. The resulting aberrations should be

$$\begin{aligned} M_{11}^{\oplus^2} r_o &= -.263, \\ N_{11}^{\oplus^2} r_o &= +.027. \end{aligned}$$

But from Figure 32, the aberrations have about the right order of magnitude, but $N_{11}^{\oplus^2} r_o$ has the wrong sign. This discrepancy has not been resolved. Ikegami (1962) suggests that the failure to predict the correct sign for the \oplus aberrations may arise from the neglect of the fringing field in his analysis. Nevertheless, the removable pole tip radii have proved to be a valuable way to correct the optical properties of this spectrometer.

In general, the aberrations will affect line shapes and widths; however, yields will not be affected. These effects are shown for the ThC' alpha line (~ 7.5 kilogauss) in Figure 32, and the details are

tabulated in Table 8. The observed effects of increasing the entrance aperture are:

- (1) to broaden the line from $\delta p/p = 1/2520$ to $1/1540$;
- (2) to shift the peak by an amount $\delta p/p = 1/3500$ towards lower momenta.

In general, the aberrations will be asymmetric with a tail on the low energy side for fields less than 10 kilogauss and to the high energy side for fields greater than 10 kilogauss. However, to interpret line shapes properly, one must consider in addition to aberrations the various contributions to the shapes and widths discussed by Snyder (1950).

P. SUMMARY

The final values of the spectrometer parameters are presented in Table 9 along with the original design specifications. Also included are the first order predictions for the various parameters as calculated from Judd's (1950) theory. These were calculated using measured parameters whenever possible. The fringing field was taken into effect by

- (1) considering the total angle of deflection to be 189.6° instead of 180° ,
- (2) reducing the image and object distances by 2.01 inches (4.8° on a 24-inch radius).

The agreement is very good with the measured values as shown in Table 9.

In retrospect, there are a few things that could have been done differently.

- (1) The field parameters α and β should have been

optimized at a lower field than 10 kilogauss. The effects of saturation are quite apparent between the measurements at 8.2 kilogauss and 11.1 kilogauss. By optimizing α and β at a field near 7 or 8 kilogauss, the field shape would be nearly the same down to zero.

- (2) A magnet with adjustable poles [Rubin (1955) and Cohen (1961)] would be quite desirable. A small movement of the poles together produces a large change in β while affecting α only slightly. This would add another empirical adjustment to reduce aberrations.
- (3) Determination of the entrance angle for each ray in the ray tracing measurements.
- (4) Many minor details such as (a) overhead cables for water and power, (b) second set of beam-defining slits closer to the target chamber, (c) steering magnets after quadrupole lens, (d) more rigid support for the magnet, (e) better thermo-switches on the coils, (f) larger windows in the evaporation furnace, (g) magnet controls closer to counting equipment.

The spectrometer has proven itself to be a very useful laboratory instrument. During the first year of operation, the following reactions have been investigated:

Be^9 (p, α)	Li^7 (He^3 , p)
Be^9 (He^3 , p)	Li^7 (He^3 , α)
B^{10} (d, p)	B^{10} (He^3 , N^{12})
Na^{23} (p, α)	Be^9 charge states
F^{19} (He^3 , d)	C^{12} charge states

III. EXCITED STATES IN B^{11}

A. INTRODUCTION

The mass of Be^{11} has recently been measured by Pullen et al. (1962) and a few excited levels are known. With this information, one can try to identify the corresponding $T = 3/2$ excited states in the isospin quartet, $Be^{11} - B^{11} - C^{11} - N^{11}$,[†] as shown in Figure 36. Unfortunately, all of the reactions used to investigate the excited states in B^{11} above 10.6 MeV could populate only the states with isotopic spin $T = 1/2$. The only convenient charged particle reaction which can excite $T = 3/2$ states, $Be^9(He^3, p)$, has been investigated by Hinds (1959 and 1960) up to 10-MeV excitation in B^{11} .

With the mass of Be^{11} one can calculate where the analogue to the Be^{11} ground state would lie in B^{11*} :

$$\begin{aligned} \text{excitation energy in } B^{11} &= (Be^{11} - B^{11})_c^2 - (n - H^1)_c^2 + \\ &E_c(B^{11}) - E_c(Be^{11}), \end{aligned} \quad (1)$$

where the symbol $(Be^{11} - B^{11})$ stands for the atomic mass difference between Be^{11} and B^{11} , and the symbol $E_c(B^{11})$ stands for the coulomb excitation energy of the B^{11} nucleus.

For the coulomb energy one can assume that the protons are distributed uniformly through the nuclear volume. If the nuclear volume is a sphere with radius R , then

$$E_c = \frac{3}{5} Z(Z-1) \frac{e^2}{R}.$$

[†] N^{11} has not been observed experimentally.

When an experimental value of R is not available, one may use

$$R = R_0 A^{1/3} .$$

It is found experimentally that the coulomb energy term is well represented by this expression if $R = 1.45 A^{1/3}$ fermi. This is a value somewhat larger than that given by other definitions of the nuclear radius. For a discussion of these discrepancies between radii, see Wilkinson (1956) or Goldhammer (1963). For the value R_0 equal to 1.45 fermi, a uniformly-charged sphere gives

$$E_c(B^{11}) - E_c(Be^{11}) = 2.14 \text{ MeV} ,$$

and for the excitation in B^{11} , 12.87 MeV. One could also consider the coulomb exchange term which reduces the coulomb energy due to the exclusion principle (Goldhammer, 1963):

$$\frac{e^2}{R} \left(\frac{3}{5} Z^2 - .460 Z^{4/3} \right) .$$

In this case, the nuclear radius R would be smaller (e.g., as determined by electron scattering, etc.), thus giving about the same results.

A better value of the radius R_{11} for mass $A = 11$ can be found by comparing the coulomb energy difference of the mirror pair B^{11} and C^{11} . It follows that

$$E_c(C^{11}) - E_c(B^{11}) = (C^{11} - B^{11})c^2 + (n - H^1)c^2 ,$$

$$\frac{3}{5} \frac{e^2}{R_{11}} (6 \times 5 - 5 \times 4) = 2.765 \text{ MeV} .$$

This gives

$$\frac{3}{5} \frac{e^2}{R_{11}} = 0.2765 \text{ MeV} .$$

This value of the radius gives

$$E_c(B^{11}) - E_c(Be^{11}) = 0.2765 (5 \times 4 - 4 \times 3) = 2.212 \text{ MeV}.$$

Thus, this method yields 12.94 MeV for the excitation of B^{11} .

One can compare nuclei with the same Z , Be^{10} - B^{10} (first $T = 1$ state), and modify the nuclear radius to allow for the addition of the extra neutron as suggested by Wilkinson (1956). One readily finds by the above procedure that

$$E_c(B^{10}) - E_c(Be^{10}) = 1.969 \text{ MeV}.$$

This coulomb energy difference is multiplied by $(1 - 1/A)^{1/3}$ to allow for the increase in the nuclear radius from the additional neutron. One now gets

$$E_c(B^{11}) - E_c(Be^{11}) = \frac{(10)^{1/3}}{(11)^{1/3}} \{E_c(B^{10}) - E_c(Be^{10})\} = 1.907 \text{ MeV}.$$

This gives for the excited state in B^{11} an energy of 12.63 MeV.

Wilkinson (1956) reports that this method produces values that average 35 KeV high when compared with the experimental value. Thus, correcting for this empirical difference, the excitation energy would be 12.60 MeV. The above three methods yield values for the excitation of the B^{11} state which is the analogue to the Be^{11} ground state to be in the range 12.60 to 12.94 MeV.

We have surveyed the above region by means of the reaction $Be^9(He^3, p)$. The survey was extended to 9 MeV to overlap the work of Hinds (1959 and 1960), and up to 15 MeV to search for analogues to the excited states in Be^{11} . The energy level diagram for B^{11} from Ajzenberg-Selove and Lauritsen (1962) is shown in Figure 37.

B. EXPERIMENTAL DETAILS

A He^{++} beam was accelerated to 10 MeV in the ONR Tandem Van de Graaff accelerator by means of the standard 500-KeV neutral injection scheme. The beam was analyzed in a 90° , 34-inch radius magnet which had been calibrated by means of (p,n) reactions, and in the later stages of the experiment calibrated by a direct comparison with the 24-inch radius magnetic spectrometer (see Section II. N.). The beam analyzer momentum was assumed to be linear with NMR frequency. The beam analyzer slits were normally set at ± 0.075 inches to give momentum resolution ($\delta p/p$) of 1/450. A momentum resolution of 1/755 (slits ± 0.045 inches) was also used for a few careful measurements; this was impractical for most of the experiment since the beam intensity was reduced from a normal current of 0.3 μ amperes to less than 0.1 μ amperes. The He^{3++} beam passed through a thin, self-supporting beryllium foil prepared by the prescription given in Appendix 4. The thicknesses of the foils used were in the range 35 to 125 $\mu\text{gm}/\text{cm}^2$.

The 180° , 24-inch radius Office of Naval Research Magnetic Spectrometer was used to measure the momenta of the reaction products at various angles. This spectrometer is discussed in Section II. A 2600 Ω -cm silicon surface barrier detector made by Ortec* was used to detect the particles at the focus of the spectrometer. Aluminum foils of various thicknesses (0.003-, 0.005-, and 0.008-inches) were placed in front of the detector to eliminate all particles except protons. This also

* Oak Ridge Technical Enterprises Corp., Oakridge, Tennessee.

served to slow down the protons so that they would lose a maximum of energy in the detector's 300-micron depletion depth.

C. RESULTS

A spectrum of protons at 30° laboratory from Be^9 plus He^3 is shown in Figure 38 for B^{11} excitation energies between 8.9 and 14.6 MeV. Many spectra were measured at other observation angles to determine the mass of the target nucleus responsible for the various momentum groups in the spectrum. The targets contained some carbon and oxygen, and thus proton groups from $\text{O}^{16} (\text{He}^3, p) \text{F}^{18*}$ and $\text{C}^{12} (\text{He}^3, p) \text{N}^{14*}$ may be seen in Figure 38. These spectra at other angles were also used to see if there might be any proton groups from B^{11} that were missed at 30° due to low cross sections or confusion with contaminant peaks.

The results of these observations are shown in Table 10. All previously reported (Ajzenberg-Selove and Lauritsen, 1962) states were observed except:

- (1) the 10.26 - 10.32-MeV doublet was not resolved in the survey because of the low spectrometer momentum resolutions used (1/450);
- (2) the 11.0-MeV state was not observed because of its large width of 670 KeV;
- (3) the 14.0-MeV state was not observed because of its 300-KeV width and the large background in that portion of the spectrum.

States not previously reported were observed at 11.27- and 12.57-MeV excitation.

D. ISOTOPIC SPIN TEST

The two new states at 11.27 and 12.57 MeV could conceivably have isotopic spin $T = 3/2$. In order to test this hypothesis, it was decided to attempt to observe these states in the reaction $B^{10}(d,p)B^{11*}$. If these states are $T = 3/2$ states, then it would be impossible to populate them by means of this reaction without the violation of the conservation of isotopic spin. It is known that the excited states in the light nuclei have an isotopic spin impurity of less than 1/1000 (Burcham, 1955).

Very thin foils of 92 per cent enriched B^{10} were prepared by T. Fisher in a manner similar to the preparation of the beryllium foils outlined in Appendix 4. These foils were bombarded with 10-MeV deuterons. A proton spectrum measured at 30° is shown in Figure 39. Spectra were also measured at 15° and 45° . The 11.27-MeV state in B^{11} is clearly discernible from the background, and therefore has isotopic spin $T = 1/2$.

Protons are seen at the NMR frequency = 23.05 Mc/s, the frequency expected for protons from the 12.57-MeV state. However, protons from $B^{11}(d,p)B^{11*}$ (4.51) would also have the same momentum, and it is necessary to find out whether the observed protons come from $B^{10}(d,p)B^{11*}$ (12.57) or from the 8 per cent of B^{11} in the target. The common procedure of separating coinciding peaks by changing the observation angle was not successful. Since the masses of the two boron isotopes are very close, and since the 4.51-MeV state in B^{12} is broad, it is necessary to go to far backward angles to achieve complete separation. Attempts were made to observe the protons at 90° and 150° , but the yields at backward angles from the (d,p) stripping reaction are so

small that a proton peak was not observed above the background.

High purity B^{10} is very expensive, and the method of making the thin foils renders only a few per cent of the material into the finished foils. Therefore, it was decided to try a different method of ascertaining whether protons at a NMR frequency = 23.05 Mc/s in Figure 39 are due to the B^{10} or the B^{11} in this target. A natural boron foil was bombarded with 10-MeV deuterons and the proton spectrum for 30° was measured as shown in Figure 39; a spectrum was also measured at 15° . The ratio of the B^{11} content of this target to that in the enriched B^{10} target was determined by elastic scattering of He^3 to be

$$B_N^{11} / B_E^{11} = 25.5$$

where B_N^{11} = the amount of B^{11} in the natural boron target,

B_E^{11} = the amount of B^{11} in the enriched B^{10} target.

As a check, the relative amounts of B^{10} were also measured in these same targets; from the nominal percentage abundance of B^{11} in each target material, the ratio of the B^{11} in the two targets was 27.

In both spectra shown in Figure 39, the proton groups at NMR frequency = 23.05 Mc/s lie on a background of protons from other reactions. The estimated background shown by the dashed lines in Figure 39 was subtracted. The remaining protons should be in the ratio of the B^{11} contents of the two targets if $B^{11}(d,p)$ is responsible. The ratios of the peak heights and the ratios of the areas were found to be, for 15° and 30° :

<u>Angle</u>	<u>Peak Heights</u>	<u>Areas</u>
15°	27	28
30°	25	26

Thus the amount of B^{11} in the enriched target accounted for all of the measured peak within experimental accuracy.

The failure of $B^{10}(d,p)$ to populate this state at 12.57 MeV is evidence that this state has isotopic spin $T = 3/2$. More convincing evidence would be the discovery of additional states corresponding to the first few excited states in Be^{11} . This region of the spectrum, from NMR frequency = 21 to 24 Mc/s, in Figure 38 is confused by a large background of protons from other reactions, and no other states were evident in this region.

E. Q-VALUE AND WIDTH MEASUREMENTS

Higher precision measurements of the Q-values and widths of the 11.27-, 11.88-, and 12.57-MeV states were undertaken. Besides the two new states, the 11.88-MeV state was chosen since it did not correspond closely to any previously observed state. Other states were not measured due to the relatively good agreement between previous measurements and the preliminary results from the initial survey.

The Be^9 target thickness was determined to ± 5 per cent by the transmission of ThC' alpha particles. The 8.784-MeV ThC' alpha line was observed in the 24-inch spectrometer with and without the foil in front of the source. The shift of the line gave the energy loss (25.4 ± 1.3 KeV) of the alpha particles. The thickness was then calculated from the stopping cross sections (Whaling, 1958 and 1962) to be 49.5 ± 2.5 $\mu\text{gm}/\text{cm}^2$. This thickness was approximately 20 KeV for 10-MeV He^3 and 3 KeV for the outgoing protons.

The sources of uncertainty for the Q-value of the 11.266-MeV state are given in Table 11. The largest contribution to the uncertainty

was the beam resolution from the 90° magnetic analyzer. With the image and object slits set at ± 0.045 inches, the calculated momentum resolution was

$$\delta p/p = \frac{1}{2}(0.090''/34'') = 1/755.$$

However, it is known that the homogeneity of the beam is better than one would calculate (see Section II. N. and Figures 33, 34, and 35). If one wishes to consider probable errors, the beam will occupy the middle half of the slit width with a 50 per cent probability. Therefore, the uncertainty in beam energy can be taken to be $\pm 1/4$ of resolution calculated from the full slit width.

The uncertainty in the calibration constants arises from the uncertainty in the energy of the ThC' alpha particle. Wapstra (1960) gives this energy as 8.7841 ± 0.0028 MeV. The uncertainty in the spectrometer angle of $\pm 0.05^\circ$ ($= \pm 0.05$ inches on the track protractor) is consistent with the reproducibility of the zero measurements.

For the 11.88- and 12.57-MeV states the largest contribution to the uncertainty in the measured Q-value was the position of the peak in the proton spectra. In these cases, it was difficult to determine the peak position accurately because:

- (1) widths of the states are about 100 KeV;
- (2) large, uncertain, non-constant background was present;
- (3) poor counting statistics were due to small beam and small spectrometer aperture.

The widths were measured by considering the base width of the triangular shaped proton peaks. The base width is the sum of all the contributing widths including width due to the natural width of the state; the

residual after the subtraction of the known widths (source size, detector slit size, E_1 , target thickness, and aberrations) should be due to the natural width of the state. An uncertainty of 30 KeV has been assigned to the measured widths. This estimate is based on the observed spread in repeated measurements and the difficulty in determining the base line. The observed widths are shown in Table 10.

F. ANGULAR DISTRIBUTIONS

An attempt was made to determine the angular distribution of the protons from $\text{Be}^9(\text{He}^3, p)\text{B}^{11*}$ (12.57) and B^{11*} (14.56). We found that the large background of protons from other reactions shifted with angle and made it impossible to obtain more than a rough indication of the distribution.

For the 12.57-MeV state, the angular distribution observed at six center-of-mass angles between 9° and 70° is isotropic within 25 per cent. No indication of a strong stripping pattern was observed. For the 14.56-MeV state, the angular distribution observed at eight center-of-mass angles between 9° and 73° was forward peaked. The cross section at 9° , eight times the cross section at 73° , is still rising towards 0° .

G. CONCLUSIONS

Two new excited states were observed in B^{11} . The state at 11.27-MeV excitation has isotopic spin $T = 1/2$ because it was observed in the reaction $\text{B}^{10}(d, p)$. The state at 12.57-MeV excitation appears to have isotopic spin $T = 3/2$, and since it comes close to the predictions, it could be the analogue to the ground state of Be^{11} . The

width of the 12.57-MeV state is 145 KeV; this is reasonable because of the allowed $T = 3/2$ decay channel $\text{Be}^{10} + p$. This state does not appear to be formed in a direct process in the reaction $\text{Be}^9(\text{He}^3, p)$ at 10 MeV. The 14.56-MeV state which stands out clearly in Figure 38 could correspond to the 1.78-MeV state in Be^{11} . However, since this state has been observed in the $\text{Li}^7(\alpha, n)$ and $\text{Be}^{10}(n, n', \gamma)$ reactions (Ajzenberg-Selove and Lauritsen, 1962), it is unlikely to have isospin $T = 3/2$.

IV. EXCITED STATES IN Li^6

A. INTRODUCTION

The first spectrum examined with the 24-inch radius magnetic spectrometer was that of the alpha particles from $\text{Be}^9(p, \alpha)\text{Li}^{6*}$. This experiment was chosen as one part of a many-sided examination of the $A = 6$ nuclei being carried out in this laboratory. At the time this work was begun, this reaction had been used to study excited states in Li^6 at 2.18- and 3.56-MeV excitation (Browne, 1957). No additional states had been seen below 5-MeV excitation. Additional states had been reported at 4.52-, 5.35-, 5.5-, 6.63-, 7.40-, 8.37-, and 9.3-MeV by the work of Allen et al. (1960) as shown in Figure 40. The reaction $\text{Be}^9(p, \alpha)\text{Li}^{6*}$ was chosen as a straightforward application of the magnetic spectrometer.

B. EXPERIMENTAL DETAILS

A proton beam was accelerated to 10 MeV in the ONR Tandem Van de Graaff accelerator using the H^- injection scheme. The beam was analyzed in the 90° magnet as described in Section III. B. The proton beam of intensity 0.3 to 1.0 μ amperes passed through a thin, self-supported beryllium foil prepared by the prescription given in Appendix 4. The thicknesses of the foils used were in the range 35 to 200 $\mu\text{gm}/\text{cm}^2$.

The 180° , 24-inch radius Office of Naval Research Magnetic Spectrometer was used to measure the momenta of the alpha particles at various angles. This spectrometer is discussed in Section II. A 300 Ω -cm silicon surface barrier detector made by Ortec[†] was used to

[†] Oak Ridge Technical Enterprises Corp., Oakridge, Tennessee.

detect the particles at the focus of the spectrometer. Since both doubly-charged alphas and protons have the same energy at the image of the spectrometer, it was necessary to use the solid-state detector as a dE/dx detector for the protons to separate the two groups. An example of a typical spectrum is shown in Figure 24.

C. RESULTS

The momentum spectra of alpha particles from the reaction $\text{Be}^9(p, \alpha)\text{Li}^6$ are shown in Figures 41 and 42 for alpha particles emitted at laboratory angles of 30° and 90° . The spectrum of all particles detected at the image of the spectrometer for 30° is shown in Figure 43. Similar observations were made at laboratory angles of 15° , 30° , 45° , 90° , and 150° in an effort to obtain better discrimination between the discrete alpha particle groups and the continuous background, but at all of these angles the background was essentially unchanged. The large background from the breakup in flight of Li^{6*} , Be^8 , Be^{9*} , and B^{9*} prevented the observation of alpha particle transitions to excited states in Li^6 above 6 MeV. However, the region of excitation energy covered in these investigations extended from 0 to 9 MeV. The locations and widths of the excited states in Li^6 corresponding to the discrete alpha particle groups in Figures 41 and 42 are given in Table 12.

The quantitative study of the 4.50- and 5.36-MeV states was complicated by the rising background. To determine the Q-value and width of the 4.50-MeV state, the background was assumed to be linearly rising as shown in Figure 42. The low intensity and the uncertainty of the background subtraction were the main contributions to the uncertainty of the measurements. For the 5.36-MeV state, a simple resonance

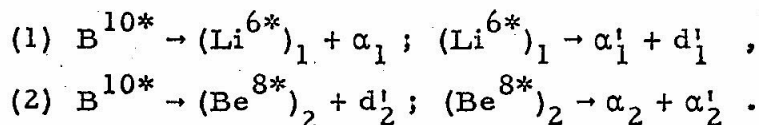
shape was fit to the curve so that the remaining background was smoothly varying. The uncertainty shown in Table 12 reflects the range of resonance energy and width that yielded a satisfactory shape for the residual background.

D. COINCIDENCE EXPERIMENT

A coincidence experiment between the magnetically-analyzed alpha particle and an associated particle in the target chamber was attempted to eliminate the effects of the background and to see if any of the excited states decay electromagnetically to the ground state of Li^6 . The coincident particle was detected in the chamber with the auxiliary surface-barrier detector described in Section II. L. and shown in Figure 23. Coincidence circuitry described by Pearson (1963) was used. An additional delay was given the pulse from the chamber detector to allow for the flight time of the analyzed particle around the spectrometer. A coincidence resolving time from 50 to 100 nanoseconds was used.

Li^6 recoils were observed from transitions to the ground and 3.57-MeV states. The 3.57-MeV state is therefore stable against particle decay, as has been previously shown (Allen, 1960). Li^6 recoils corresponding to transitions to the 2.19-, 4.50-, and 5.36-MeV states were not seen. Therefore, these states must decay primarily by particle emission.

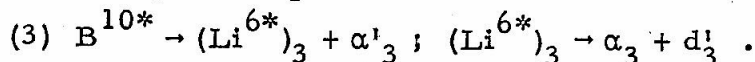
The attempt to reduce the background was unsuccessful. To understand the reason for the failure to improve the situation, consider the following two decay modes of the excited compound nucleus B^{10*} :



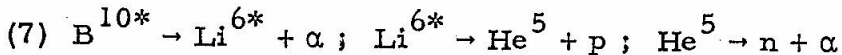
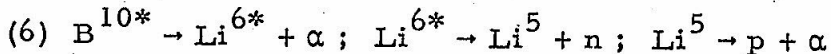
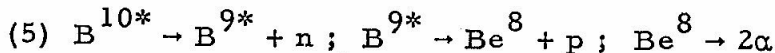
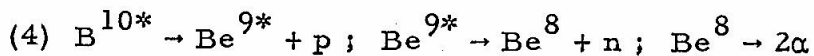
We suppose that the velocity vector of the primary alpha particle α_1 is determined by the spectrometer. Hence, the velocity vector for the recoil nucleus $(\text{Li}^{6*})_1$ is determined by kinematics. One would like to detect α'_1 or d'_1 in coincidence with α_1 and thereby eliminate the background caused by α_2 and α'_2 with the same velocity vectors as α_1 .

Since the velocity vector for $(\text{Li}^{6*})_1$ is determined, the velocity vector for α'_1 (and d'_1) is fixed for any given laboratory direction for the α'_1 (and d'_1) detector. However, it can be seen from the velocity diagrams in Figure 44 that an α_2 with the same velocity vector as α_1 can be accompanied by an α'_2 (and d'_2) with the same velocity vector as α'_1 (and d'_1). Therefore, it is not possible to distinguish α_1 from the α_2 background by the coincident detection of α_1 with α'_1 (and d'_1).

Furthermore, another decay mechanism can also give an α_3 with a velocity vector equal to that of α_1 and an α'_3 (and d'_3) with the same velocity vector as α'_1 (and d'_1). This mode is:



Other decay modes:



can be eliminated by a coincidence measurement, since no d is produced; and since the decay leads to four particles, there is no longer a correlation between the resultant particles' energies and laboratory angles. However, any improvement that may have developed from this was overcome by the extreme loss of counting statistics and the additional confusion of random coincidences.

The inability to distinguish between decay modes (1), (2), and (3) can be derived from the following facts:

- 1) All the reactions start with the same masses (Be^9 and proton) and the same total center-of-mass energy.
- 2) All the reactions end with the same masses (two alpha particles and deuteron) and the same total center-of-mass energy release.
- 3) In the center-of-mass system the total momentum is always zero.

For a given alpha particle energy and angle, and for a given coincident particle angle, the other alpha particle and the deuteron can only have a definite value for their center-of-mass energies and angles. These values are given by the conservation of energy and momentum. The concept of the formation of a compound nucleus is used only for convenience. This result would hold equally well for a direct reaction.

E. CONCLUSIONS

The width of the 4.50-MeV state is much less than reported from $\text{He}^4 + d$ scattering (Galonsky, 1955, and L. Senhouse, 1963). No other reported measurements of the width exist. From the published alpha particle spectrum from $\text{Li}^7(\text{He}^3, \alpha)\text{Li}^{6*}$ (Allen, et al., 1960), the state appears to have about the same width as the 3.56-MeV state, which is narrow. However, since they used a thick $(\text{Li}^7)_2\text{O}$ target with poor resolution, the state could have a width up to 250 KeV. Another measurement of the $\text{Li}^7(\text{He}^3, \alpha)\text{Li}^{6*}$ alpha particle spectrum was done by Linck, et al. (1961). Although they do not publish any observed widths, the published alpha particle spectrum appears to have a width in the neighborhood of

230 KeV. This value is in agreement with the value of 260 ± 80 KeV obtained here. In all cases, the excitation energies agree within experimental accuracy.

The state observed at 5.36 MeV has a measured width of 350 ± 60 KeV. Allen et al. (1960) publish a width of less than 100 KeV for a state at 5.35 MeV. On the other hand, the published spectrum of Linck et al. (1961) has a state at 5.6 MeV with a width that appears to be about 410 KeV. The agreement between all of these measurements is poor. However, this state does appear to be different from the 1.0-MeV wide state inferred from the $\text{He}^4 + d$ scattering phase shifts by Galonsky (1955) at 5.5 MeV. This broad state was also inferred from the background subtraction by Allen et al. (1960). If the two states are different and the 5.36-MeV state is not observed in $\text{He}^4 + d$ scattering as is now believed, then the 5.36-MeV state could be the analogue $T = 1$ state to the first excited states in He^6 and Be^6 (Ajzenberg-Selove and Lauritsen, 1960). The width would result from the open $T = 1$, $\text{He}^5 + p$ channel.

APPENDIX 1. PERFORMANCE CHARACTERISTICS FOR
MAGNETIC SPECTROMETER AND ITS POWER SUPPLY

(1) Energy Range: 27 MeV - 0.1 MeV protons.

(2) Mean Radius = 24 inches.

(3) Field Profile will be defined in terms of series expansion:

$B(r) = B_0(1 - \alpha P + \beta P^2 + \dots)$ where $P = (r - r_0)/r_0$. With a field such that $B_0 = 10$ kilogauss at $r = r_0 = 24''$, α and β shall be given by $\alpha = -0.5 \pm 0.02$ and $\beta = 0.34 \pm 0.1$ over the useful range of r . As a design aim, the vendor shall attempt to hold the tolerances above over the widest possible range of B_0 .

(4) Solid Angle: with source located at 26" from the plane of the magnet entrance, the solid angle shall be greater than or equal to 0.015 steradian when $B_0 = 10$ kilogauss. The solid angle will be computed from the dimensions of the gap, with gap length equal to the distance between pole faces at $r = 24''$ and gap width Δr determined by measurement and defined as the useful range of r over which the magnetic field profile satisfies the tolerances in specification (3).

(5) Angle of Observation: the angle between the direction of the beam striking the target and the direction of a particle emitted into the central trajectory of the spectrometer must be variable from -10° to the maximum possible backward angle, at least 155° , simply by rotating a carriage supporting the magnet about a vertical axis through the target.

(6) Mounting: the spectrometer platform rotates through 360° about a vertical axis through the target. The spectrometer may be translated on this platform toward or away from the target to effect an

interchange of the image and source distances from their normal values of 26" and 9". The spectrometer shall be oriented on its support to accept particles emitted into the horizontal plane from a source located 69" above the floor. In order to allow for the deflection of charged particles in the fringing field at the entrance, the mount must include provision for (a) tilting the spectrometer about the Z-axis, and (b) raising or lowering the spectrometer in its carriage.

(7) The curved iron plate which forms the back of the spectrometer shall be made in two sections, the upper entrance segment shall be 60° , the lower segment 120° .

(8) The pole faces shall be fabricated of Armco iron. The thickness of each pole face shall be at least 1" at $r = 24"$.

(9) The side plates of the magnet, the pole body, and the pole face shall be cut as indicated on the accompanying drawing so that an 8° segment is removed at entrance and exit boundaries. Four plugs will be furnished by the vendor to replace the iron removed in these cuts, and the plugs will be constructed from the same type of iron as that removed in the cuts. Those parts of the plug which replace the pole face and pole body will be machined to present to the entering or emergent beam a circular boundary with radius of curvature 10.25".* Bolts and alignment pins will be provided to fix the plugs rigidly to the side plates of the magnet. These plugs are to be designed so that they may be removed by the customer without disturbing the vacuum chamber. When the plugs are inserted in the cuts, the gaps in the magnetic circuit,

* This specification was changed after the bidding due to an error in the calculation of the entrance and exit radii.

introduced by these cuts, should be no more than 0.005" and the gaps should be of constant length.

(10) Power Supply: current regulation to provide $(\Delta I/I) = 1/3000$ in the current range from I_{\max} for $E_p = 27 \text{ MeV}$ to $I_{\max}/4$ preferably lower. Power supply will exceed the maximum power rating of the spectrometer by a factor of two. The motor shall be wired for 440-volt, 3-phase supply. The quotation shall include the cost of all motor starting equipment, and the power supply shall be complete with base, requiring only connection to the customer's 440-volt supply in order to put the power supply into service.

(11) Cooling Water: maximum temperature rise = 20°C . Input pressure = 80 psi.

(12) The vendor shall furnish (a) a plot of the radial variation of the magnetic field at two angles to demonstrate that the requirements on α and β have been satisfied when the field at 24" is 10 kilogauss, and (b) a plot of the azimuthal variation of the magnetic field at constant radius to demonstrate that the field is homogeneous within 1 part in 1000.

APPENDIX 2

Several programs were written for the Burroughs 220 computer to facilitate data reduction and the interpretation of results. One important program calculated relativistic kinematics and Q-values, but since this is relatively straightforward, it will not be discussed further. Only the Peak-Valley Sum program will be mentioned.

A solid-state detector at the image of the spectrometer can produce a quite complicated pulse height spectrum (e. g., Figure 24). It is always possible, although not always convenient, to position a single-channel discriminator-scaler combination around each peak. In this manner, the total numbers of each variety of particle are counted. However, when the dE/dx of a particle is measured (by foils or by varying the thickness of the detector) along with the energies of several other particles, the relative pulse heights will change with the magnetic field. In this case, the positioning of a discriminator is rather tedious. By setting the discriminator on only the peaks of immediate interest, one can save the remaining information on printouts (or punchouts) from the 400-channel analyzer. A computer program was written to reduce this remaining data.

The primary purpose of this program is to find the peaks in the data and the corresponding valleys in between. Then the sums of the data between adjacent valleys are calculated (each valley is split between the peak to the right and the one to the left).

However, at times there may be a large number of relative peaks and valleys due to statistical fluctuations and noise in the background. These fluctuations will yield erroneous peaks and valleys. It may be

desirable to smooth out the fluctuations in the data by applying a Gaussian at each point:

$$N'(x_0) = \sum_{x=-n}^{x=+n} N(x)(\sigma\sqrt{2\pi})^{-1} \exp\left[-\frac{1}{2}\left(\frac{x_0-x}{\sigma}\right)^2\right]$$

where

$N(x)$ = the number of counts in channel x

$N'(x_0)$ = the smoothed number of counts in channel x_0

σ = the standard deviation of the Gaussian

n = the number of channels such that the truncation error is less than a predetermined amount.

The amount of smoothing is completely determined by the value of σ . For $\sigma \leq 0.25$, the smoothed spectrum is the same as the original; for $\sigma > 12$, the smoothed spectrum is lumped into only one peak. Thus, with the proper choice of σ , all the fluctuations are smoothed out without destruction of the information contained in the data.

After the peaks and the valleys have been determined from the smoothed spectrum, the sums in the actual data are made. The computer program thus provides a more consistent way of handling the data than may be done by a cursory inspection. In all cases, the computer-reduced data has been as good or better than the data taken from the discriminator-scaler combination.

APPENDIX III

When the design of the 24-inch radius spectrometer was first considered, it was deemed important to have a provision to allow the observation of nuclear reactions at 180° . Peterson and Barber (1962) have developed a method of observing at 180° electron elastic scattering with a double-focusing magnetic spectrometer. Their method involves the use of a small deflection magnet. The beam from the linear accelerator is bent by the deflecting magnet by 10° before it hits the target. The target is located just outside the fringing field of the deflection magnet; thus the beam scattered at 180° re-enters the deflection magnet's field and is deflected by another 10° . The net effect is that the accelerator beam and the 180° scattered beam are separated by 20° . The spectrometer now analyzes the resultant scattered beam.

Another method as envisioned for the 24-inch spectrometer would bring the beam into the back of the spectrometer, as illustrated in Figure 45. The entering beam paths were determined from a scaled-up measurement of the fringing field on the 16-inch radius magnetic spectrometer. In practice, one would use the ray tracing technique discussed in Section II. I. to empirically find the approximate focus of the beam paths.

A small deflection magnet could be placed at this focus to deflect the beam into the various bombarding angles. A set of entrance slits would be necessary to make certain that the beam was approaching the target at the correct angle. This deflection magnet's field and, to a certain extent, position would have to be readjusted each time the spectrometer's field is changed. This is somewhat inconvenient;

however, if a multi-detector array is used at the image of the spectrometer, then an entire narrow line could be measured at one spectrometer field setting. This seems to be the only practical way to make this measurement without the continual adjustment of both the spectrometer and the deflection magnet.

Provision was made for the removal of the upper 60° segment of the back of the spectrometer for this purpose. However, with the present arrangement, the spectrometer apparatus, including the vacuum box, entrance slits, and target chamber, would have to be rebuilt, since bringing the beam through the back of the magnet is so completely different.

APPENDIX IV

The thin beryllium foils used in this experiment were obtained by three different means:

- (1) foils given to W. K. Kellogg Radiation Laboratory by Dr. H. Bradner of the University of California in 1946;
- (2) preparation in this laboratory by the technique of Bradner (1948);
- (3) preparation by the method described below.

The foils obtained from (1) and (2) usually had a thickness greater than $100 \mu\text{gm}/\text{cm}^2$. Any foils that were thinner than this thickness were very difficult to strip from their backing and to mount on a foil holder.

A modification of a technique from Chalk River (Woytowich, 1962) has proven to be reliable for producing foils thinner than $100 \mu\text{gm}/\text{cm}^2$. The order of operations consists of: *

- (1) Glass microscope slides (1×3 inches or 2×3 inches) are prepared;
 - (a) wash in acetone,
 - (b) wash with a mildly abrasive soap, such as Lava,
 - (c) wash in sodium dichromate with sulfuric acid glass cleaning solution (Handbook of Chemistry and Physics, page 2990),
 - (d) rinse in distilled water,
 - (e) dry in a warm ($\geq 100^\circ\text{F}$), dust-free location.

* NOTE: anyone planning to work with beryllium or its oxides should first read the article by Schubert (1958) about the health hazard of beryllium and berylliosis.

Precleaned microscope slides have been satisfactory without any preparation. The cleanliness of the slides is most important for hole-free, easily stripped foils.

(2) Two evaporation boats are prepared in a bell jar (water-cooled metal or glass with radiation shields to prevent localized heating);

(a) a tantalum boat contains 30 ± 10 mg barium chloride for an evaporation distance of 4 inches.

Barium chloride is used because of its high solubility in water.

(b) A Berlox pure beryllium oxide ceramic crucible, size S-1 (National Beryllia Corporation, New Jersey), is placed in a helically wound coil made from 0.080-inch thick tungsten wire. This coil was prepared by wrapping the tungsten wire around a 9/16-inch diameter steel rod by using a low voltage - high current transformer to locally heat the wire. Small pieces of solid beryllium are placed in the crucible. A beryllium oxide crucible is used because of the high reactivity of beryllium with metals at high temperatures. Beryllium oxide also has the highest thermal conductivity of any of the common ceramics.

(3) The barium chloride is evaporated first.

(4) The voltage from a high-current transformer is raised slowly, heating the tungsten coil. This outgasses the

crucible and its contents; the vacuum should be kept below 5×10^{-5} Torr. With 2.85 volts and 160 amperes, the beryllium starts to melt and evaporate. Approximately one to two minutes are required to produce an opaque layer of beryllium on the slides. Just before becoming opaque, the thickness is approximately $25 \mu\text{gm}/\text{cm}^2$. The vacuum may rise as high as 10^{-4} Torr. during the evaporation. The slides must be allowed to cool under vacuum for 30 minutes or more to prevent the formation of beryllium oxide with the air that is let into the bell jar.

- (5) The beryllium on the slide is divided into squares with a sharp scribe. A razor-blade scraped along the edges of the slide will expose the barium chloride.
- (6) The slide is slowly lowered at a 45° angle into a beaker of water (plus 5 per cent acetone by volume to reduce surface tension). The barium chloride dissolves and the beryllium floats on the surface of the water as the slide is lowered.
- (7) The foil can now be picked up on a thin (0.005 to 0.010-inch thick) aluminum or tantalum frame (with holes up to $\frac{1}{2}$ -inch in diameter). Upon drying, the thicker foils may drop off the frame; a little shellac will prevent this.

Foils prepared in this manner have been very robust under bombardment by a beam of charged particles. They appear to be uniform and relatively free from pin holes.

TABLE 1. Pole Piece Profile

Radius	Distance from Mid Plane (normalized at $r = r_o$)
18.00	1.362
18.25	1.404
18.50	1.452
18.75	1.494
19.01	1.541
19.16	1.567
19.26	1.575
19.51	1.584
20.02	1.604
20.52	1.624
21.02	1.643
21.53	1.662
22.03	1.681
22.54	1.699
23.04	1.716
23.55	1.734
24.05	1.752
24.55	1.770
25.05	1.787
25.56	1.804
26.06	1.821
26.56	1.838
27.07	1.856
27.57	1.873
28.07	1.889
28.58	1.902
28.83	1.908
28.99	1.913
29.09	1.899
29.34	1.842
29.59	1.784
29.84	1.728
30.00	1.694

TABLE 2. Alpha and Beta Versus Field

California Institute of Technology measurements with vacuum box in place over all usable field (least squares fit to measured field profile).

<u>Field</u>	<u>Alpha</u>	<u>Beta</u>
3.2 kG	.510	.50
6.3 kG	.515	.51
8.5 kG	.513	.45
11.3 kG	.515	.39

Spectromagnetic's measurements without vacuum box at $r = r_0 = 24''$ (calculated from measurements of the logarithmic derivative of the field profile).

<u>Field</u>	<u>Alpha</u>	<u>Beta</u>
6.0 kG	.508	.41
10.0 kG	.508	.39
12.5 kG	.503	.26

TABLE 3. Vacuum Components and Characteristics

2" Station on Quadrupole Lens Support (ultimate vacuum $\leq 10^{-6}$ Torr.)			
Component	Manufacturer	Part No.	Characteristics and Comments
Forepump	Welch	1400B	Speed: 21 liters/min
Diffusion pump	Cons. Vacuum	PMC-115	2 1/4" diam.; oil; speed: 105 l/s
Refrigerated baffle	Cons. Vacuum	BC-20	Freon cooled
Cold trap	Cal Tech	4T4-30	Capacity: .63 liters liquid N ₂
Pirani gauge	Cons. Vacuum	GP-105	High pressure protection for diffusion pump; Range: 0-2000 migrons
Discharge gauge	Cons. Vacuum	GPH-100A	Cold cathode; Range: 10^{-3} to 10^{-5} Torr.
High vacuum valves	Vacuum Research	VG-105	HVEC supplied
	Cal Tech	SV2-02	Standard 2" size

5" Station on Spectrometer Support (ultimate vacuum $\leq 10^{-6}$ Torr.)

Component	Manufacturer	Part No.	Characteristics and Comments
Forepump	Cenco	HYVAC 7	Speed: 70 liters/min
Diffusion pump	Cons. Vacuum	PMC-720	5 1/4" diam.; oil; speed: 750 l/s
Refrigerated baffle	Cons. Vacuum	BC-41	Freon cooled
Cold trap	Cal Tech	4B-60	Capacity: .71 liters; automatic filler and trap heater for quick entry
Pirani gauge	Cons. Vacuum	GP-105	(Same as above.)
Discharge gauge	Cons. Vacuum	GPH-100A	(Same as above.)
High vacuum valves	Circle Seal	--	1/4", 1/2", and 3/4" sizes
	Cal Tech	SV2-02	Standard 2" size
	Cal Tech	2B-82	Rough valve
	Cal Tech	4B-019	5 1/4" size
	Cal Tech	4B-49	Special 2" valve

TABLE 4. Θ and Φ Slit Angles Versus Dial Readings

Reading	Φ	Θ	Reading	Φ	Θ
30 ^o	max.		0 ^o	0.000 ^o	0.000 ^o
29	6.537 ^o		-1	-0.207	-0.128
28	6.300		-2	-0.414	-0.254
27	6.064		-3	-0.619	-0.379
26	5.828		-4	-0.822	-0.502
25	5.592		-5	-1.023	-0.622
24	5.358		-6	-1.223	-0.740
23	5.124		-7	-1.431	-0.857
22	4.890		-8	-1.617	-0.971
21	4.658		-9	-1.811	-1.084
20	4.426	max.	-10	-2.003	-1.193
19	4.195	2.716 ^o	-11	-2.194	-1.301
18	3.964	2.564	-12	-2.382	-1.407
17	3.735	2.411	-13	-2.568	-1.510
16	3.506	2.260	-14	-2.752	-1.611
15	3.279	2.110	-15	-2.934	-1.710
14	3.052	1.960	-16	-3.114	-1.806
13	2.826	1.812	-17	-3.281	-1.900
12	2.602	1.664	-18	-3.466	-1.992
11	2.378	1.518	-19	-3.639	-2.081
10	2.156	1.373	-20	-3.809	-2.167
9	1.935	1.229	-21	-3.977	-2.252
8	1.714	1.086	-22	-4.142	-2.333
7	1.495	0.945	-23	-4.305	-2.413
6	1.278	0.805	-24	-4.465	-2.489
5	1.061	0.667	-25	-4.622	-2.563
4	0.846	0.531	-26	-4.777	-2.635
3	0.632	0.395	-27	-4.929	-2.704
2	0.421	0.262	-28	-5.077	-2.771
1	0.209	0.131	-29	-5.223	-2.835
0	0.000	0.000	-30	-5.366	-2.896
			-31	-5.506	max.
			-32	-5.642	
			-33	-5.775	
			-34	-5.905	
			-35	-6.032	
			-36	-6.155	
			-37	-6.275	
			-38	-6.391	
			-39	-6.503	
			-40	-6.612	
			-41	max.	

Slit Zeros:

Θ : 0 = 0 by definition

Φ : top slit reads +50' at zero position; bottom slit reads -1^o 10' at zero position

TABLE 5. Delta Theta Due to Phi Versus Theta

Theta	$\hat{\phi} = 0.0^\circ$	0.5°	1.0°	1.5°	2.0°	2.5°	3.0°	3.5°	4.0°	4.5°	5.0°	5.5°	6.0°	6.5°	7.0°
0° 180°	0.000	0.500	1.000	1.500	2.000	2.500	3.000	3.500	4.000	4.500	5.000	5.500	6.000	6.500	7.000
5 175	0.000	0.025	0.099	0.220	0.384	0.589	0.829	1.101	1.400	1.723	2.207	2.428	2.804	3.194	3.560
10 170	0.000	0.012	0.049	0.111	0.196	0.305	0.436	0.589	0.763	0.956	1.169	1.399	1.646	1.909	2.186
15 165	0.000	0.008	0.033	0.073	0.130	0.202	0.290	0.394	0.512	0.646	0.793	0.955	1.113	1.318	1.152
20 160	0.000	0.006	0.024	0.053	0.096	0.149	0.214	0.292	0.380	0.480	0.591	0.713	0.845	0.989	1.142
25 155	0.000	0.005	0.019	0.042	0.075	0.119	0.168	0.228	0.298	0.376	0.463	0.560	0.665	0.779	0.901
30 150	0.000	0.004	0.015	0.034	0.060	0.094	0.136	0.185	0.240	0.305	0.376	0.454	0.540	0.632	0.732
35 145	0.000	0.003	0.012	0.028	0.050	0.078	0.112	0.152	0.199	0.251	0.310	0.375	0.446	0.523	0.605
40 140	0.000	0.003	0.010	0.023	0.042	0.065	0.093	0.127	0.166	0.210	0.259	0.313	0.373	0.437	0.506
45 135	0.000	0.002	0.009	0.020	0.035	0.055	0.078	0.107	0.139	0.176	0.218	0.263	0.313	0.367	0.425
50 130	0.000	0.002	0.007	0.016	0.029	0.046	0.066	0.090	0.117	0.148	0.183	0.221	0.263	0.308	0.357
55 125	0.000	0.002	0.006	0.014	0.024	0.038	0.055	0.075	0.098	0.124	0.153	0.184	0.219	0.257	0.298
60 120	0.000	0.001	0.005	0.011	0.020	0.031	0.045	0.062	0.081	0.102	0.126	0.152	0.181	0.212	0.246
65 115	0.000	0.001	0.004	0.009	0.016	0.025	0.037	0.050	0.065	0.082	0.101	0.123	0.146	0.172	0.199
70 110	0.000	0.000	0.003	0.007	0.013	0.020	0.029	0.039	0.051	0.064	0.079	0.096	0.114	0.134	0.155
75 105	0.000	0.000	0.002	0.005	0.009	0.015	0.021	0.029	0.037	0.047	0.058	0.071	0.084	0.099	0.114
80 100	0.000	0.000	0.002	0.003	0.006	0.010	0.014	0.019	0.025	0.031	0.038	0.047	0.055	0.065	0.075
85 95	0.000	0.000	0.001	0.002	0.003	0.005	0.007	0.009	0.012	0.015	0.019	0.023	0.027	0.032	0.037
90 90	0.000	0.000	0.000	0.000	0.000	0.000	0.000	0.000	0.000	0.000	0.000	0.000	0.000	0.000	0.000

TABLE 6. R and Z Foci Versus Field from Ray Tracing

d_r = R image distance; d_z = Z image distance; Ab = diameter of the circle of least confusion.

9" Radius Pole Tips

Field	$\bar{\phi} = \pm 5.8^\circ$			
	All Rays		5 Inner Rays	
	d_r	Ab	d_r	Ab
3.37 kG	9.39	.41	9.53	.05
6.71 kG	9.91	.23	9.53	.07
8.22 kG	8.79	.20	9.55	.05
10.03 kG	9.37	.05	9.53	.05
11.13 kG	8.83	.17	9.37	.02

14.5" Radius Pole Tips

Field	$\bar{\phi} = \pm 5.1^\circ$			
	All Rays		5 Inner Rays	
	d_r	Ab	d_r	d_z^*
3.37 kG	9.49	.28	9.73	7.7
6.71 kG	9.45	.16	9.99	7.5
8.22 kG	10.65	.26	9.98	7.7
10.03 kG	9.99	.11	9.75	7.5
11.13 kG	9.29	.10	10.53	7.5

* independent of the radius of the entrances

TABLE 7. Momentum (Energy) Resolution Versus Dispersion and
Detector Slit Size

Dispersion (mean field)	3.74 (3.37 kG)	3.77 (6.71 kG)	3.80 (8.22 kG)	3.86 (10.03 kG)	3.56 (11.13 kG)
Slit					
1/2"	$\frac{1}{180} \left(\frac{1}{90} \right)$	$\frac{1}{181} \left(\frac{1}{90} \right)$	$\frac{1}{182} \left(\frac{1}{91} \right)$	$\frac{1}{185} \left(\frac{1}{93} \right)$	$\frac{1}{171} \left(\frac{1}{86} \right)$
1/4"	$\frac{1}{359} \left(\frac{1}{180} \right)$	$\frac{1}{361} \left(\frac{1}{181} \right)$	$\frac{1}{365} \left(\frac{1}{182} \right)$	$\frac{1}{370} \left(\frac{1}{185} \right)$	$\frac{1}{342} \left(\frac{1}{171} \right)$
1/8"	$\frac{1}{718} \left(\frac{1}{359} \right)$	$\frac{1}{723} \left(\frac{1}{361} \right)$	$\frac{1}{729} \left(\frac{1}{365} \right)$	$\frac{1}{741} \left(\frac{1}{370} \right)$	$\frac{1}{684} \left(\frac{1}{342} \right)$
1/16"	$\frac{1}{1436} \left(\frac{1}{718} \right)$	$\frac{1}{1446} \left(\frac{1}{723} \right)$	$\frac{1}{1458} \left(\frac{1}{729} \right)$	$\frac{1}{1482} \left(\frac{1}{741} \right)$	$\frac{1}{1368} \left(\frac{1}{684} \right)$
1/32"	$\frac{1}{2872} \left(\frac{1}{1436} \right)$	$\frac{1}{2892} \left(\frac{1}{1446} \right)$	$\frac{1}{2916} \left(\frac{1}{1458} \right)$	$\frac{1}{2964} \left(\frac{1}{1482} \right)$	$\frac{1}{2736} \left(\frac{1}{1368} \right)$

Table 8. Aberrations Measured with ThC' Source (8.784 MeV α^{++})

<u>Angles</u>				<u>Resolution</u>	<u>Width</u>		<u>Peak Shift</u>	
<u>Reading</u>		<u>True Angle</u>			FWHM	Mc/s	(δp/p)	Mc/s
Θ	Φ	Θ	Φ					
5°	5°	0.67°	1.06°	1/2520	.000		.000	
10	10	1.37	2.16	1/1980	.0055	(1/5000)	.001	(1/28000)
19	29	2.72	6.54	1/1540	.011	(1/2500)	.008	(1/3500)
5	10	0.67	2.16	1/2310	.003	(1/9200)	.000	
10	10	1.37	2.16	1/1980	.0055	(1/5000)	.001	(1/28000)
15	10	2.26	2.16	1/1730	.010	(1/2800)	.004	(1/6900)
19	10	2.72	2.16	1/1730	.010	(1/2800)	.004	(1/6900)
10	10	1.37	2.16	1/1980	.0055	(1/5000)	.001	(1/28000)
10	15	1.37	3.28	1/1730	.006	(1/4500)	.002	(1/14000)
10	20	1.37	4.43	1/1680	.009	(1/3100)	.005	(1/5500)
10	29	1.37	6.54	1/1680	.010	(1/2800)	.005	(1/5500)
5	5	0.67	1.06	1/2520	.000		.000	
5	10	0.67	2.16	1/2310	.003	(1/9200)	.000	

These measurements were taken with

$$\frac{1}{D} \frac{\delta r_c}{r_o} = 1/2900 ,$$

$$\frac{M}{D} \frac{\delta r_s}{r_o} = 1/3450 .$$

The aberration width was taken to be the increase in the base line width over the value measured with $\Theta = 0.67^\circ$ and $\Phi = 1.06^\circ$. The base line width was found by extrapolating the triangular line shape (see Figure 32) to the abscissa.

TABLE 9. Summary of Properties

Property	As Calculated*	As Specified	Final Value or As Measured
Radius		24"	24"
Maximum Energy	45 MeV proton (16.2 KG)	27 MeV proton (12.4 KG)	
Observation Angles		-10° to 155°	-10° to 155°
Maximum Entrance Angles Θ Φ	+2.3° (without vacuum box) ±5.7° (without vacuum box)		+1.9° (with vacuum box) ±5.8° (with vacuum box)
Solid Angle (steradians) without vacuum box with vacuum box	.0178 .0155	.015	.0151
Pole Entrance Radius	14.5"	14.5"	9.0"
Field Parameters (see Table 2) α β	.50 .34	.50 + .02 .34 ± .1	.51 .39 to .51
Object Distance (d_o)		26.2"	25 49/64"
Image Distances (see Table 6) d_r d_z	9.64" 7.58"	9.0" 9.0"	9.37 to 9.55" (set at 9.47") 7.5 to 7.7"
Magnification (M)	.84		3.56 to 3.86
Dispersion (D) (see Table 7)	3.76		
Resolution in Energy full solid angle half solid angle		1° .1°	less than .2° FWHM for narrow line .1° for 2/3 full solid angle
Tip of Focal Plane	57° to 61°		45.4° to 49.6° (from \perp to mean ray)
Total Deflection	190°	180°	189.6°
Current Regulation ($\Delta I/I$)		± 1/3000	± 1/3100 to 1/26000 (ΔI approxi- mately constant)
Variation of Field with Angle		± 1/1000 (2 gaps)	± 1/2000 (4 gap widths from entrance)

* Note: calculations were made with first order formulas of Judd using measured parameters wherever possible.

Table 10. Excited States in B^{11} from Be^9 (He, p)

Q-value (MeV)	Excitation in B^{11} (MeV)	Observed Width (keV)	Observation Angles	Previous Measurements Excit. in B^{11}	* Width (keV)
1.40 ± 0.02	8.92	< 35	$30^\circ, 45^\circ$	8.923 ± 0.004	< 0.7
1.12 ± 0.02	9.20	< 35	$30^\circ, 45^\circ$	9.187 ± 0.002	< 0.1
1.04 ± 0.02	9.28	< 35	$30^\circ, 45^\circ$	9.276 ± 0.002	5
0.46 ± 0.02	9.87	200 ± 50	30°	9.87 ± 0.02	160
0.03 ± 0.03	10.30	250 ± 50	$30^\circ, 60^\circ, 90^\circ, 120^\circ$	$\begin{cases} 10.26 \pm 0.03 \\ 10.32 \pm 0.02 \end{cases}$	$\begin{cases} 220 \\ 45 \pm 14 \end{cases}$
-0.28 ± 0.02	10.61	100 ± 50	$30^\circ, 60^\circ, 90^\circ, 120^\circ$	10.61 ± 0.03	100
	11.0		(not observed)	11.0	670
-0.9416 ± 0.0069	11.266	< 30	$30^\circ, 60^\circ, 90^\circ, 100^\circ, 120^\circ$	(not previously observed)	
-1.135 ± 0.015	11.460	< 100	$30^\circ, 45^\circ, 60^\circ, 90^\circ, 100^\circ, 110^\circ, 120^\circ$	11.46 ± 0.02	70
(-1.54 ± 0.05)	(11.87)	(260 ± 50)	$30^\circ, 60^\circ, 90^\circ$	11.97 ± 0.08	320
-1.559 ± 0.012	11.884	72 ± 30	$30^\circ, 37.5^\circ, 45^\circ, 60^\circ, 90^\circ, 120^\circ$	11.68 ± 0.10	140
-2.240 ± 0.012	12.565	145 ± 30	$7.5^\circ, 22.5^\circ, 30^\circ, 37.5^\circ, 45^\circ, 60^\circ, 90^\circ$	(not previously observed)	
-3.00 ± 0.1	13.3	500 ± 100	$30^\circ, 60^\circ, 90^\circ, 100^\circ, 110^\circ, 120^\circ$	13.16	250
	14.0		(not observed)	14.0	300
-4.238 ± 0.015	14.563	< 50	$7.5^\circ, 15^\circ, 22.5^\circ, 30^\circ, 37.5^\circ, 45^\circ, 52.5^\circ, 60^\circ, 90^\circ, 100^\circ, 110^\circ$	14.55	

* Ajzenberg-Selove and Lauritsen (1961 and 1962)

Table 11. 11.266 State Error Analysis

<u>Source of Error</u>	<u>Uncertainty</u>	<u>ΔQ (MeV)</u>
Beam Energy		
Slit resolution ($\pm .045''$)	$\pm 1/1500$	$\pm .0056$
Calibration constant	$\pm 1/4000$	$\pm .0021$
Current regulation ($\Delta I/I$)	$\pm 1/8000$	$\pm .0022$
Target thickness ($\Delta t/t$)	$\pm 1/20$	$\pm .0004$
Spectrometer Angle	$\pm .05^\circ$	$\pm .0012$
Analyzed Particle Energy		
Peak position	$\pm 1/4000$	$\pm .0017$
Calibration constant	$\pm 1/4000$	$\pm .0016$
Current regulation ($\Delta I/I$)	$\pm 1/25,000$	$\pm .0006$
Target thickness ($\Delta t/t$)	$\pm 1/20$	$\pm .0001$
Total	-0.9416	$\pm .0069$

Table 12. Excited States in Li^6 from Be^9 (p, α) Li^6

Q-value (MeV)	Excitation in Li^6 (MeV)	Observed Width (keV)	Previous Measurements Excit. in Li^6	* Width (keV)
2.13 ± 0.02	0.00	< 35	0	0
-0.06 ± 0.02	2.19	< 35	2.184 ± 0.003	21
-1.44 ± 0.02	3.57	< 35	3.560 ± 0.006	$5.9 \rightarrow 9.1 \text{ eV}$
-2.37 ± 0.04	4.50	260 ± 80	4.52 ± 0.08	~ 600
-3.23 ± 0.04	5.36	350 ± 60	5.35 ± 0.07 5.5 ± 0.4	<100 ~ 600

* Ajzenberg-Selove and Lauritsen (1961).

REFERENCES

- F. Ajzenberg-Selove and T. Lauritsen, 1960, American Institute of Physics Handbook (to be published).
- 1961, Landolt-Börnstein Tables, K. Hellwege edit., (Springer-Verlag, Berlin), p. I-1.
- Allen, Almqvist, and Bigham, 1960, Proc. Phys. Soc. (London) A75, 913.
- Alvarez, Brown, Panofsky, and Rockhold, 1961, Rev. Sci. Instr. 31, 556.
- H. Bradner, 1948, Rev. Sci. Instr. 19, 662.
- G. H. Briggs, 1932, Proc. Roy. Soc. A139, 638.
- C. P. Browne, and C. K. Bockelman, 1957, Phys. Rev. 105, 1301.
- W. E. Burcham, 1955, Progress in Nuclear Physics 4, 171.
- N. D. Coggeshall, 1947, J. App. Phys. 18, 855.
- Cohen, Cookson, and Wankling, 1961, Nucl. Instr. 10, 84.
- L. Crane, 1951, AECU-1670, Nov. 23, 1951.
- H. A. Enge, 1959, Rev. Sci. Instr. 30, 248.
- A. Galonsky and M. T. McEllistrem, 1955, Phys. Rev. 98, 590.
- P. Goldhammer, 1963, Rev. Mod. Phys. 35, 40.
- Hinds and Middleton, 1959, Proc. Phys. Soc. (London) A74, 196.
- 1960, Proc. Phys. Soc. (London) A75, 754.
- H. Hintenberger, 1949, Rev. Sci. Instr. 20, 748.
- H. Ikegami, 1958, Rev. Sci. Instr. 29, 943.
- 1962, private communication:
- D. L. Judd, 1950, Rev. Sci. Instr. 21, 312.
- D. L. Judd and S. A. Bludman, 1957, Nucl. Instr. 1, 46.
- D. W. Kerst and R. Serber, 1941, Phys. Rev. 18, 53.

- G. R. Lamberston, 1956, UCRL-3366, March 21, 1956.
- T. Lauritsen and F. Ajzenberg-Selove, 1962, Nuclear Data Sheets, Sets 5 and 6 (National Academy of Sciences - National Research Council, Washington, D. C.).
- C. W. Li, 1951, Ph. D. Thesis, California Institute of Technology (unpublished).
- Linck, Nicolas, Bilwes, and Magnac-Valette, 1961, J. Phys. Radium 22, 581.
- J. B. Marion, 1961, Rev. Mod. Phys. 33, 139.
- J. D. Pearson, 1963, Ph. D. Thesis, California Institute of Technology (unpublished).
- G. A. Peterson and W. C. Barber, 1962, Phys. Rev. 128, 812.
- Pullen, Litherland, Hinds, and Middleton, 1962, Nuclear Physics 36, 1.
- E. S. Roseblum, 1950, Rev. Sci. Instr. 21, 586.
- S. Rubin and D. C. Sachs, 1955, Rev. Sci. Instr. 26, 1029.
- Rutherford, Chadwick, and Ellis, 1930, Radiations from Radioactive Substances, Cambridge University Press, p. 561.
- C. A. Scharschu, 1935, The Book of Stainless Steels, E. Thum, edit. (Amer. Soc. for Metals, Cleveland, Ohio), p. 369.
- J. Schubert, 1958, Scientific American 199, 27; Aug. 1958.
- L. Senhouse, 1963, private communication.
- F. B. Shull and D. M. Dennison, 1947a, Phys. Rev. 71, 681.
1947b, Phys. Rev. 72, 256.
- K. Siegbahn and N. Svartholm, 1946a, Nature 157, 872.
1946b, Arkiv. f. Mat. Ast. o. Fys. 33A, No. 21.
- Snyder, Rubin, Fowler, and Lauritsen, 1950, Rev. Sci. Instr. 21, 852.
- Vincent, King, and Rowles, 1959, Nucl. Instr. and Meth. 5, 254.
- A. H. Wapstra, 1960, Nuclear Physics 18, 587.

- W. Whaling and C. W. Li, 1951, Phys. Rev. 81, 150.
- W. Whaling, 1958, Handbuch der Physik 34, 193.
- W. Whaling and D. Demirlioglu, 1962, private communication.
- D. H. Wilkinson, 1956, Phil. Mag. 1, 1031.
- E. A. Wolicki and A. Knudson, 1961, NRL Quarterly on Nuclear
Science and Technology, January 1961.
- W. Woytowich, 1962, private communication.
- W. L. Zingery, 1961, Rev. Sci. Instr. 32, 706.

Figure 1. Aberrations in the r Direction Versus β .

The aberrations δr as calculated from the theory of Ikegami (1958) are shown independently for both the θ and ϕ directions. The dashed curves are based on the original design parameters with two values of the entrance and exit radii. The solid curves are based on the final measured parameters. See text: pages 9 and 37.

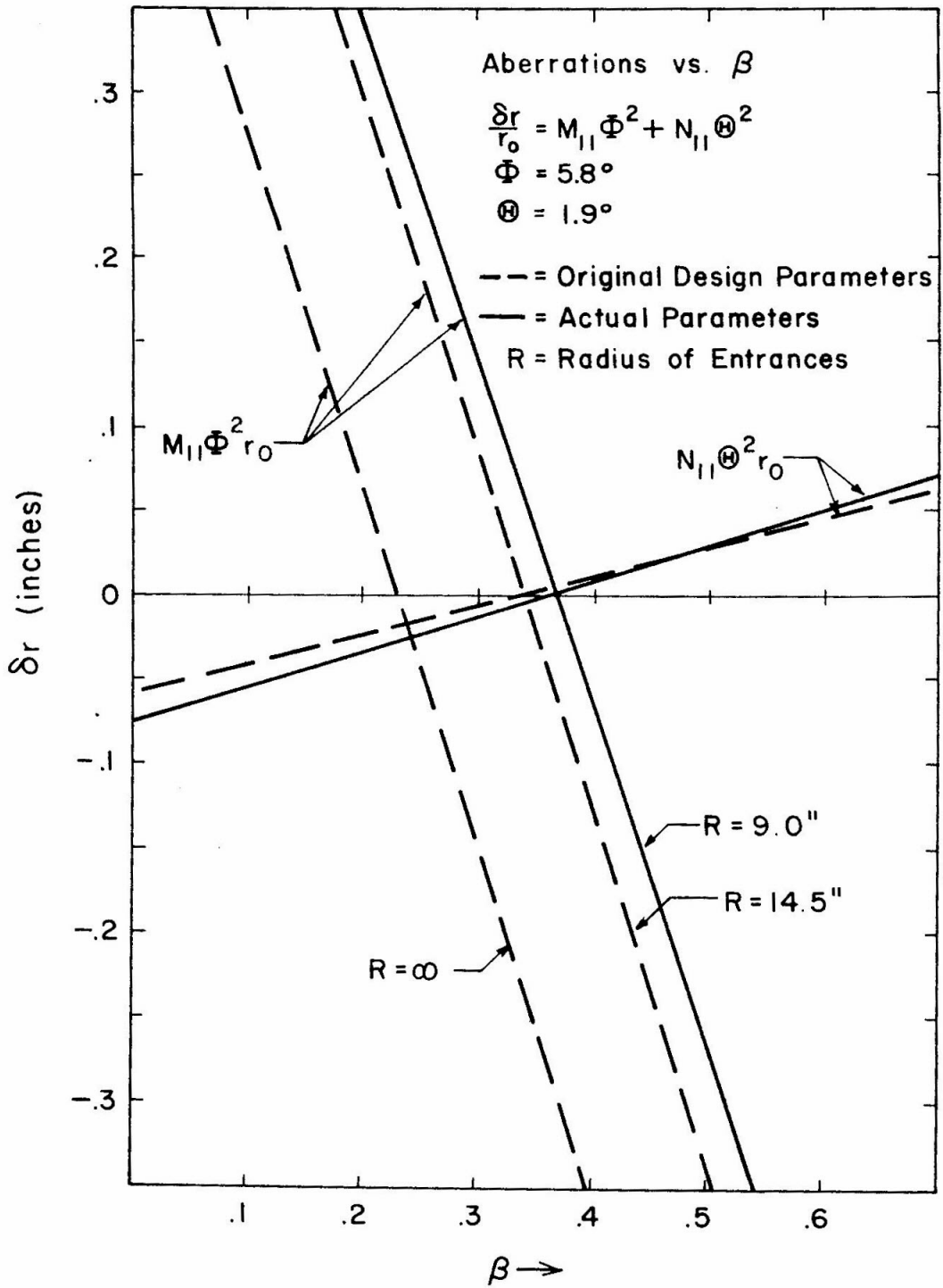


Fig. 1

Figure 2. Office of Naval Research 24-Inch Magnetic Spectrometer.

This photo shows the spectrometer set at 90° to the incoming beam. Included here are all the minor details left out of the idealized view shown in Figure 3. See text: page 11.

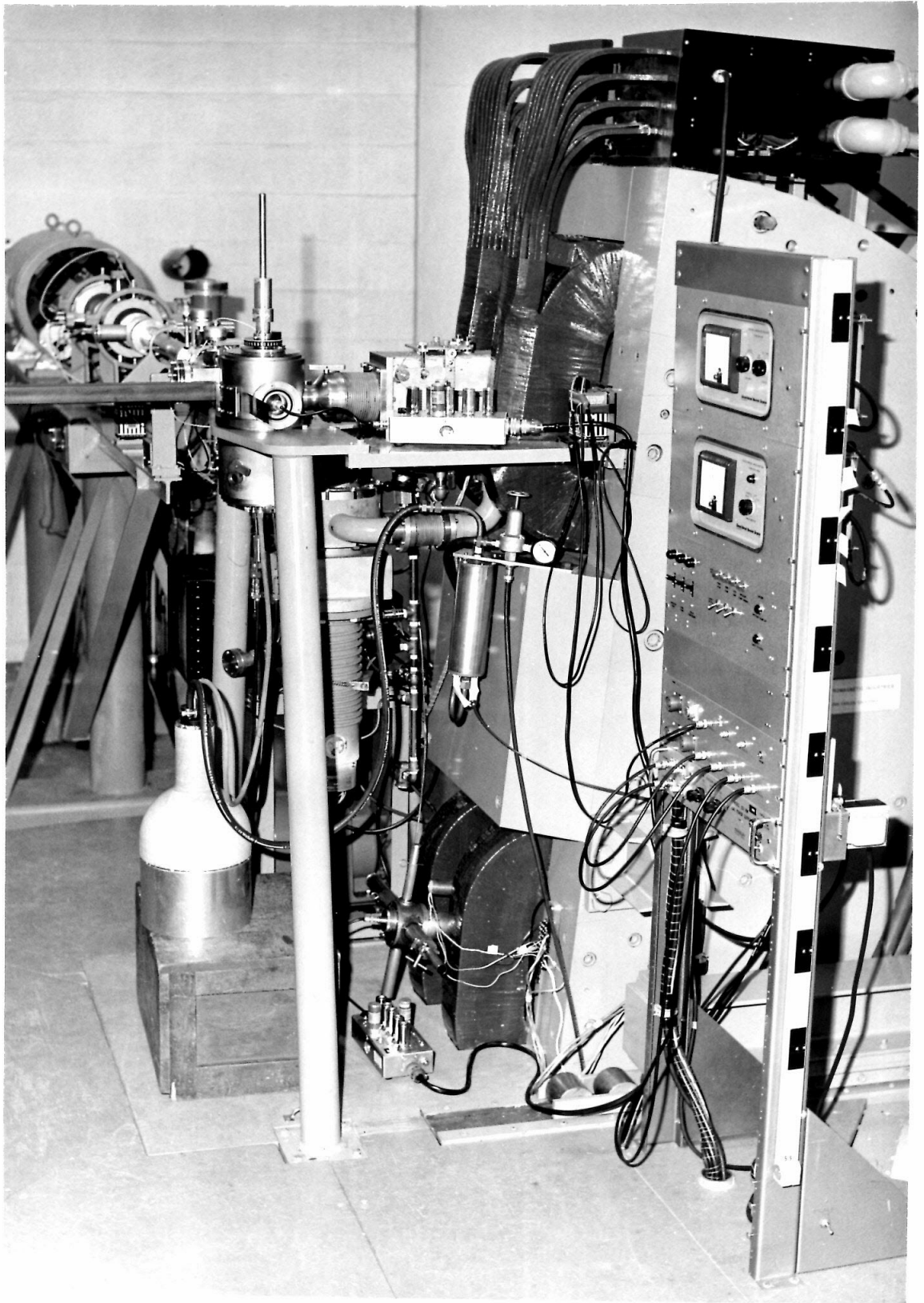


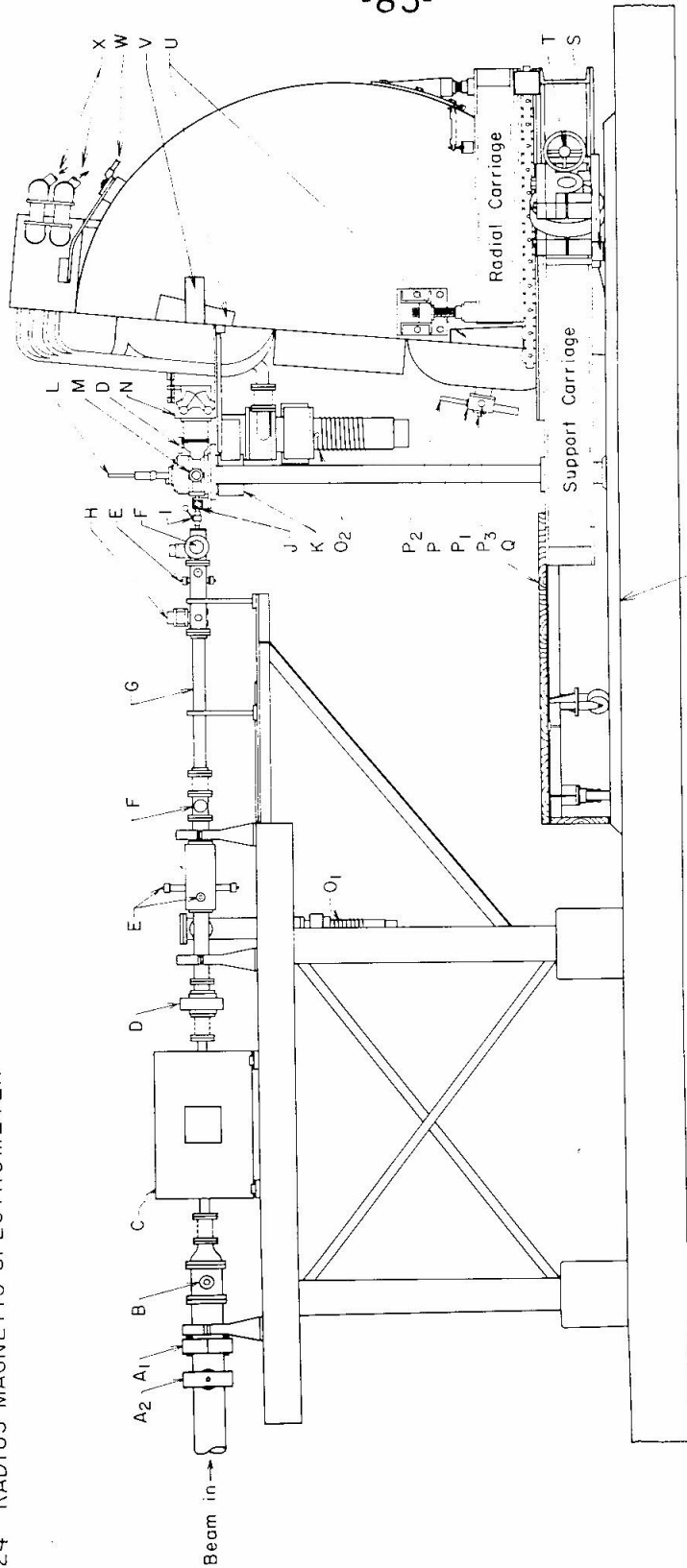
Fig. 2

Figure 3. 24-Inch Radius Magnetic Spectrometer.

The spectrometer is shown at 0° to the incoming beam; all the beam handling equipment after the tandem switching magnet is also shown. See text: pages 11 and 14.

24" RADIUS MAGNETIC SPECTROMETER

-85-



0 2 4 6 Feet

- | | | | |
|--|-------------------------------------|-------------------------------------|-----------------------------------|
| A Deflection Magnets | F Viewer | O Pumping Station | T Crank to Rotate Spectrometer |
| A ₁ Horizontal | G Iron Entrance Tube | O ₁ 2 1/4" | U Removable Pole Entrances |
| A ₂ Vertical | H Beam Chopper | O ₂ 5 1/4" | V Removable Piece for Back Angles |
| B Switching Magnet | I 1/4" Valve | P Detector Assembly | W Current Leads |
| C Quadrupole Lens (two element) | J Entrance Brace (to rigid support) | P ₁ Surface Barrier Det. | X Cooling Water |
| D 2" Valve | K Evaporation Furnace | P ₂ 6 Foils | |
| E Horizontal and Vertical Defining Slits | L Target Holder | P ₃ 5 Collector Slits | |
| | M Target Chamber | Q Wooden Platform | |
| | N Entrance Slits | R Track | |
| | | S Track Vernier (0.1°) | |

Fig. 3

Figure 4. Starting and Safety Circuits.

The starting and safety circuits for the motor-generator set are shown schematically. Note: some relay contacts have been omitted for clarity. See text: page 11.

Current Regulation Circuit.

The current regulation circuits are shown in block diagram. See text: page 12.

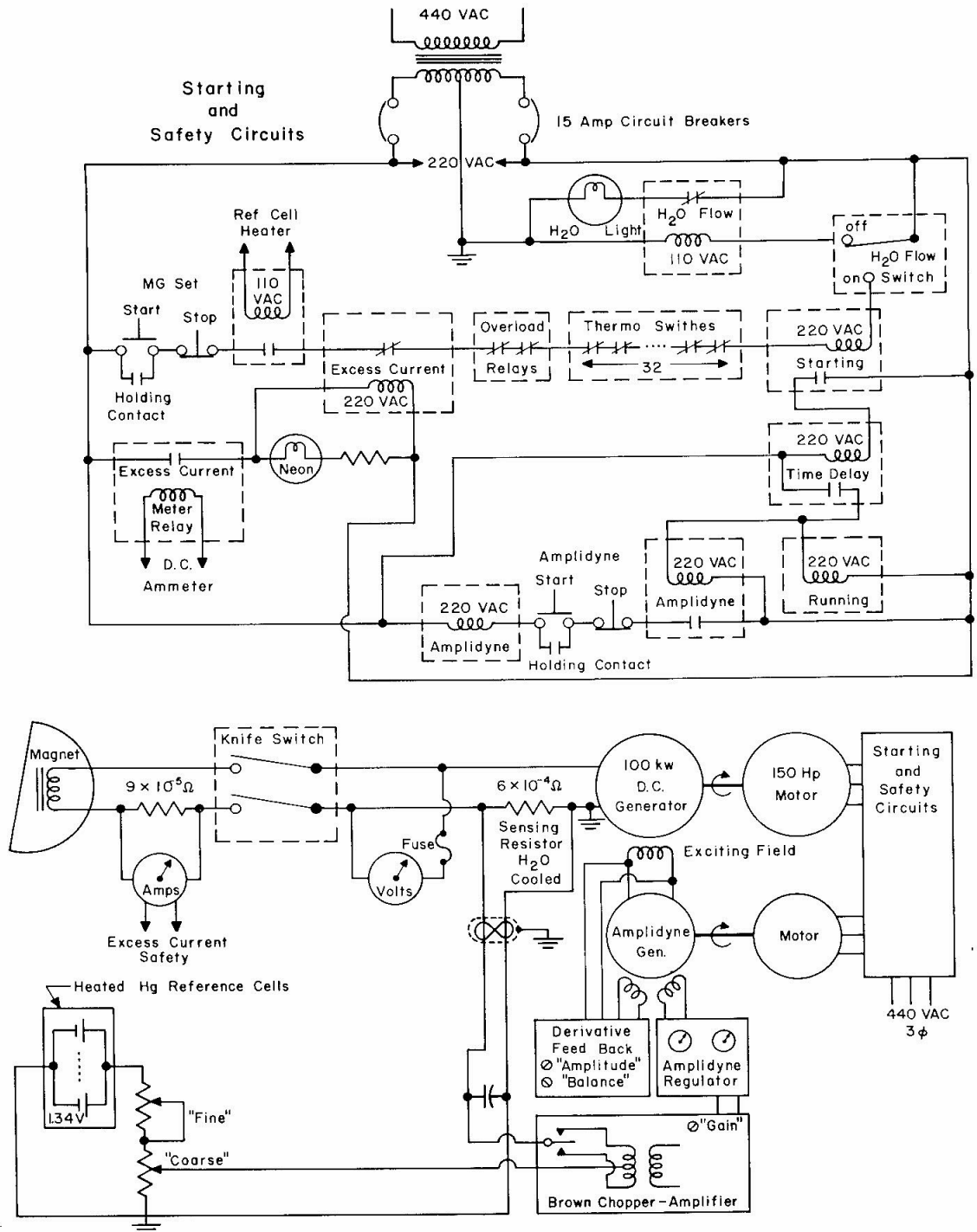


Fig. 4

Figure 5. Fringing Field Profile.

The fringing field perpendicular to the face of the magnet at the mean radius (24 inches) is shown. This field measurement was used to determine the path of the mean ray through the fringing field. In order to make the mean ray pass through the target center horizontally, the magnet was lowered by $5/16$ inch and tipped backwards 4.8° . See text: page 13.

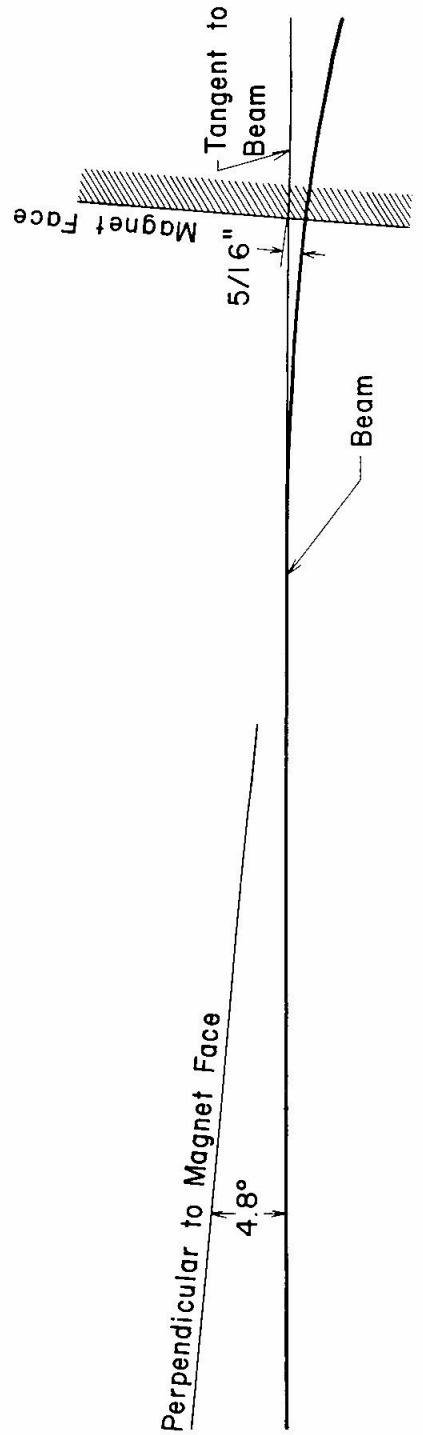
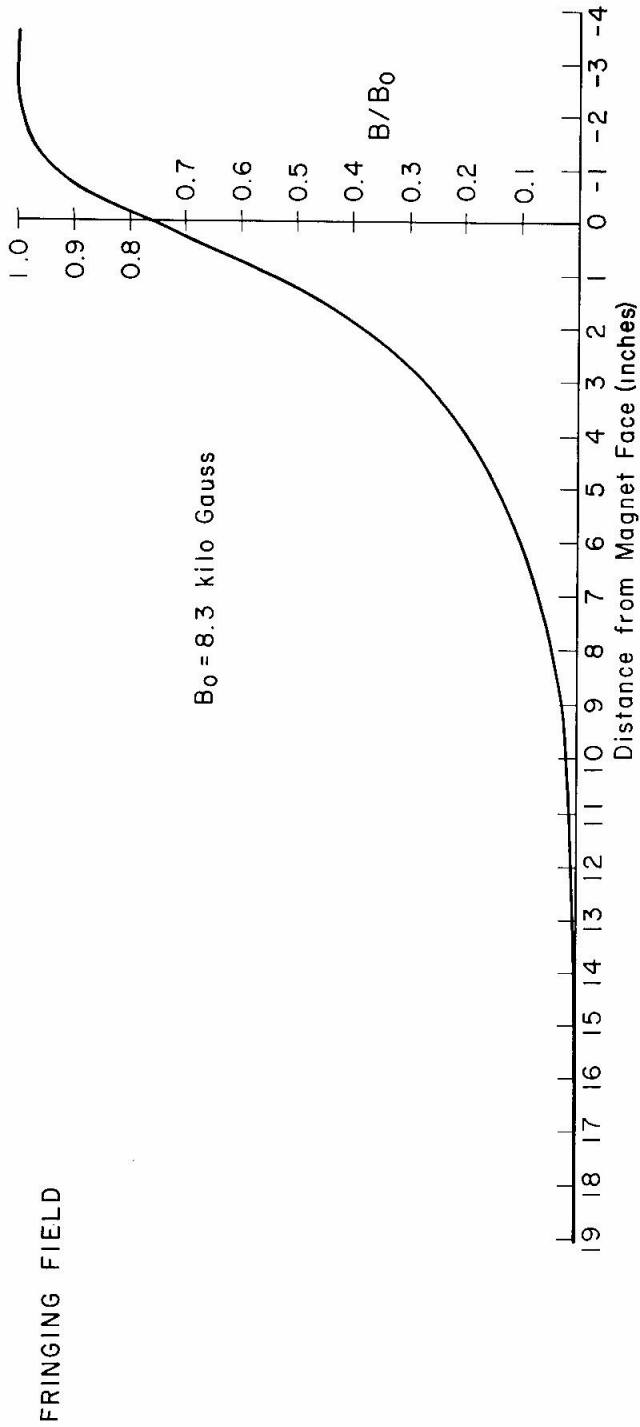


Fig. 5

Figure 6. Field Profiles.

Two different types of measurements of the field profile are shown with the pole piece profile. The upper four curves are measurements taken at the California Institute of Technology with a Hall emf generator. The curves for 6.28, 8.45, and 11.28 kiloGauss have been shifted down by 5 per cent, 10 per cent, and 15 per cent, respectively, to avoid the overlapping of the curves. The field parameters α and β obtained by a least squares analysis of the profiles are found in Table 2. The lower three curves are the logarithmic-derivative as measured by Spectromagnetic Industries. The value of the log-derivative at $r = r_0$ gives α ; the value of the slope at $r = r_0$ gives β . These measurements are also found in Table 2. See text: page 13.

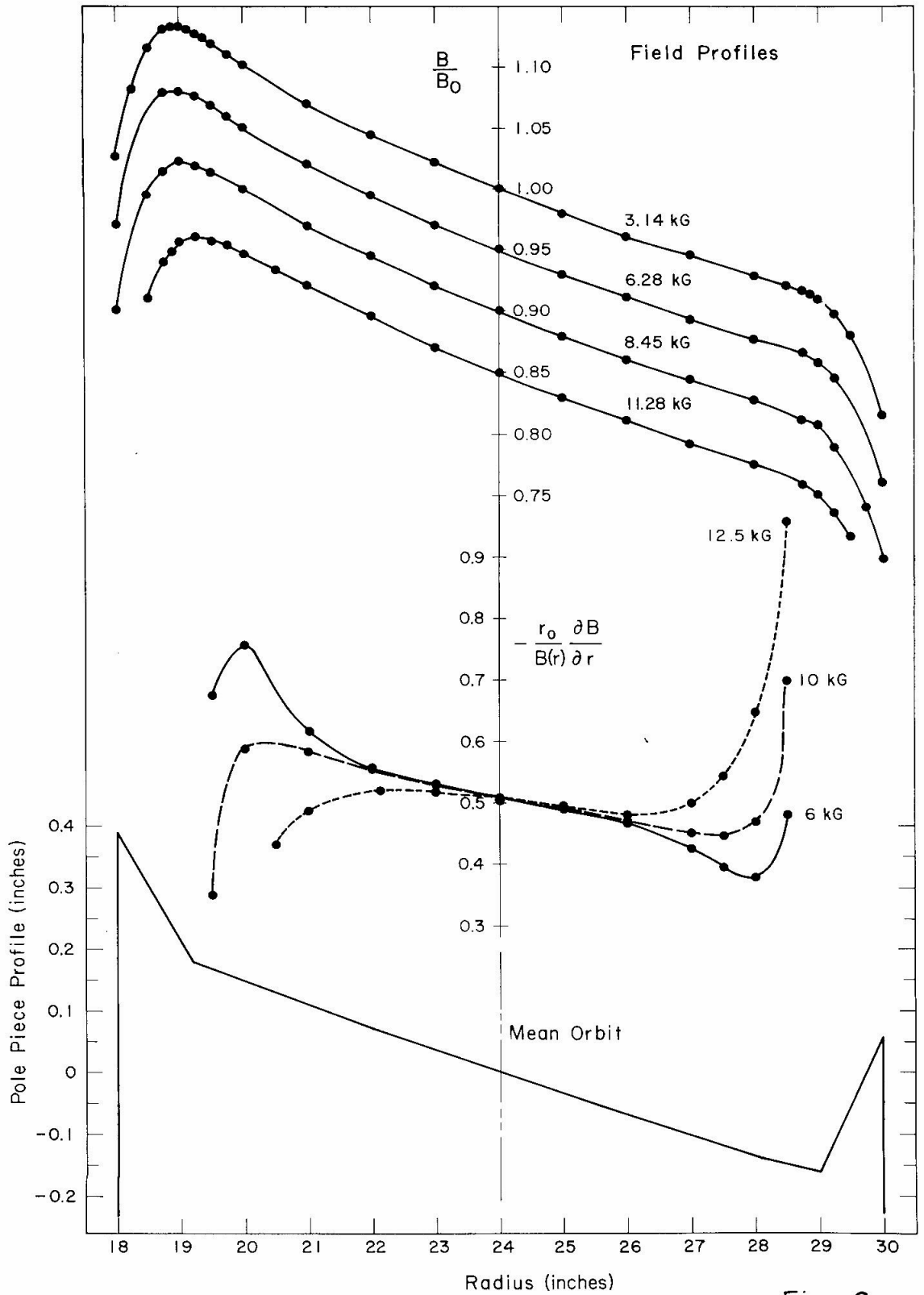
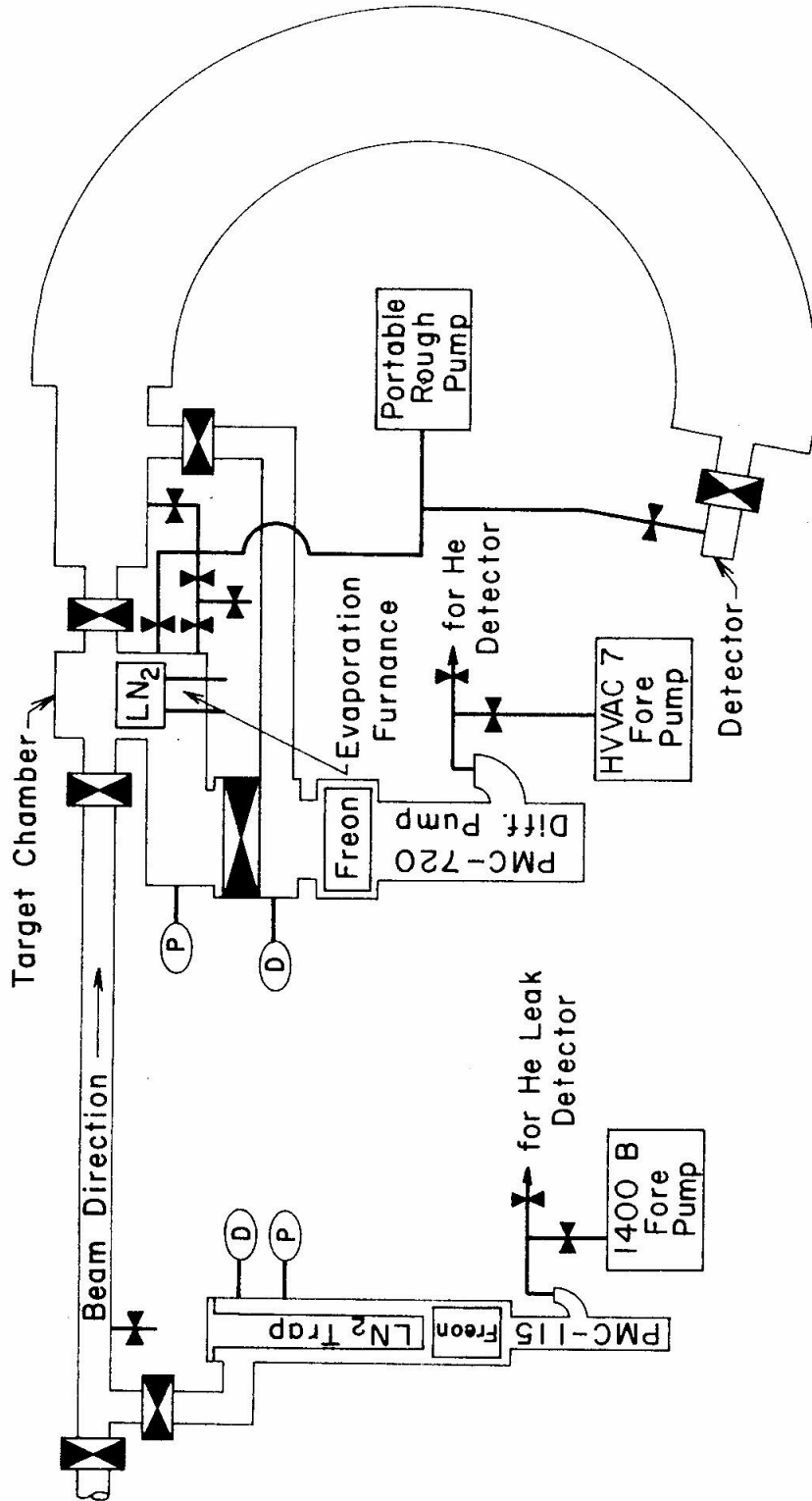


Fig. 6

Figure 7. Schematic Layout of the Vacuum Systems.

The layout for the two vacuum systems used with the spectrometer is shown schematically. The characteristics of each component are listed in Table 3. See text: pages 15 and 27.




- (D) = GPH-100A Discharge Gauge
 (P) = GP-105 Pirani Gauge
 or  = Vacuum Valve
 Freon = BC Series Freon Cooled Trap
 LN₂ = Liquid Nitrogen Cooled Trap
- Vacuum Systems

Fig. 7

Figure 8. Vacuum Box and Baffles.

Cross-section views of the vacuum box are shown. The vacuum box was made 190° in extent to allow for the additional bending of the beam in the fringing field. Phosphor-bronze baffles are placed just outside the limiting orbits. These baffles reduce the scattering of particles that strike the walls of the vacuum box. The locations of the NMR probes are indicated. See text: page 16.

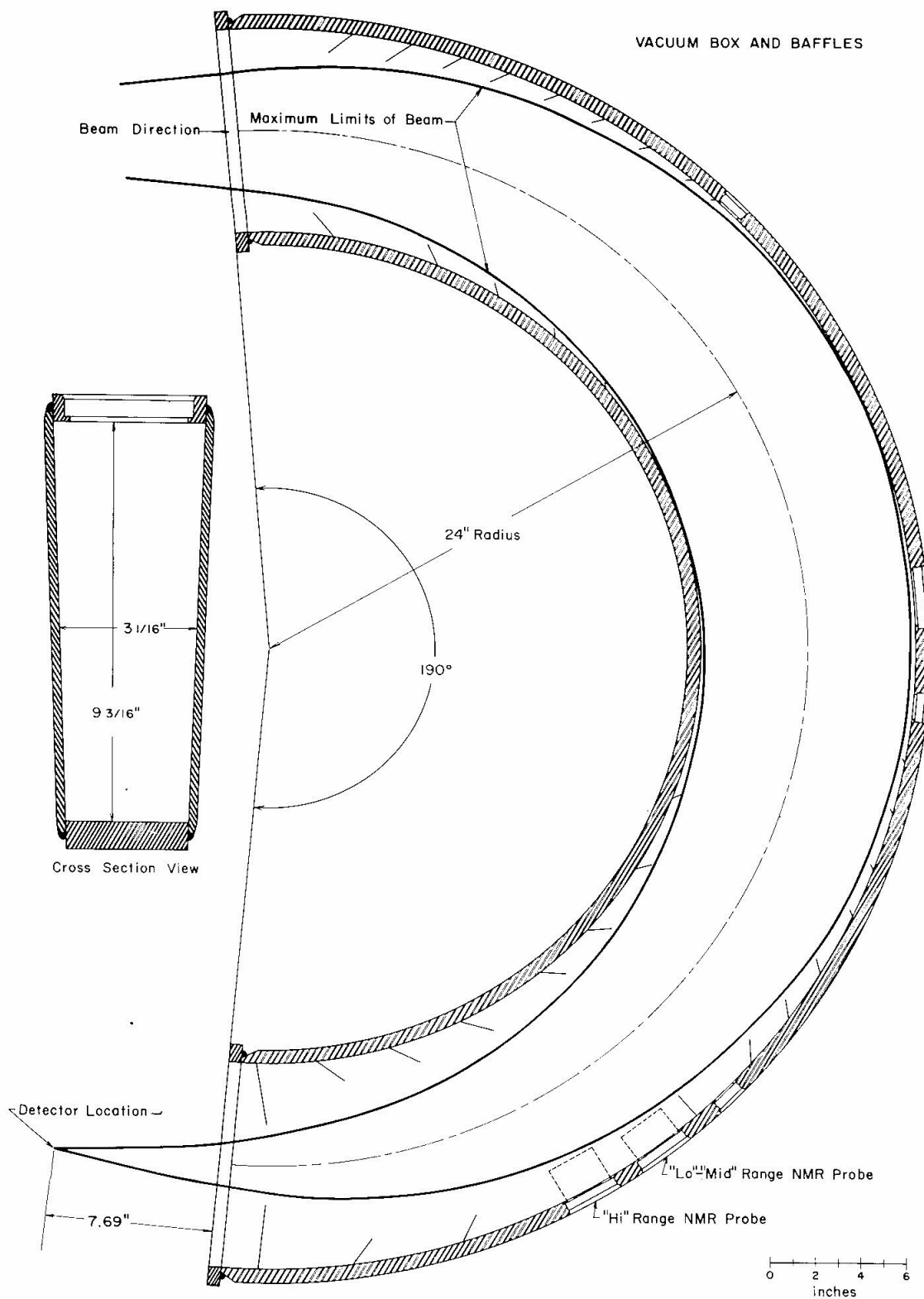


Fig. 8

Figure 9. Spectrometer Entrance Slits.

A cutaway view of the spectrometer entrance slits is shown. Four individually adjustable slits form a rectangular aperture of any size at any position in front of the spectrometer. These slits are composed of 0.020-inch thick tantalum pieces which are pivoted about horizontal and vertical axes. The true slit angles with respect to the mean ray are readily positioned by means of the slit angle readings. A coarse adjustment of 10° increments and a fine adjustment of 5" (minutes) increments are provided. Figures 10 and 11 and Table 4 give the conversion between the readings and the true angles. See text: page 17.

ENTRANCE SLITS

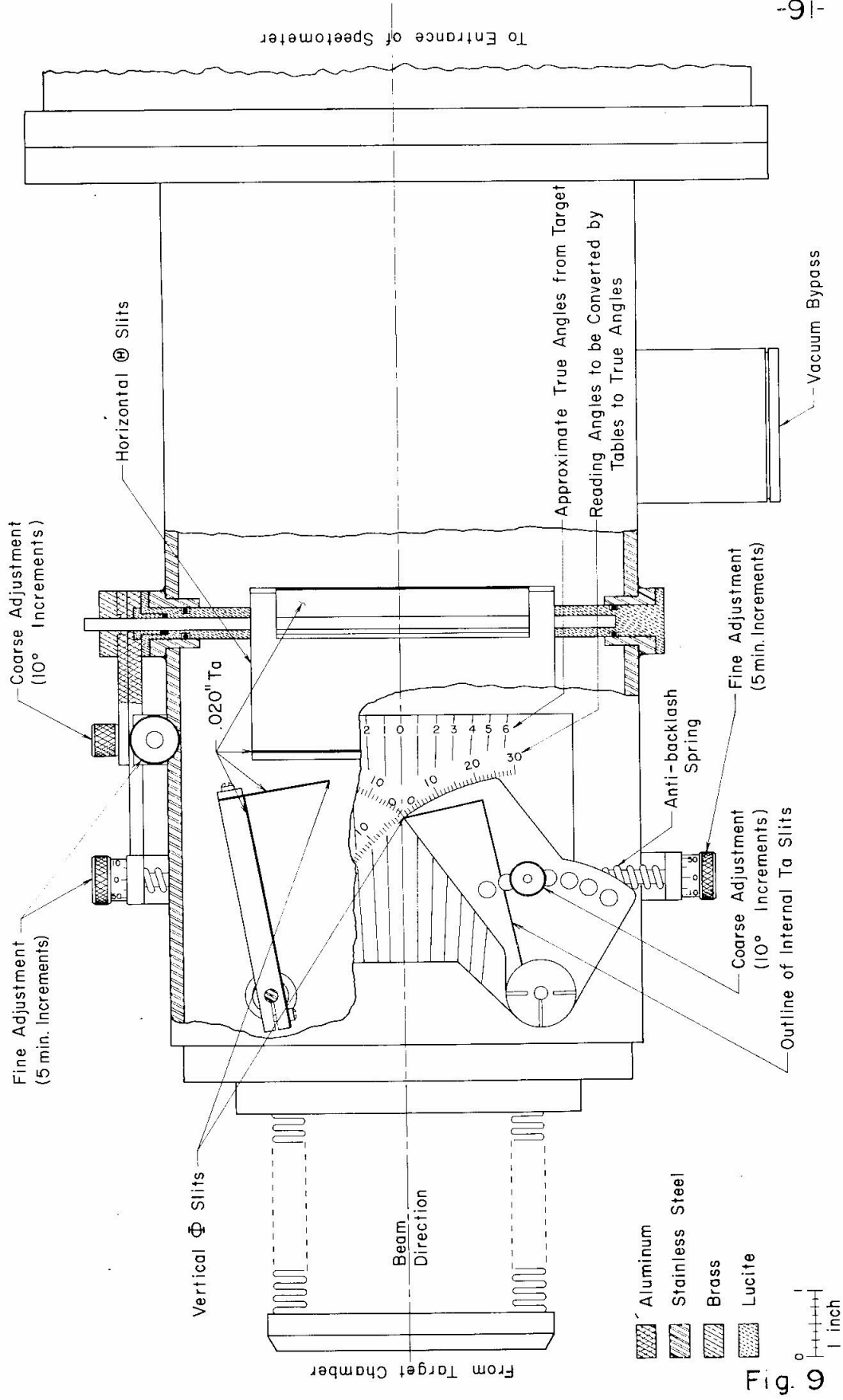


Figure 10. True Slit Angles Versus Slit Readings.

The conversions between the Θ and Φ slit edge readings and the true Θ and Φ angles from the mean ray are plotted. Negative angles are taken to be when the slit edge has crossed over the mean ray. See Table 4 and text: page 17.

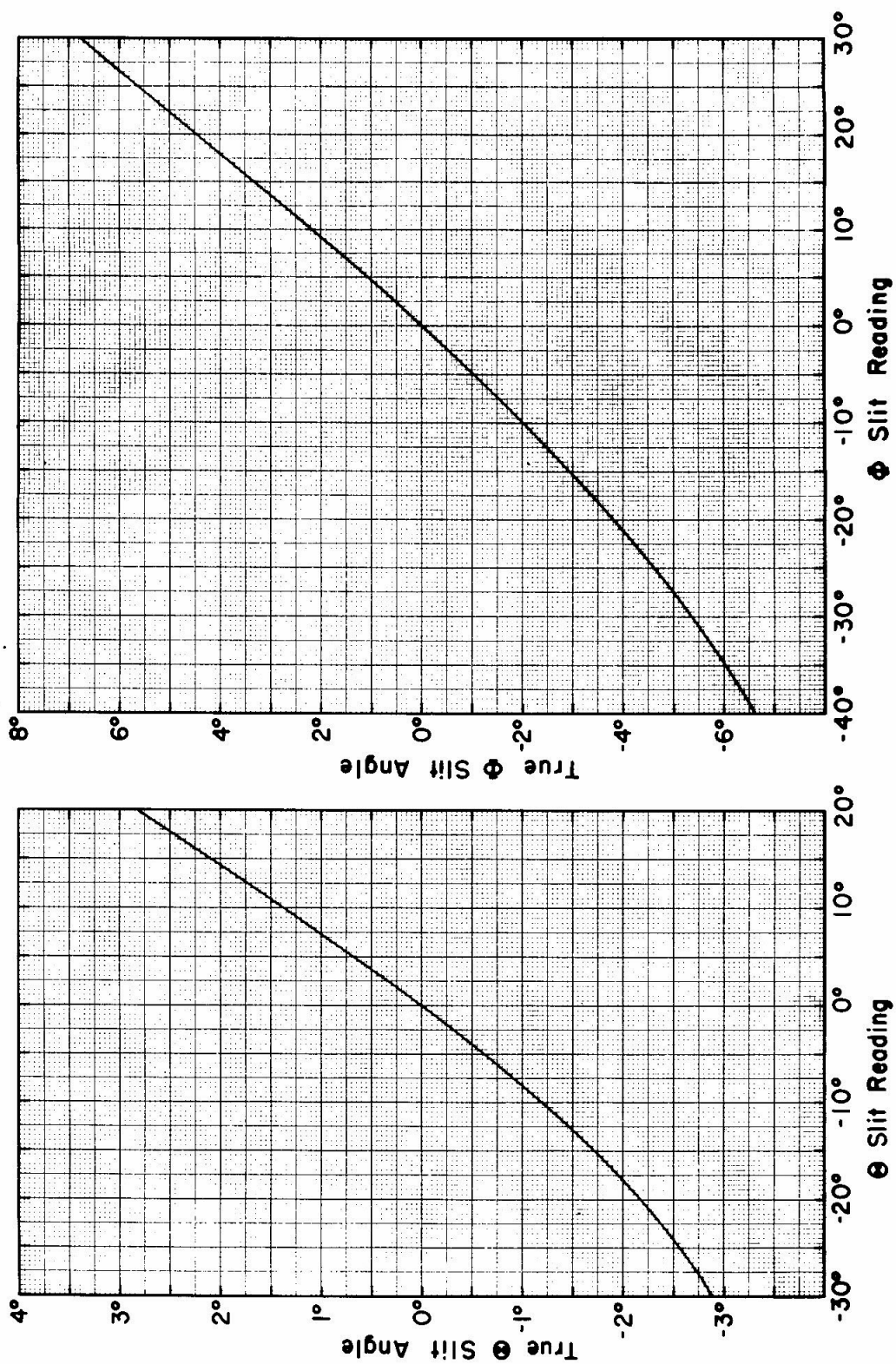


Fig. 10

Figure 11. Delta Theta Due to Phi Versus Theta.

The total broadening $\Delta\theta$ due to the finite aperture in the ϕ direction is shown plotted versus the spectrometer angle θ . These values were calculated assuming zero aperture width in the θ direction. See Table 5 for numerical values, and see text: page 18.

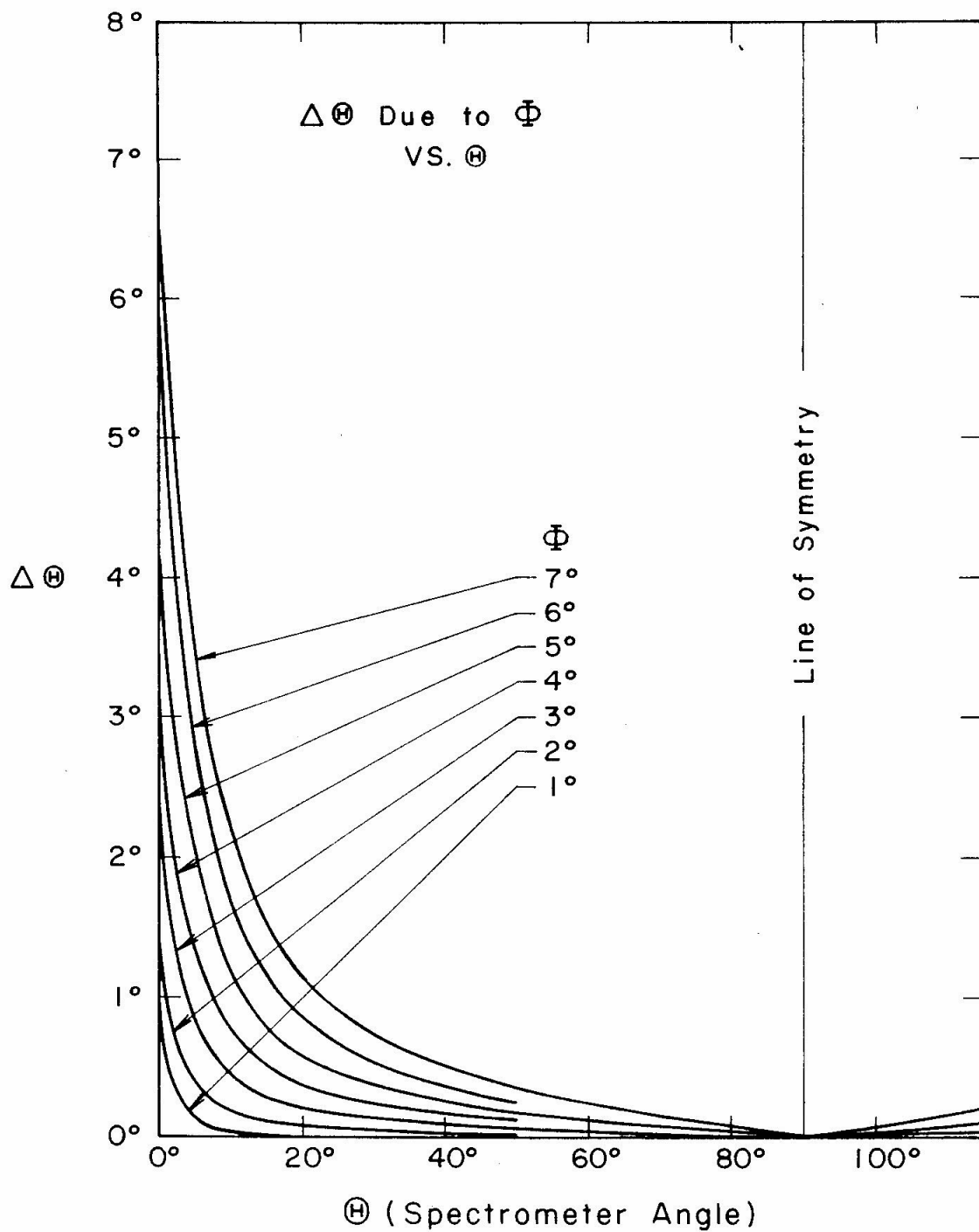


Fig. II

Figure 12. Alignment.

The configuration used to align the spectrometer target chamber is shown with other details concerning alignment. A set of quartz crosshairs and its image in a pool of mercury form a vertical axis through the central support bearing and consequently form the vertical axis of rotation of the spectrometer. An alignment telescope positioned concentric with the axis of the target chamber is used to determine when the chamber is positioned correctly. See text: pages 18 and 28.

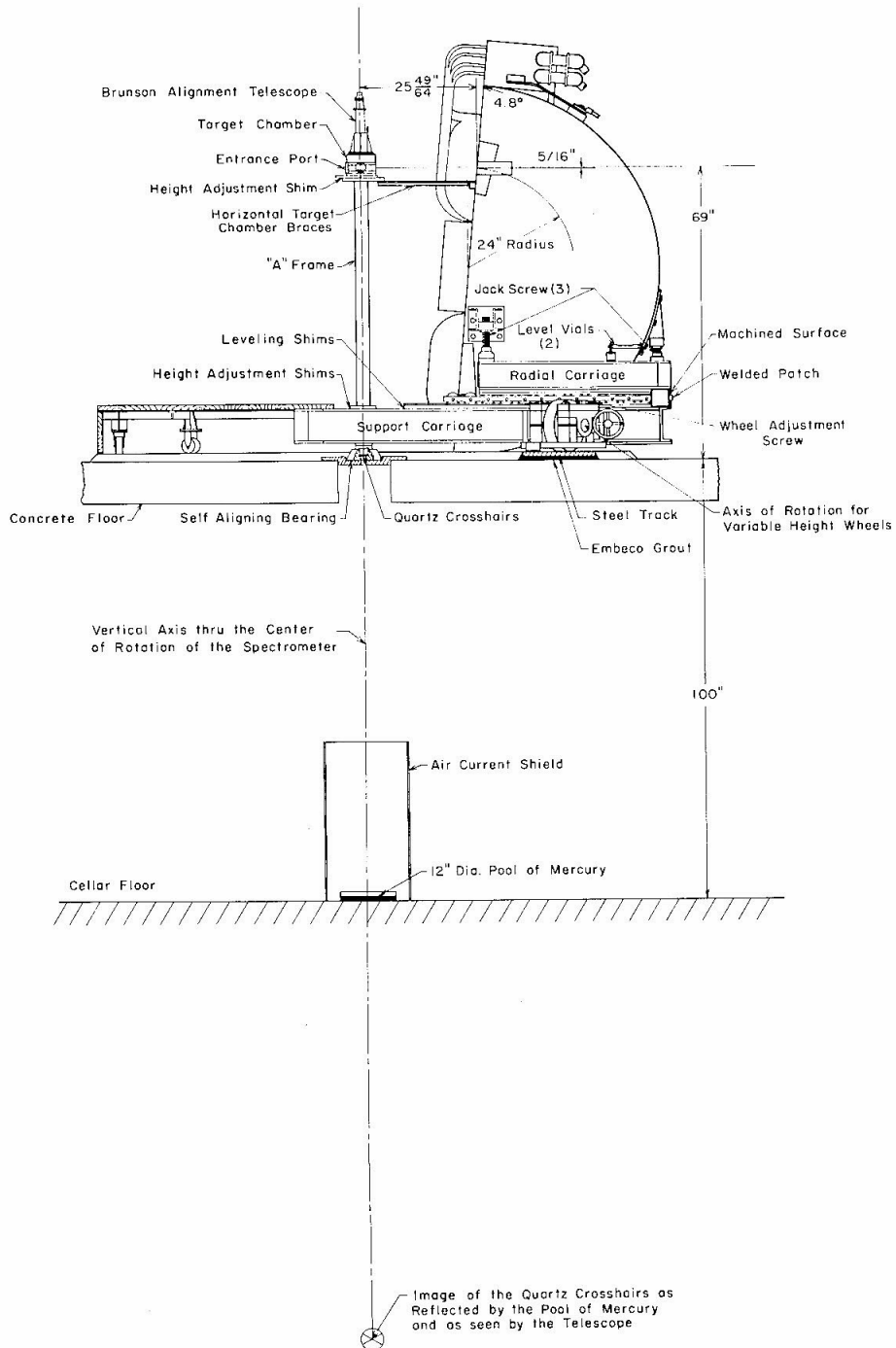


Fig. 12

Figure 13. Horizontal Displacement of the Target Chamber.

The horizontal displacement of the target chamber perpendicular to the beam direction is plotted versus spectrometer angle. The open circles were taken without adjustment of any kind. The solid circles were taken after adjusting the variable wheel supports to bring the level bubbles back on center. See text: page 19.

Vertical Runout of the Track After Grouting.

The measured vertical runout of the spectrometer base track after the grouting into position is plotted versus track angle. Before grouting, the maximum excursion was ± 0.005 inches. The values here are measured relative to the value at 300° . See text: page 19.

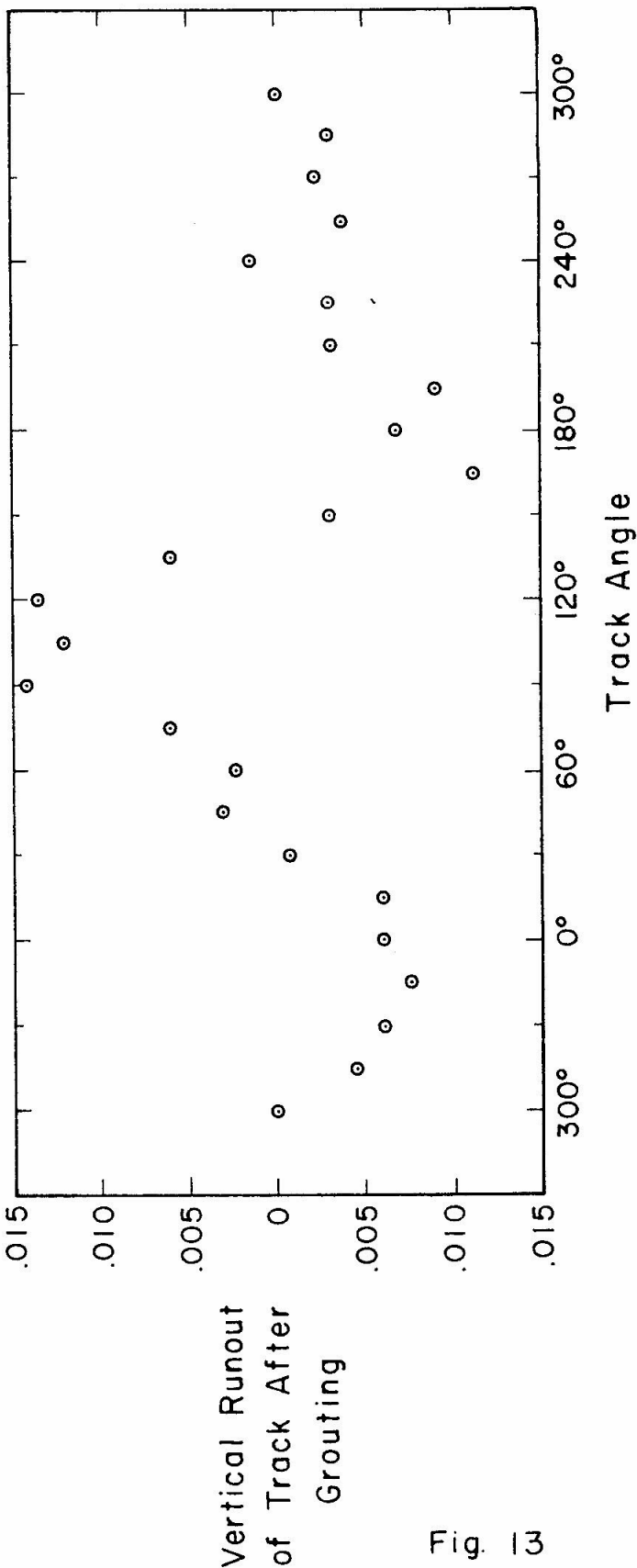
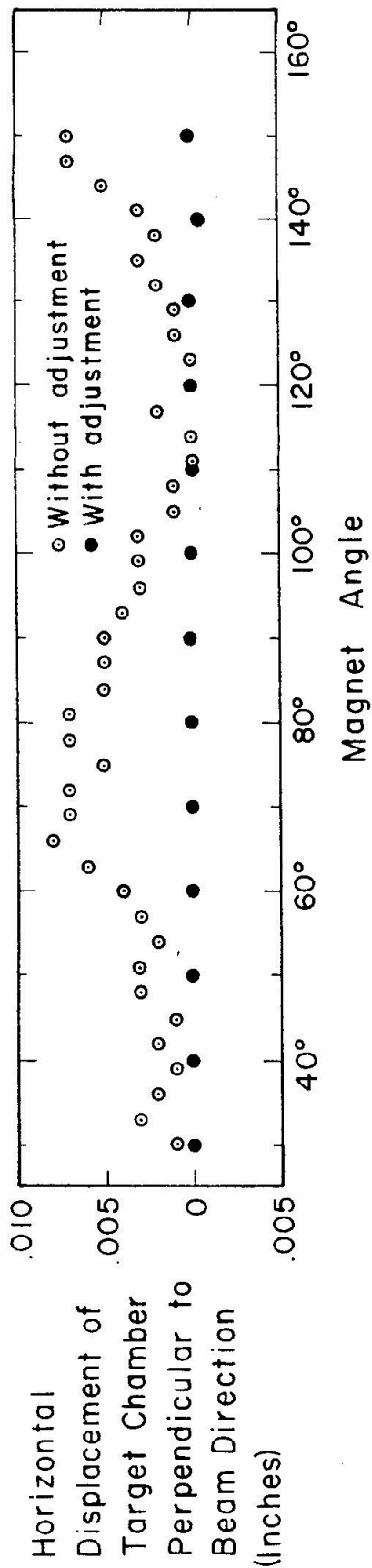


Fig. 13

Note: Before Grouting ± 0.005 Max. Excursion

Figure 14. Ray Tracing Layout.

The layout for the ray tracing measurements is shown. See Figure 15 for a schematic view of the use of the equipment. See text: page 21.

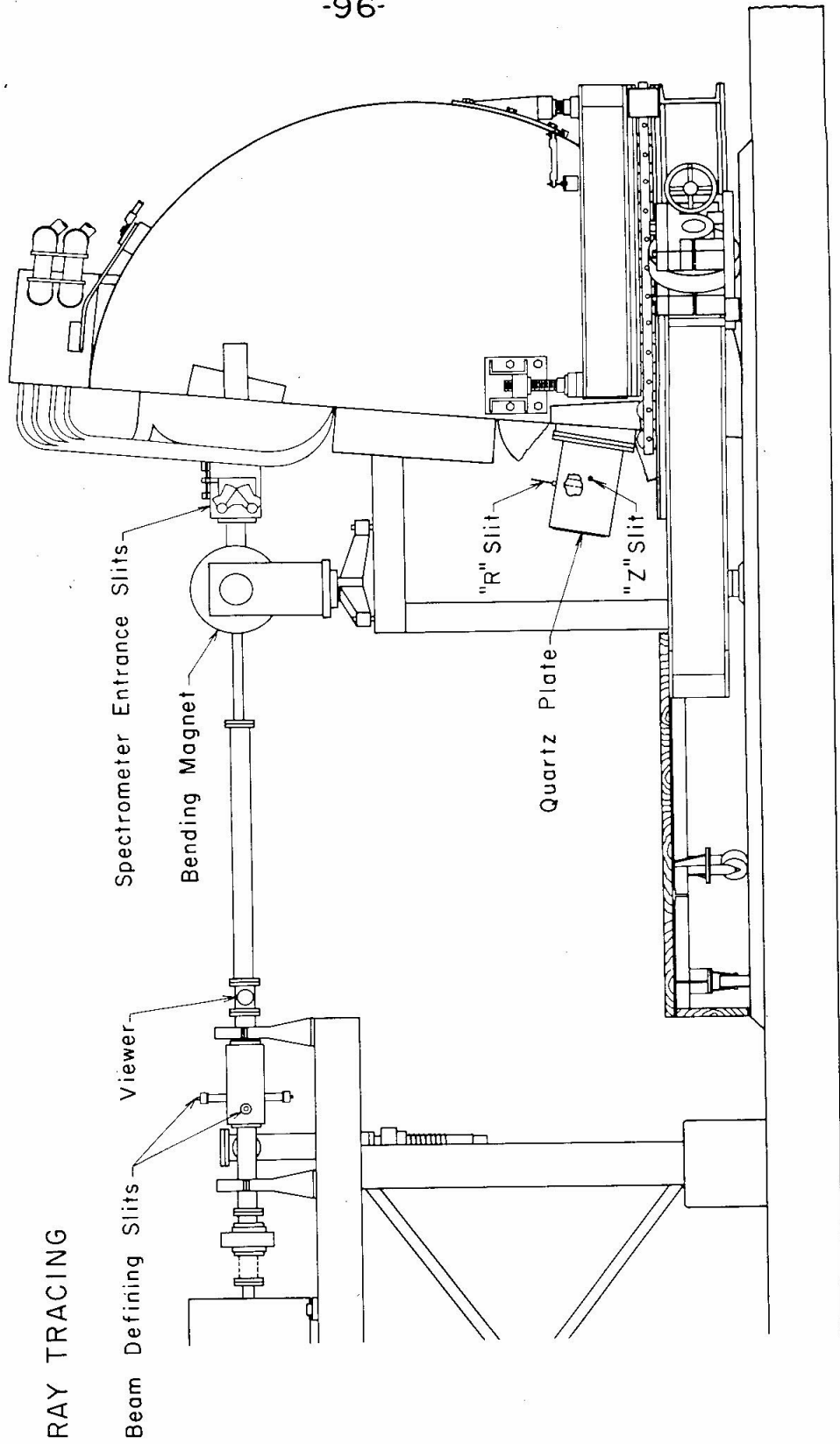


Fig. 14

Figure 15. Ray Tracing Schematic.

Here, presented in a schematic view, is the layout shown in Figure 14. At the target position, the auxiliary magnet bends the beam of charged particles from the tandem accelerator into the various ϕ angles that the spectrometer aperture can accept. Each ray of charged particles appears to be coming from a point source. Near the detector location (image position), a slit and a quartz plate in a box as shown determine the direction and position of the emerging beam. In this way, the focus and focal plane can be found, one ray at a time. The radii of the pole tip entrances are also indicated. See text: page 23.

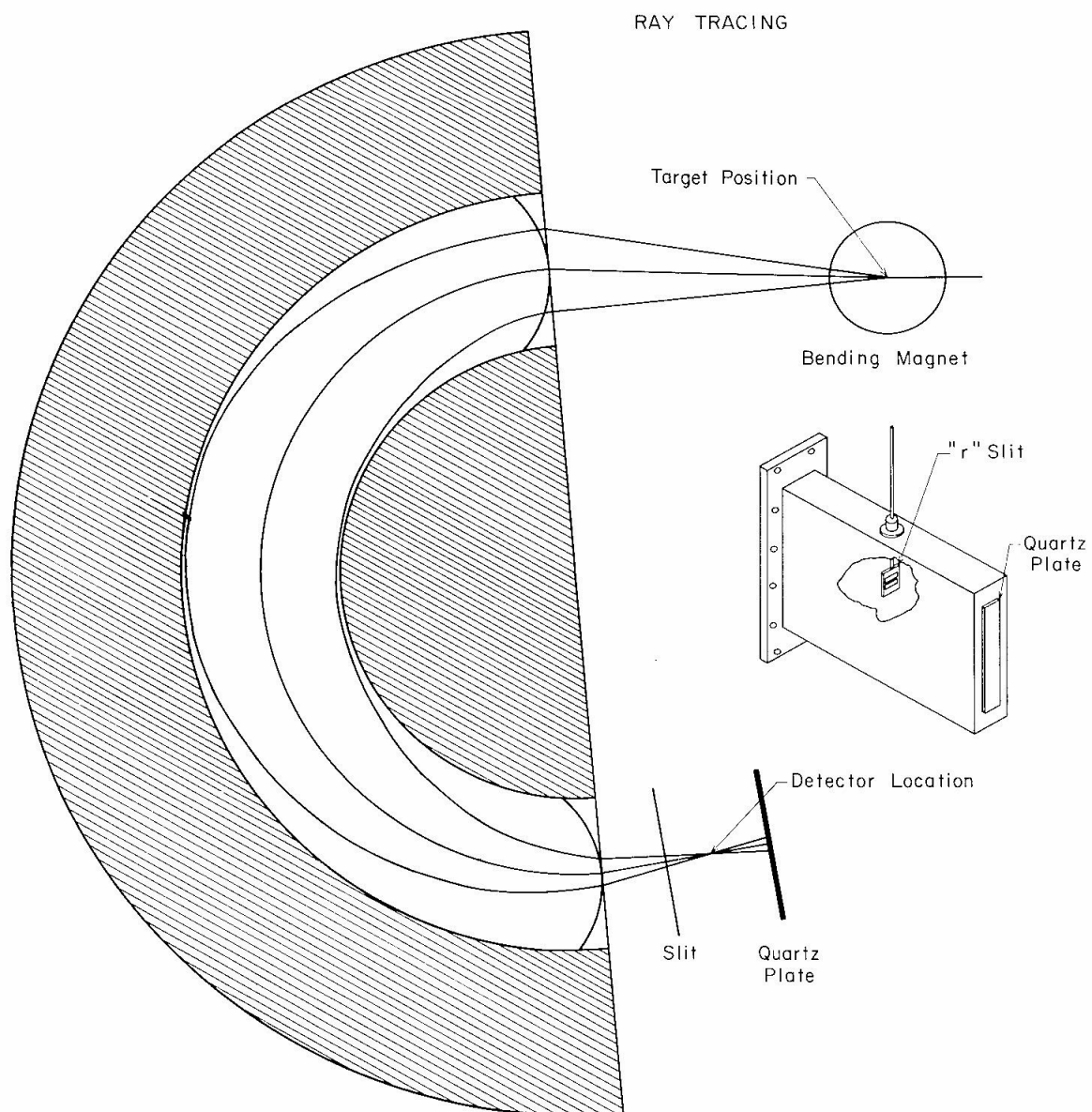
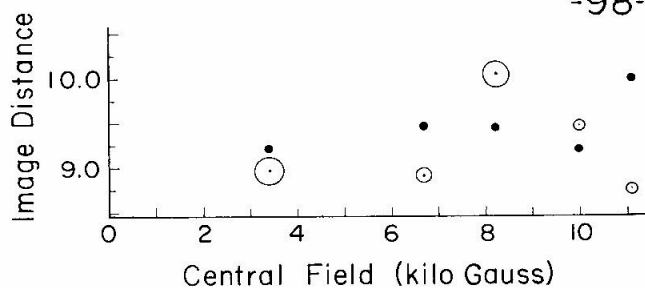
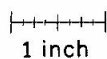


Fig. 15

Figure 16. Foci - 14.5-Inch Radius Pole Tips

The foci of the initial ray tracing measurements are shown for several fields. The "slit" and "quartz" represent the positions of the r slit and the quartz plate in the ray tracing box shown in Figure 15. The paths emerge from the spectrometer on the left, go through the slit, and are stopped on the quartz plate. From the slit position and the beam spot on the quartz plate, the direction of the emerging ray is determined. The auxiliary magnet bends the beam of charged particles from the tandem accelerator into the various ϕ angles in the spectrometer entrance aperture. This produces the different emerging rays which form a focus at the image of the spectrometer. The small graph in the upper right hand corner shows the image distance from the edge of the magnet for various fields. The small solid circles represent the image distance as found from the inner five rays; these measurements should be independent of aberrations. The open circles represent the image distance for all the rays measured; the diameter of the circles represents the minimum confusion in the r direction. Similar measurements for 9-inch radius pole tips are shown in Figure 17. See text: page 23.

Foci 14.5" R. Pole Tips



○ Focal point of all rays
 • Focal point of inner rays only
 (Size of circle represents total aberrations)

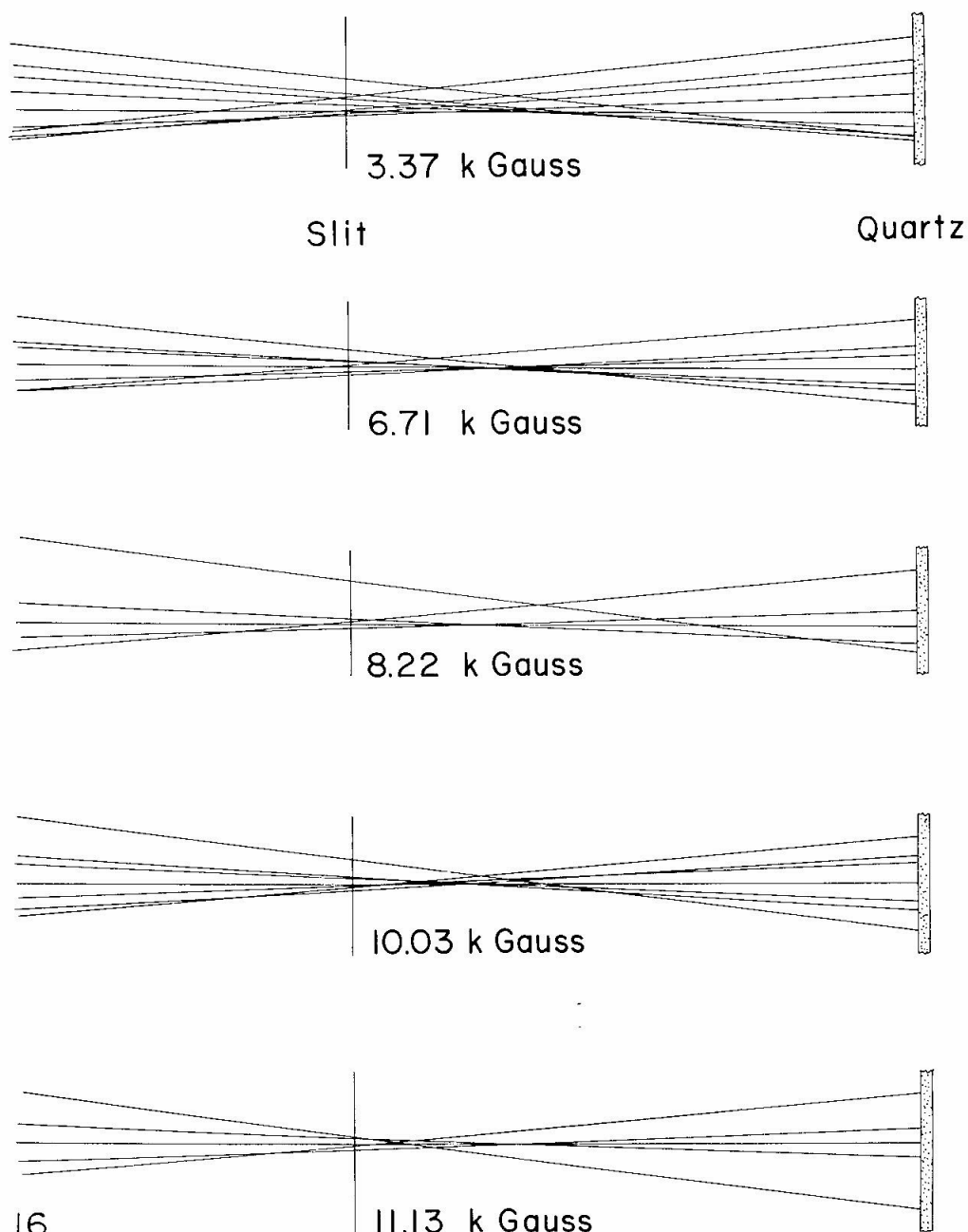
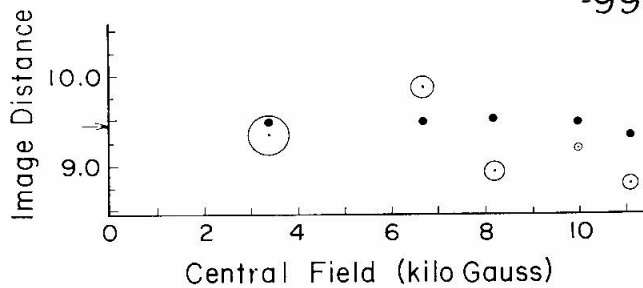
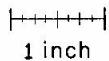


Fig. 16

Figure 17. Foci - 9-Inch Radius Pole Tips.

The foci of the final ray tracing measurements are shown for several fields. See Figure 16 for a discussion of these measurements. The small arrow on the ordinate of the graph represents the position at which the detector slits were placed. See text: page 23.

Foci 9" R. Pole Tips



- Focal point of all rays
- Focal point of inner rays only
- (Size of circle represents total aberrations)

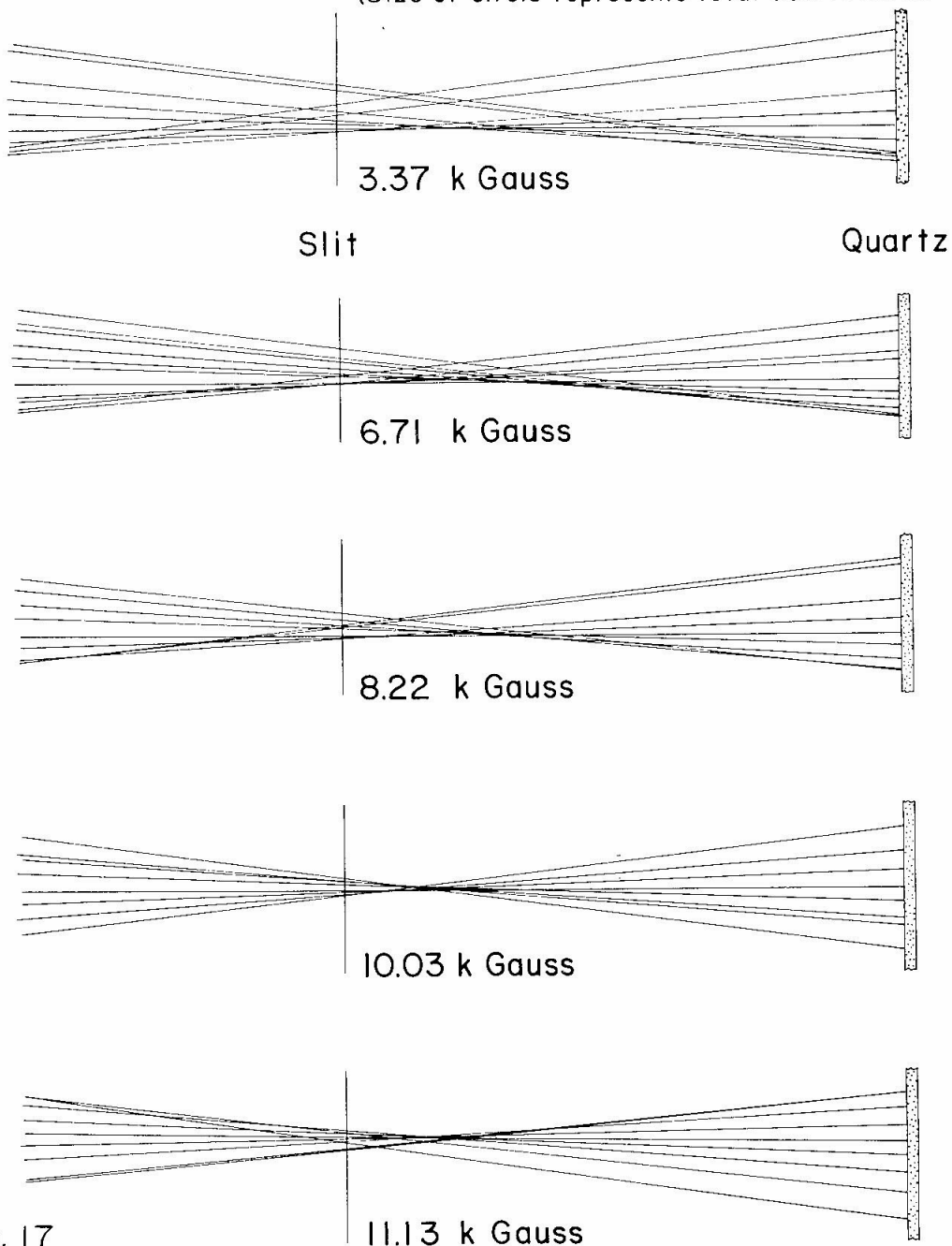


Fig. 17

Figure 18. Focal Planes at 3.37 Kilogauss.

Two focal planes with mean fields of 3.37 kilogauss are shown. The focal plane was measured by determining five different foci at different spectrometer fields for the same incoming beam energy. The upper focal plane measurement was taken with the original 14.5-inch radius entrance pole tips; the bottom plane was measured with the final 9-inch radius pole tips. See text: page 23.

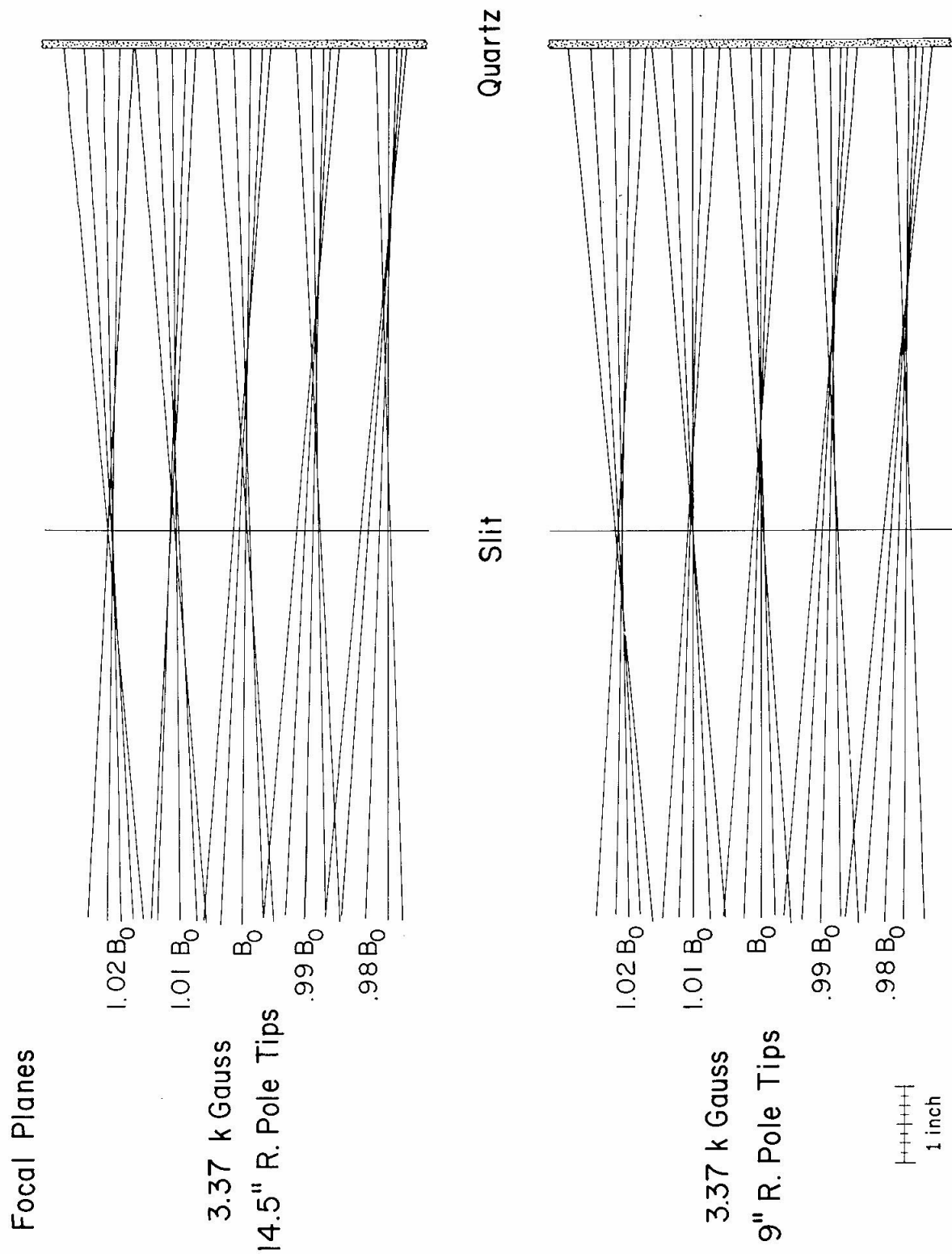


Fig. 18

Figure 19. Focal Planes at 6.71 and 8.22 Kilogauss.

Two focal planes with mean fields of 6.71 and 8.22 kilogauss are shown. See Figure 18 for a discussion of these measurements. See text: page 23.

Focal Planes
9" R. Pole Tips

1.02 B_0

1.01 B_0

B_0

.99 B_0

.98 B_0

6.71 k Gauss

Slit

Quartz

1.02 B_0

1.01 B_0

B_0

.99 B_0

.98 B_0

8.22 k Gauss

1 inch

Fig. 19

Figure 20. Focal Planes at 10.03 and 11.13 Kilogauss.

Two focal planes with mean fields of 10.03 and 11.13 kilogauss are shown. See Figure 18 for a discussion of these measurements. See text: page 23.

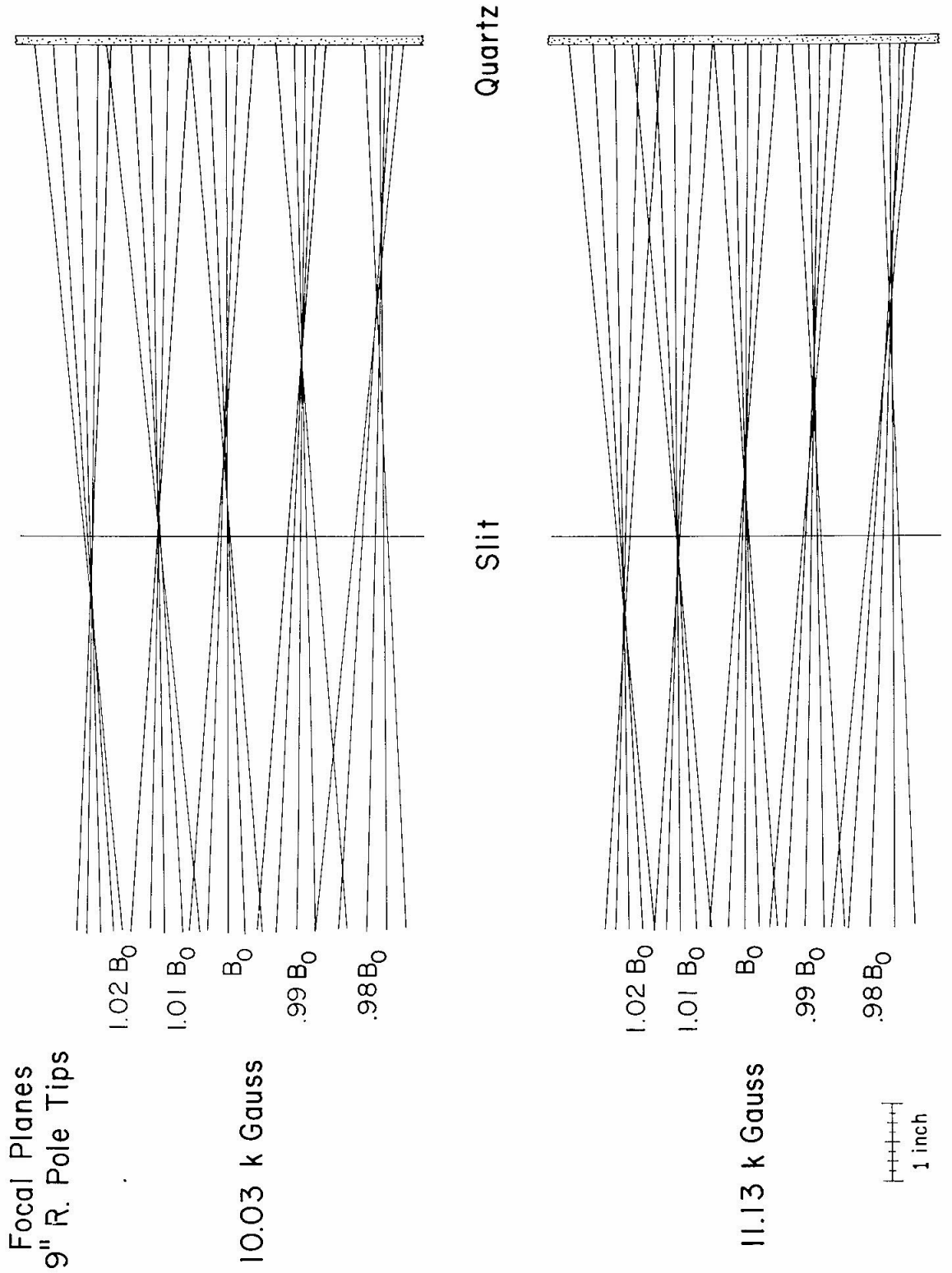


Fig. 20

Figure 21. Z Foci.

Focal points in the z direction for various fields are shown. These foci were measured in a manner similar to the measurements of the r foci shown in Figure 16. Although these measurements were done with the 14.5-inch radius entrance pole tips, the results should be the same for the 9-inch radius pole tips. The foci are practically independent of field and have very little aberrations. The partial focal plane measured for 8.22 kilogauss is parallel to the face of the magnet. See text: page 24.

Z Foci

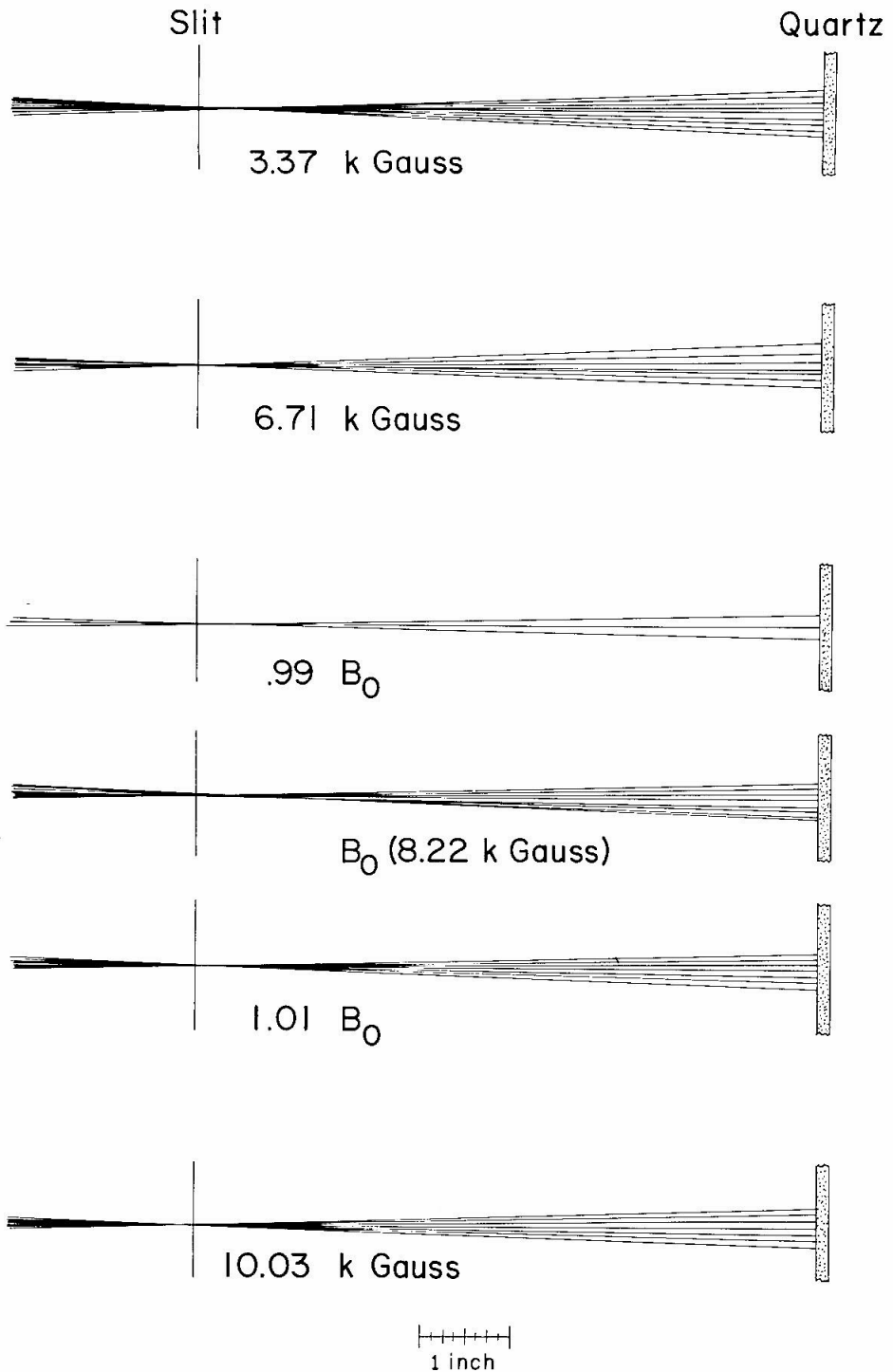


Fig. 21

Figure 22. Dispersion Measurements.

A typical dispersion measurement is shown at the top of the figure. With the auxiliary bending magnet off, the spectrometer field is varied by small increments; the positions of the emerging rays are determined by the method outlined in Figure 16. The displacement δr from the mean radius is plotted versus the change in magnetic field (NMR frequency); the slope of the line gives the dispersion of the spectrometer. At the bottom of the figure, the dispersion measurements are plotted versus the central magnetic field for both the 14.5- and 9-inch radius entrance pole tip radii. See text: page 25.

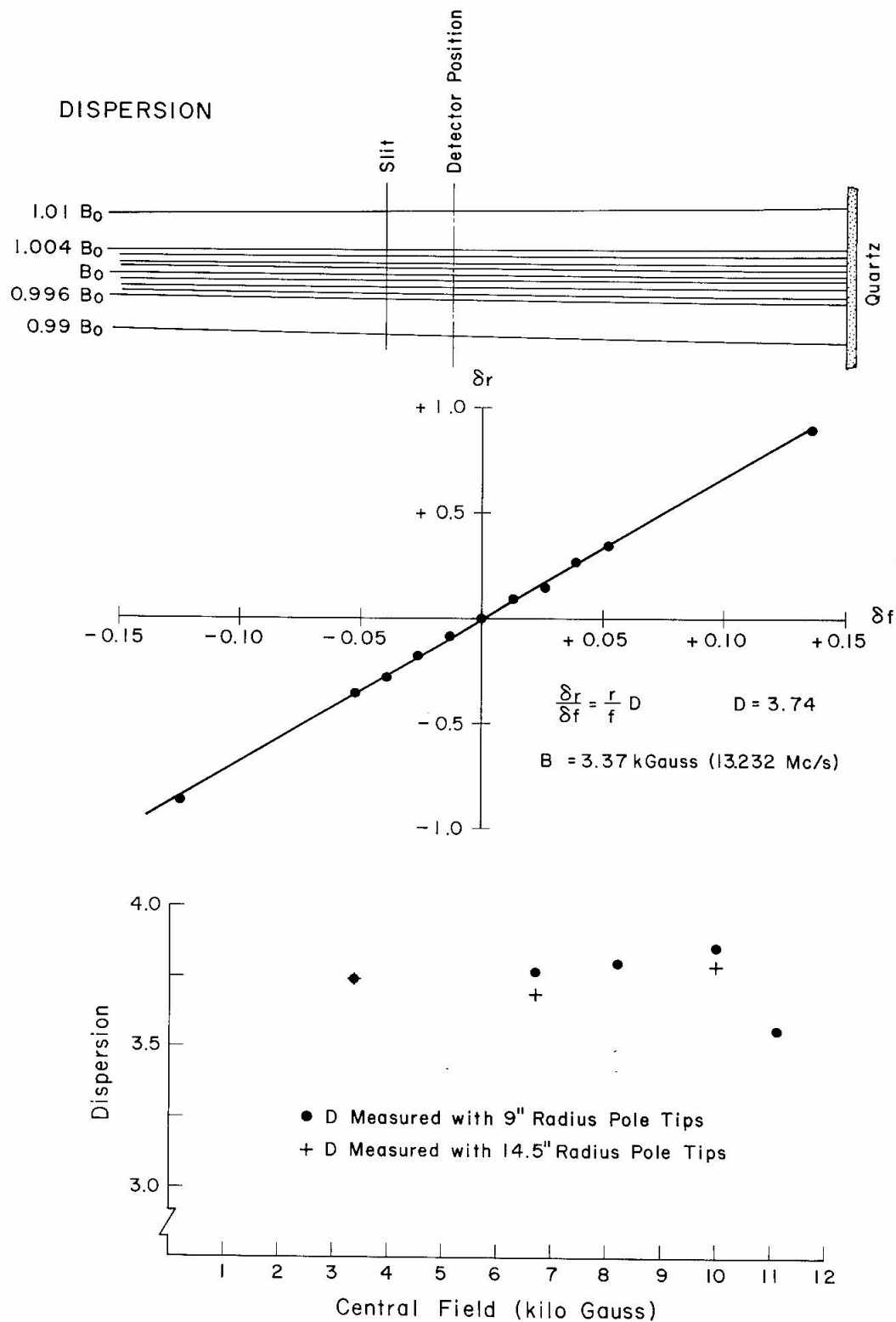


Fig. 22

Figure 23. Target Chamber and Evaporation Furnace.

A cross section is shown for the target chamber and evaporation furnace when the spectrometer is located at 0° to the beam. All significant parts are labeled. See text: page 26.

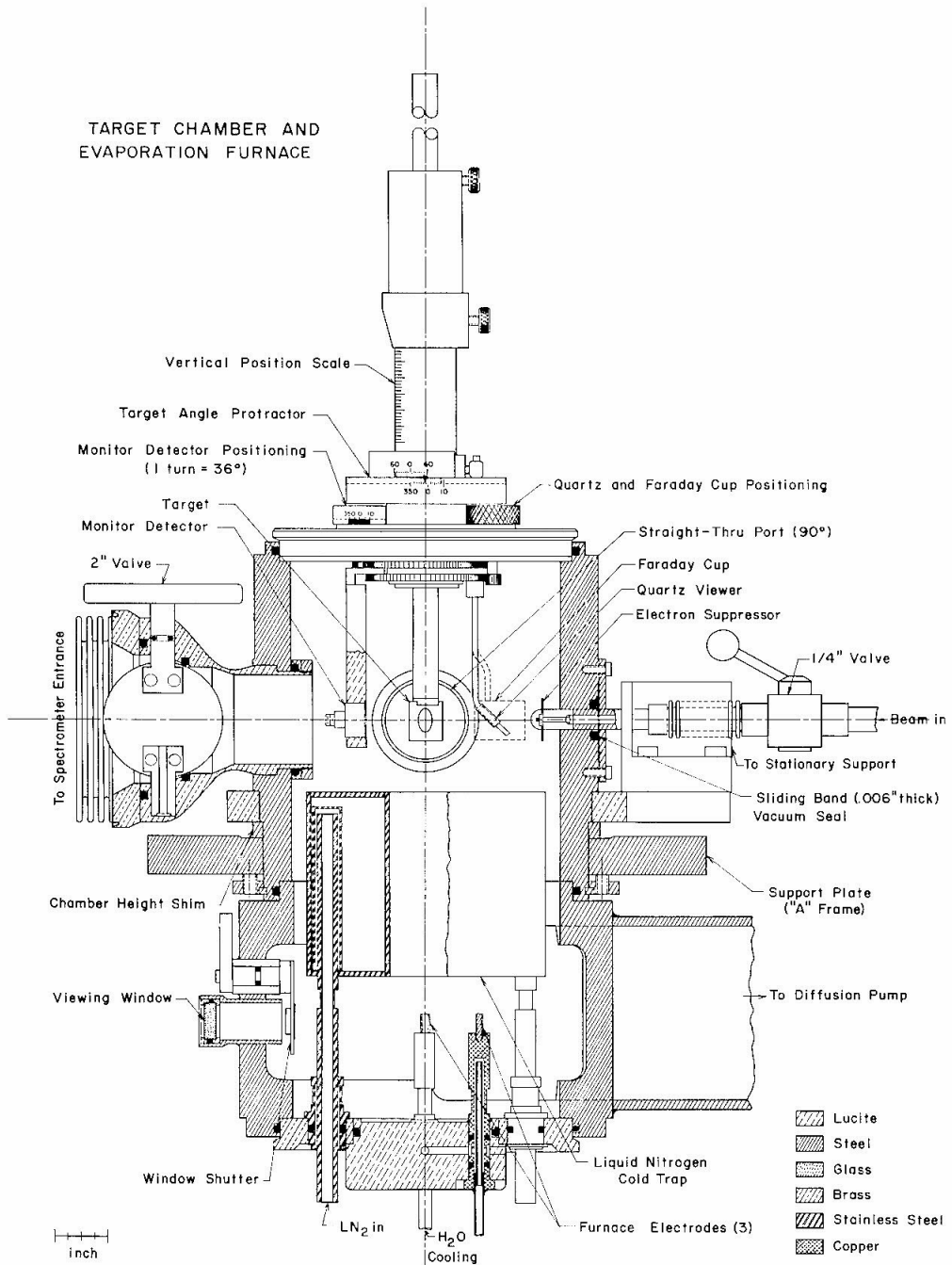


Fig. 23

Figure 24. Typical Spectrometer Detector Spectrum.

This energy spectrum was obtained in a silicon surface barrier detector located at the image of the spectrometer from the reaction $\text{Be}^9(\text{p}, \alpha)\text{Li}^6$. The four different particle groups (the α 's have two different charge states) have the same magnetic rigidity. Their energies, however, are in the ratio Z^2/A to the energy of the proton as given in the table. The detector thickness was purposely made thinner than the range of these protons in silicon by changing the electrical bias across the detector. In this way, the proton and the α^{++} peak were separated. See text: page 30.

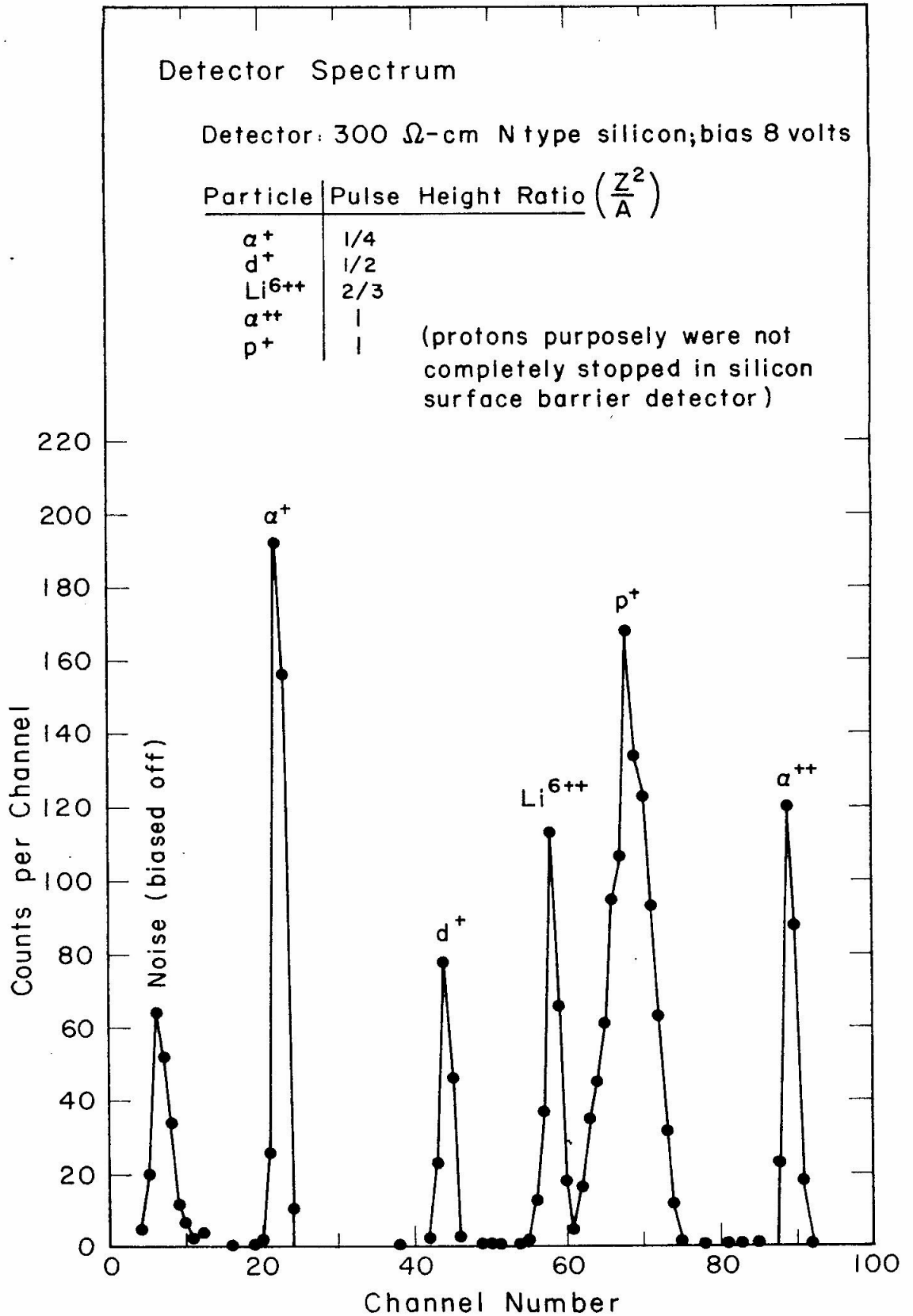


Fig. 24

Figure 25. Detection and Counting Electronics.

A typical electronic setup for charged particle detection and counting is shown. See text: page 31.

DETECTION AND COUNTING ELECTRONICS

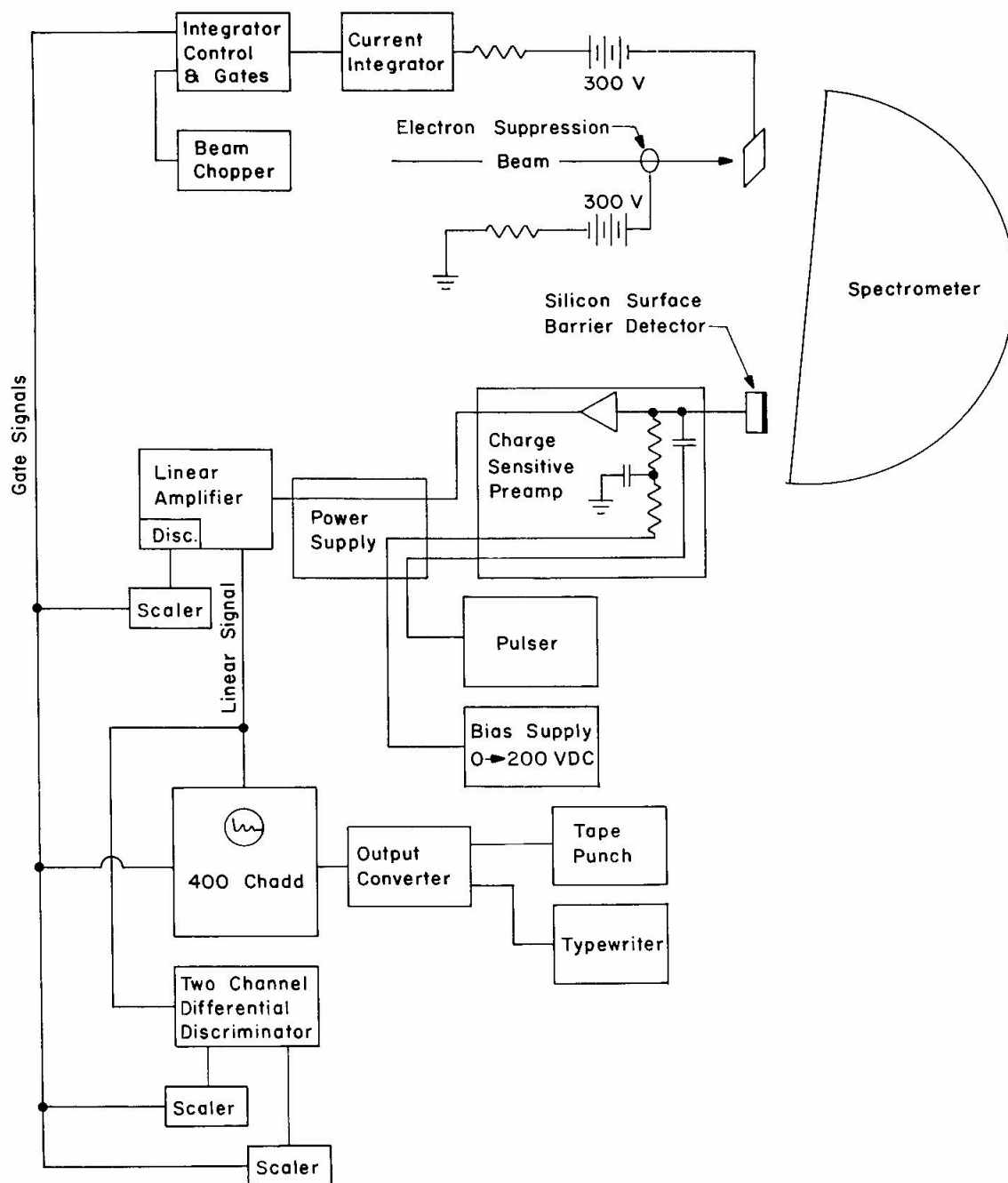


Fig. 25

Figure 26. Solid-State Detector Spectrum of Thorium B's Daughters.

The decay scheme of Thoron gas is shown. The radioactive sources prepared for calibration purposes are made by collecting Thoron gas on the end of a stainless steel rod and allowing it to recoil into the surface by the decays to Thorium B. The subsequent α decays are used to calibrate the spectrometer. A solid-state detector spectrum of these decays is also shown. This detector is typical of the several used in the target chamber of the spectrometer for monitoring or coincidence work. See text: page 31.

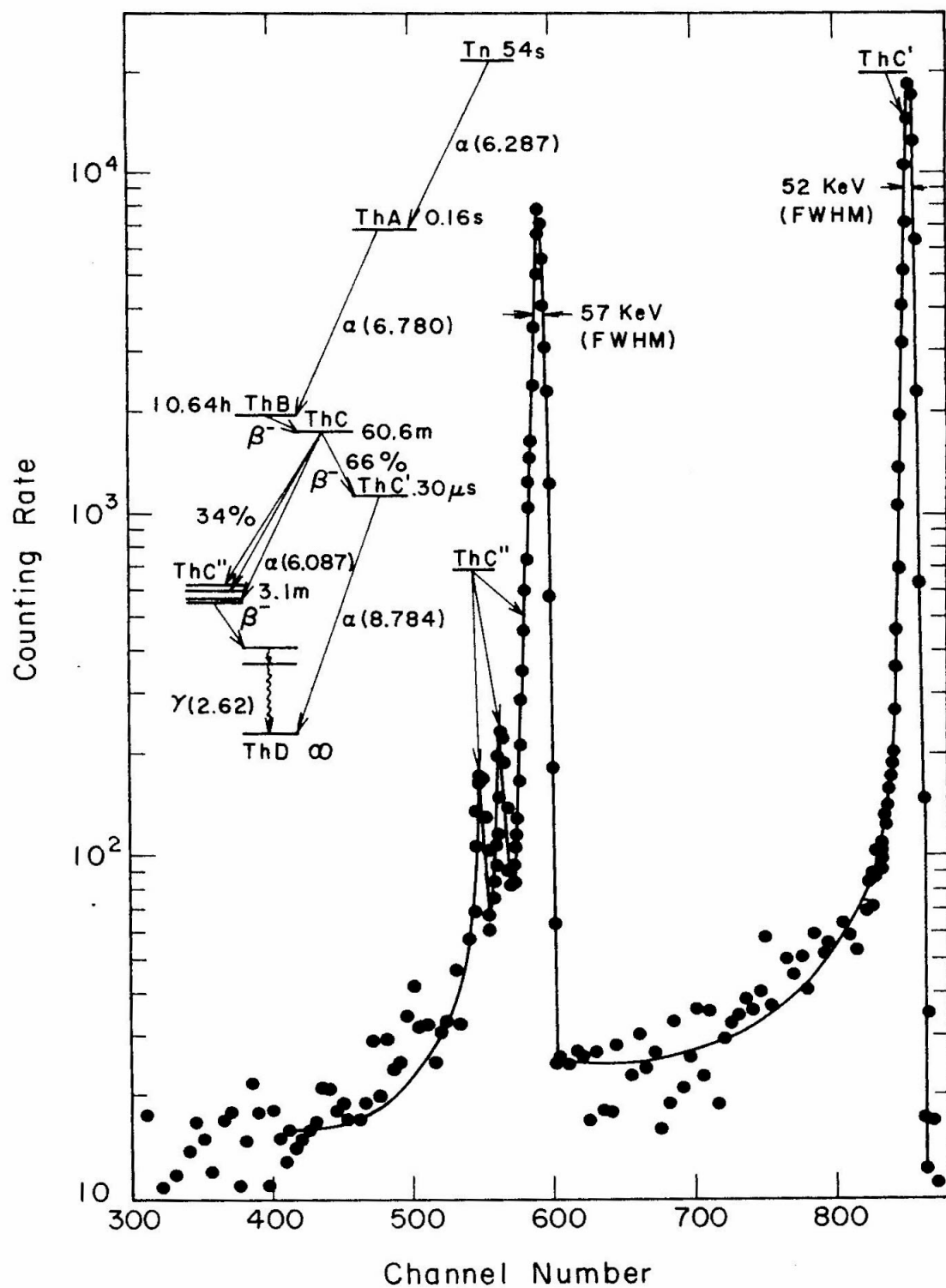


Fig. 26

Figure 27. Thorium C' Calibration Spectrum.

A typical calibration spectrum of the α^{++} particles from Thorium C' is shown (see Figure 26 for the decay scheme to Th C' from Th and the method of preparing a radioactive source) along with the source holder. The widths due to the source size and the detector slit are shown. From the peak value and using the given formula, the spectrometer constant K for protons can be calculated. See text: page 32.

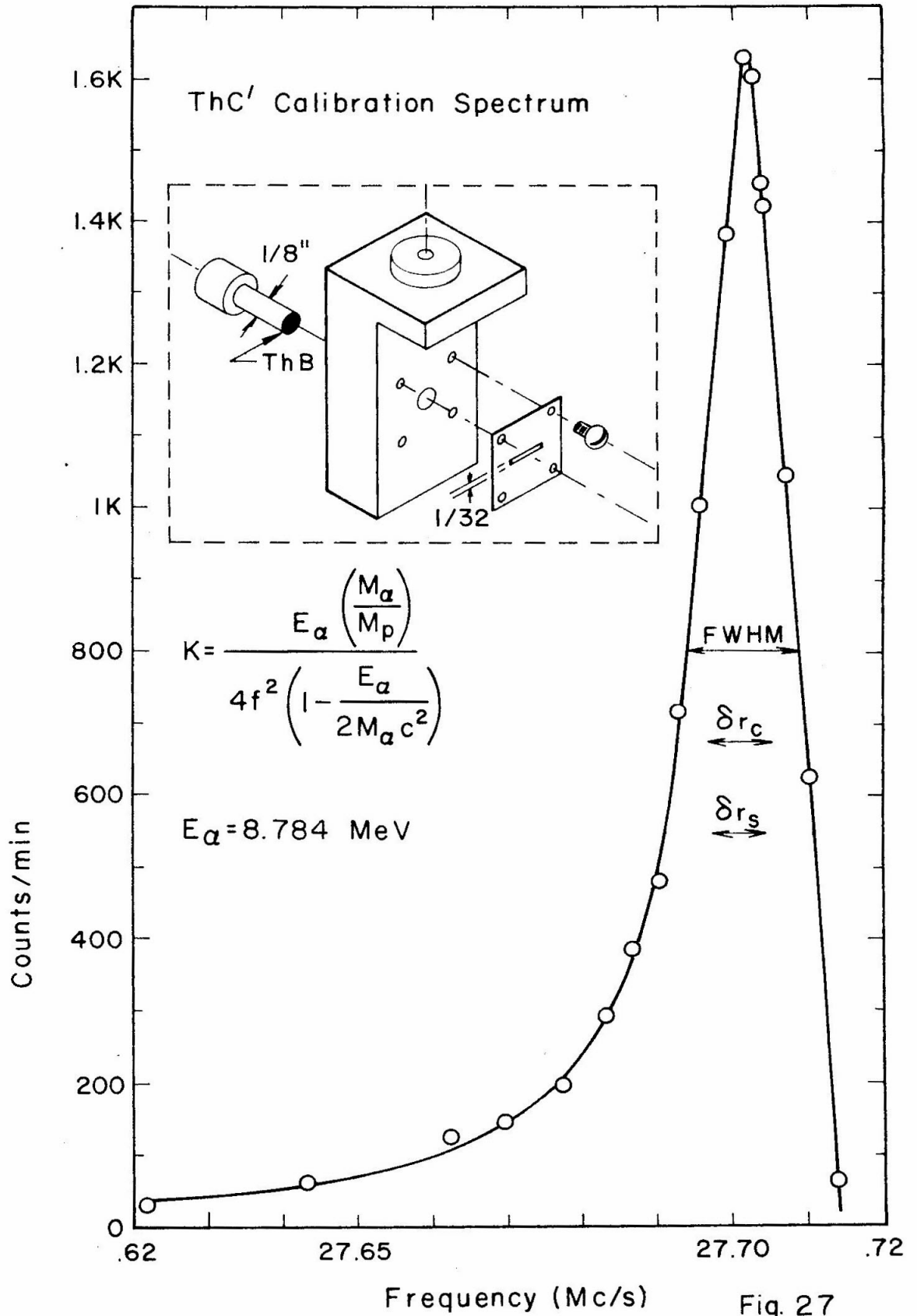


Fig. 27

Figure 28. Momentum Spectrum of Thorium C Alpha Particles.

The closely-spaced high-energy doublet from Th C is shown as measured by the spectrometer. Notice that this doublet is unresolved in Figure 26 which was taken with a solid-state detector alone. These peaks may also be used to calibrate the spectrometer as illustrated in Figure 27. See text: page 32.

Detector Counting Rate Versus Φ Slit Angle.

With the spectrometer field set to detect the peak of Th C', both Φ slits were closed; one Φ slit was withdrawn at a time, giving the plot of counting rate versus Φ slit angle for various values of the detector slit size δr_c . Φ^+ refers to those trajectories which have radii greater than the mean radius r_0 ; Φ^- , for radii less than r_0 . The radical difference between the Φ^+ results and the Φ^- results is due to the fact that the aberrations have quite different shapes for each. See text: page 35.

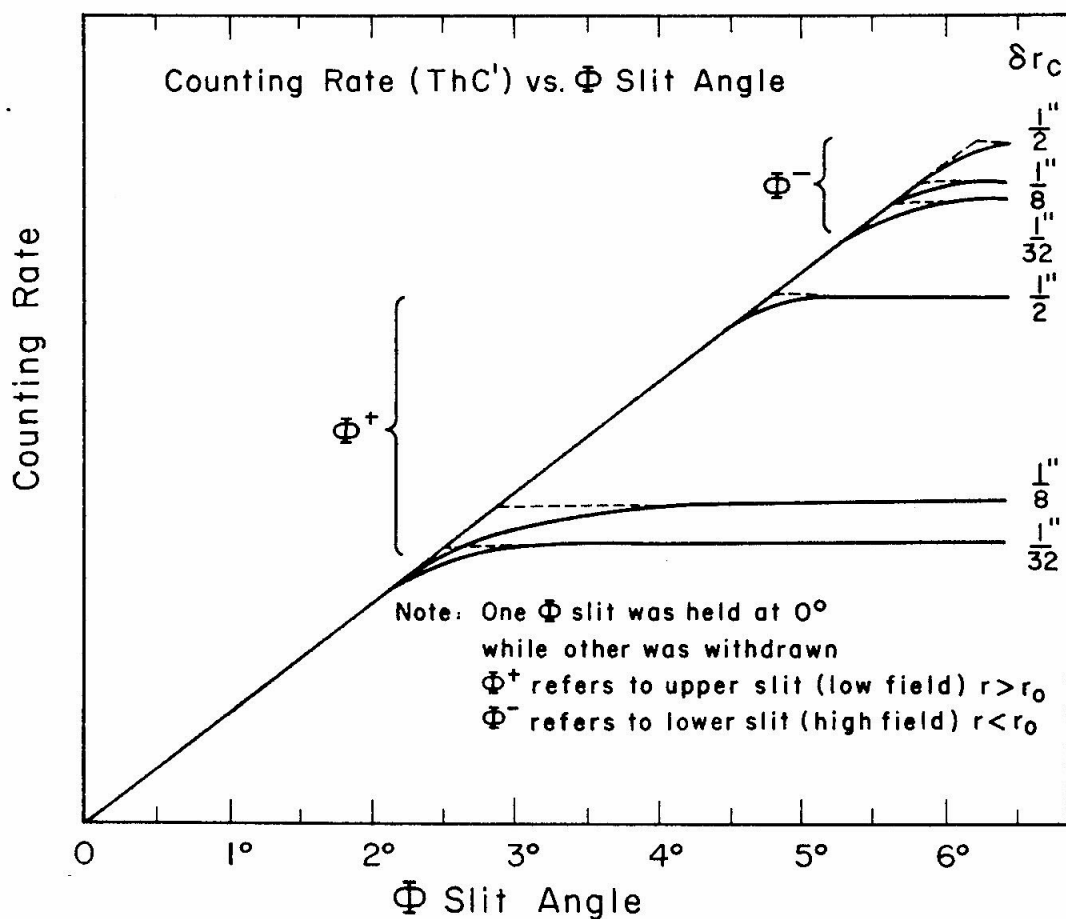
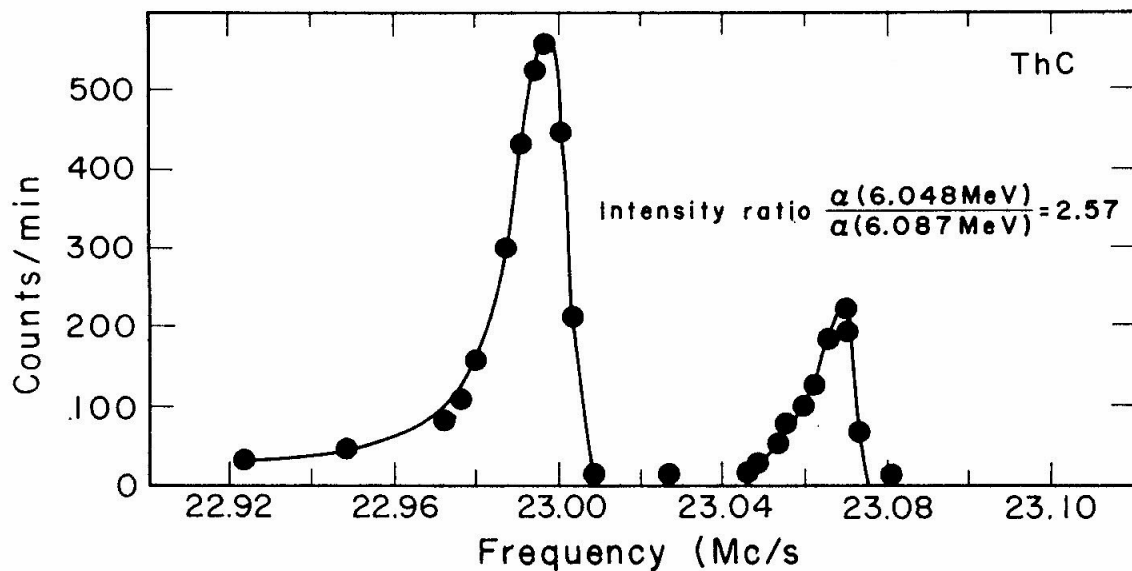


Fig. 28

Figure 29. Comparison of the Spectra Resulting from Different Source Collection Times.

The normalized peaks from two different Th B sources are shown. The solid curve shows the Th C' spectrum from a freshly-made source (less than four hours old). The dashed curve shows the same spectrum from a source that was about five days old. This spectrum has been shifted by amount $1/10^4$ and broadened by a factor of 1.6 . See text: page 32.

Demonstration of the Hysteresis of the Spectrometer.

The solid curve shows the Th C' spectrum after the spectrometer field had been brought from zero to the observation point (~ 7.5 kilogauss). The dashed curve shows the spectrum after the field had been brought down from 15.5 kilogauss to the observation point. The shift in the two spectra is about $1/3000$. Both spectra have been corrected for the 10.64 hour half life of Th B. The solid curve repeated well after the field had been brought back to zero again. The hysteresis observed is due to the combination of the hysteresis of the spectrometer iron and the hysteresis of the NMR magnetometer. See text: page 34.

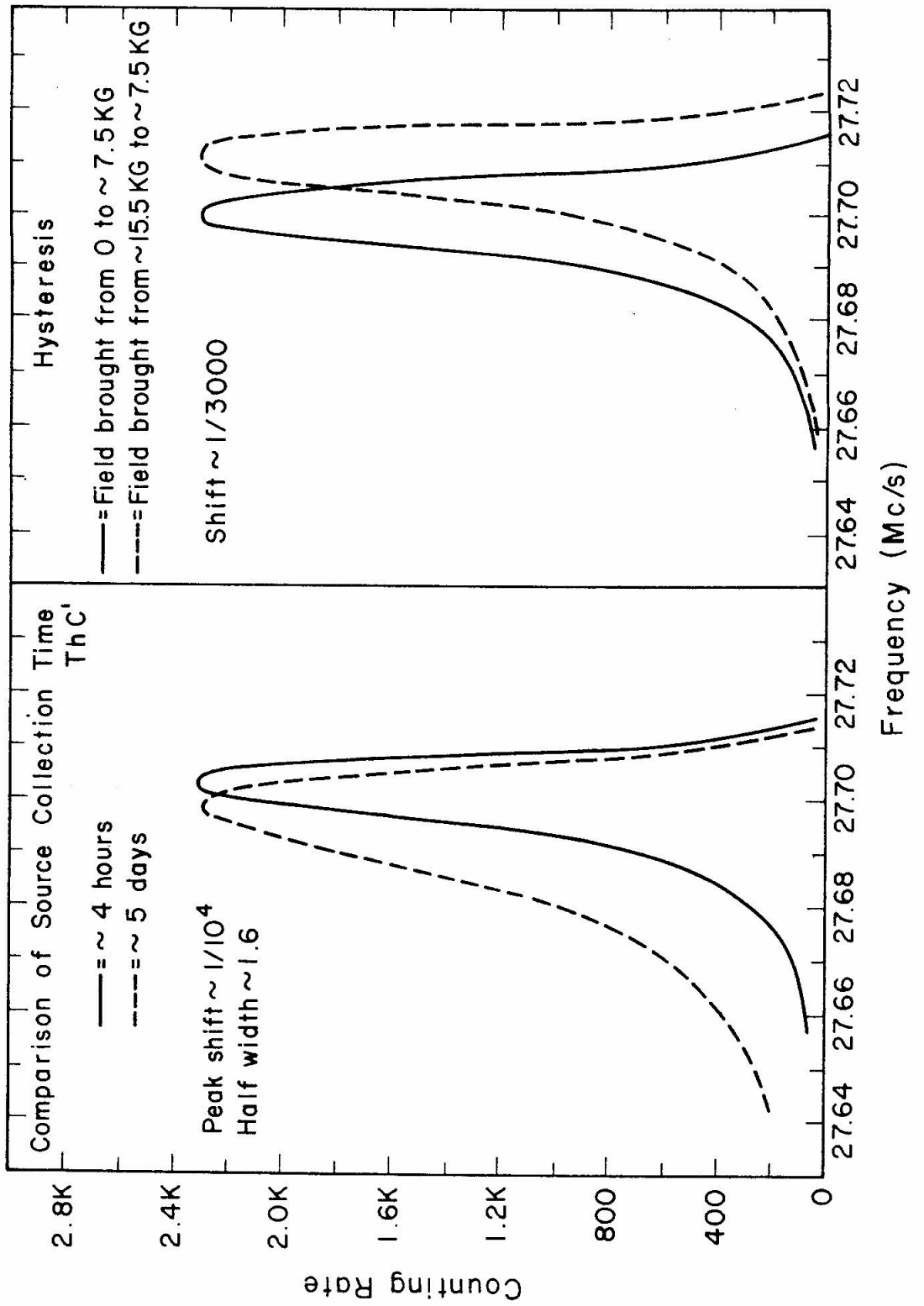


Fig. 29

Figure 30. Calibration Graph.

The energy of various charged particles versus the nuclear magnetic resonance magnetometer frequency reading in megacycles per second is shown. Also given in the magnet current in amperes and the magnetic field of the mean orbit. Note that since the NMR magnetometer is not on the central ray but in a magnetic field lower by about 7 per cent from that on the mean orbit, then for the purposes of calibration, the familiar relation of .235 megacycles per second/kilogauss does not hold. See text: page 34.

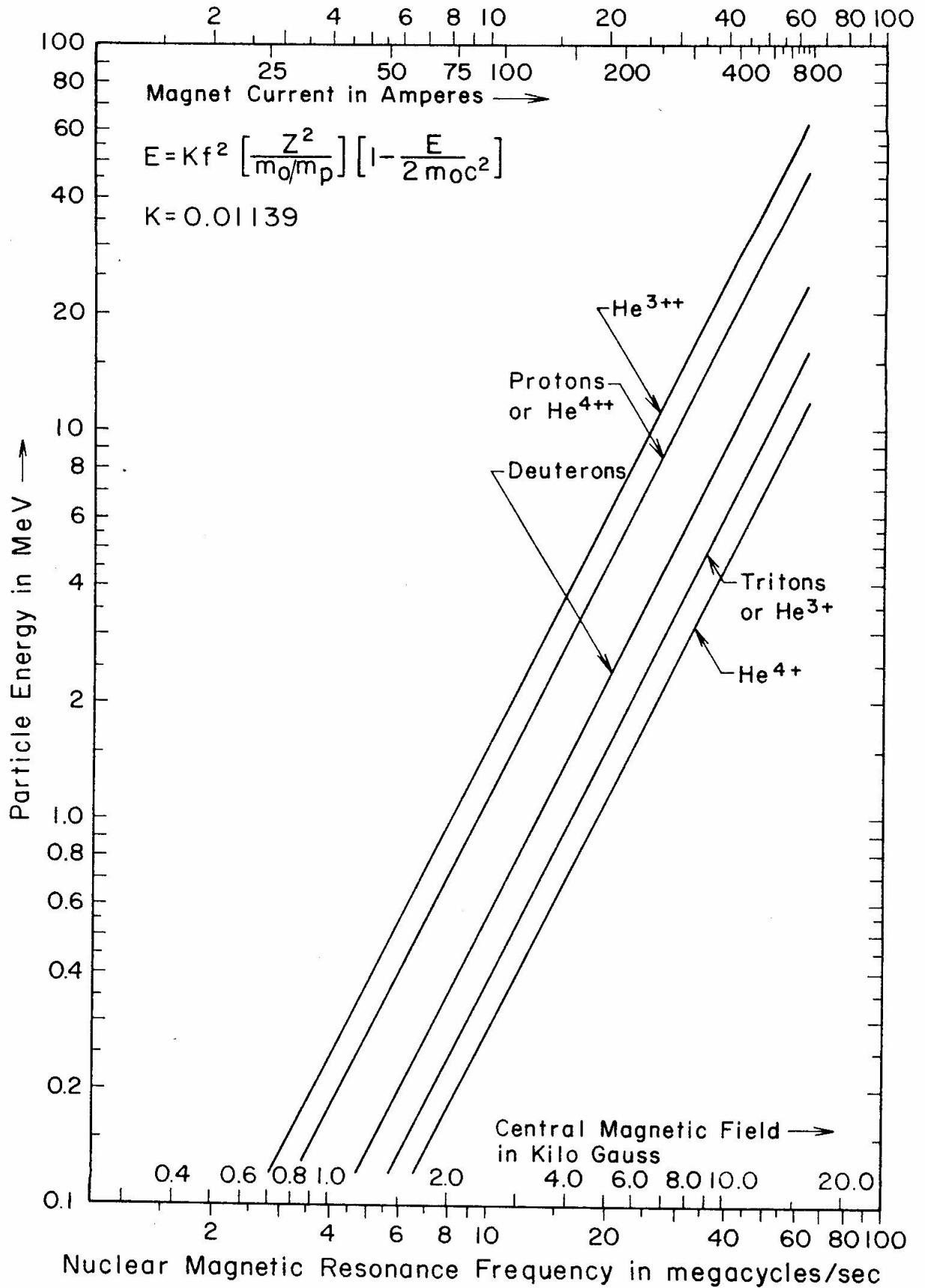


Figure 31. Comparison of Spectra Taken Through Various Portions of the Spectrometer Aperture.

The two sets of curves show the $\text{Th C}'$ spectrum for three different portions of the spectrometer entrance aperture. The first group shows the effects of the detector slit position error. The second shows the spectra with the detector positioned correctly; both the outer apertures should produce spectra that lie at lower frequencies than the spectrum from the middle aperture. This was determined by ray tracing measurements. See text: page 35.

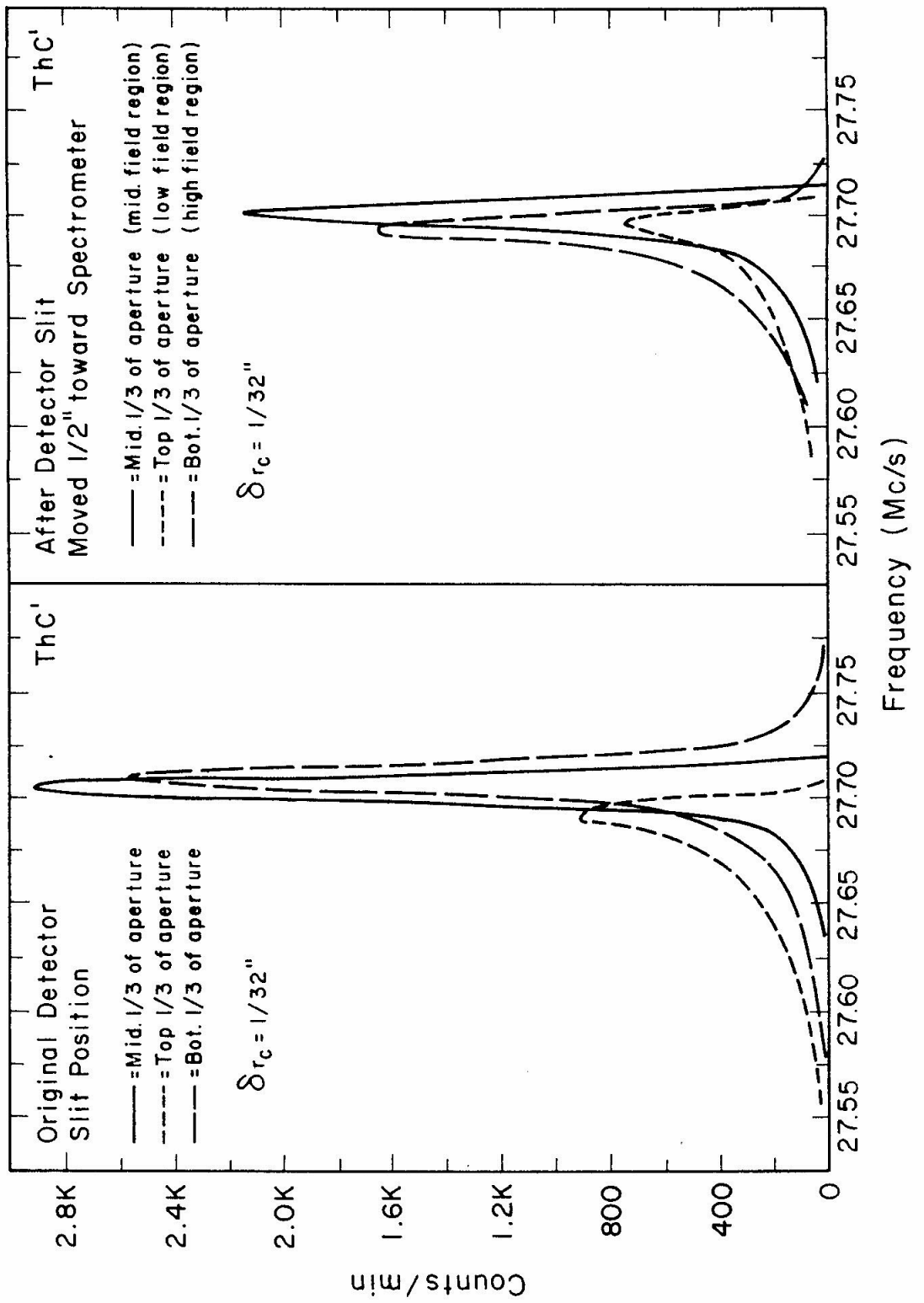


Fig. 31

Figure 32. Comparison of the Θ and Φ Aberrations.

Th C' alpha spectra for various entrance apertures are shown. The short-dashed curve is repeated three times for comparison. The curves at the left show the effect of opening the Θ slits to their maximum. The curve at the right shows the effect of opening the Φ slits to their maximum. From these two curves, the individual contributions to the total aberrations δr may be seen qualitatively. The central curves show the combined effect of both the Θ and the Φ aberrations. Note that the peaks are broadened and shifted. See Table 7 for a quantitative measurement of the aberrations. See text: pages 36 and 37.

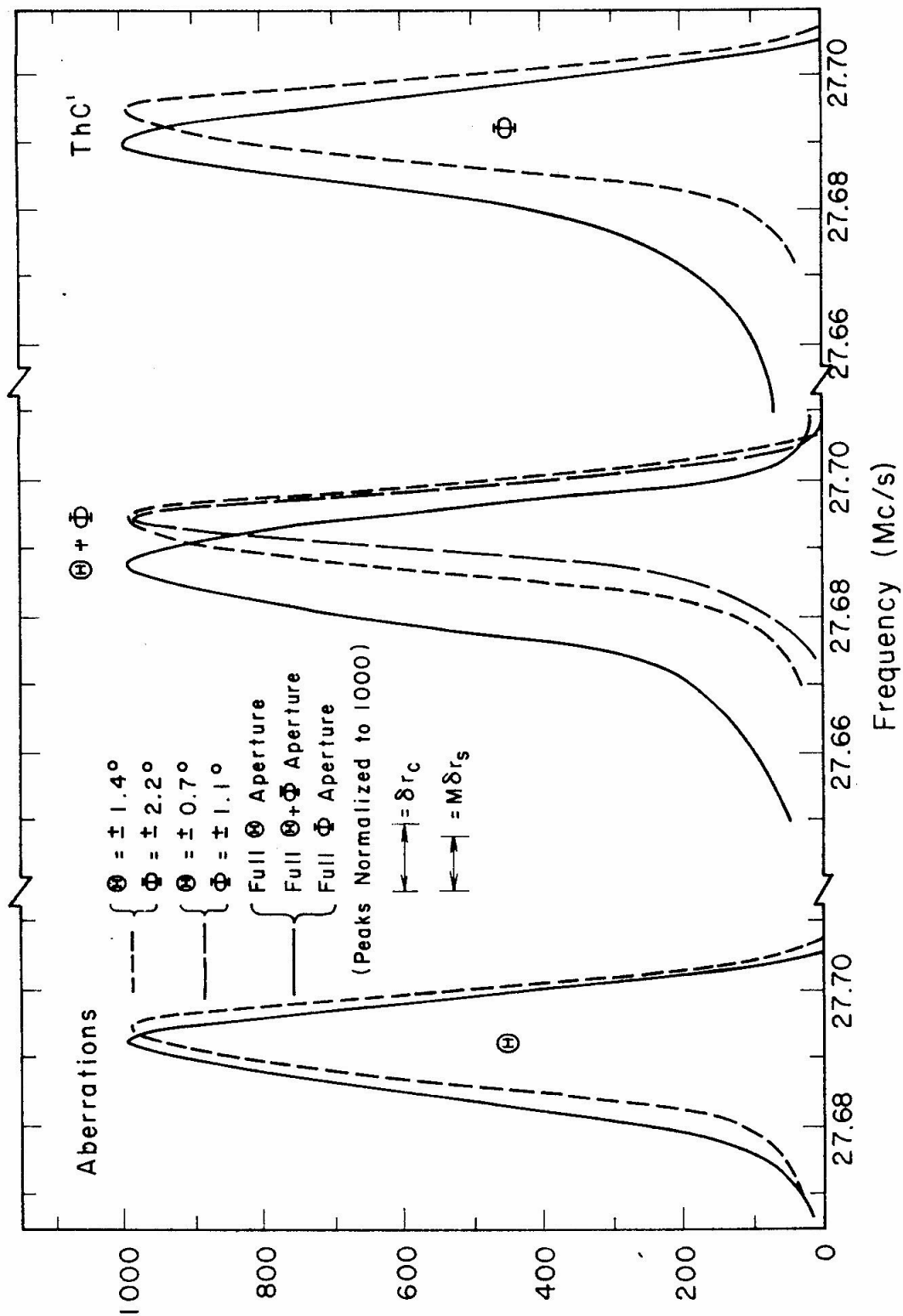


Fig. 32

Figure 33. Elastic Scattering of 4-MeV Protons from Gold.

Three profiles of the front step from the elastic scattering of 4 MeV protons from gold are shown. The various resolutions are shown by an equivalent frequency; the contribution due to the beam spot size $M\delta r_s$ is just one half that of the collector slit size, δr_c . The beam resolution is the upper limit of the resolution as set by the 90° analyzer slits. The Φ slits were closed down in the case of two of the curves; from this, the effects of the aberrations on the resolution is readily apparent. The full width of the slope of the front edge of the profile is shown as an equivalent momentum resolution. See text: page 36.

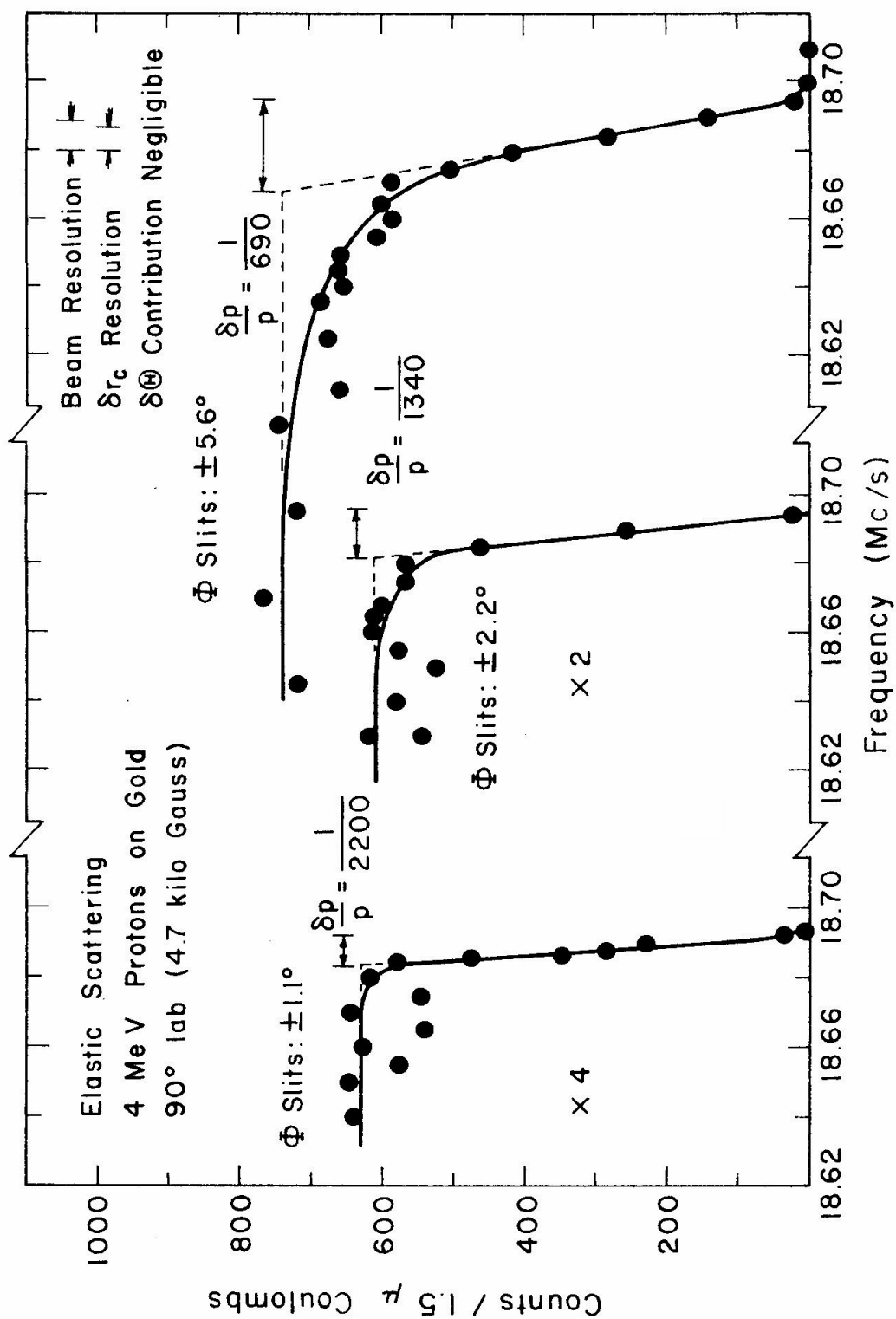


Fig. 33

Figure 34. Elastic Scattering of 10 MeV Protons from Gold.

See Figure 33 for a discussion of these measurements.

See text: page 36.

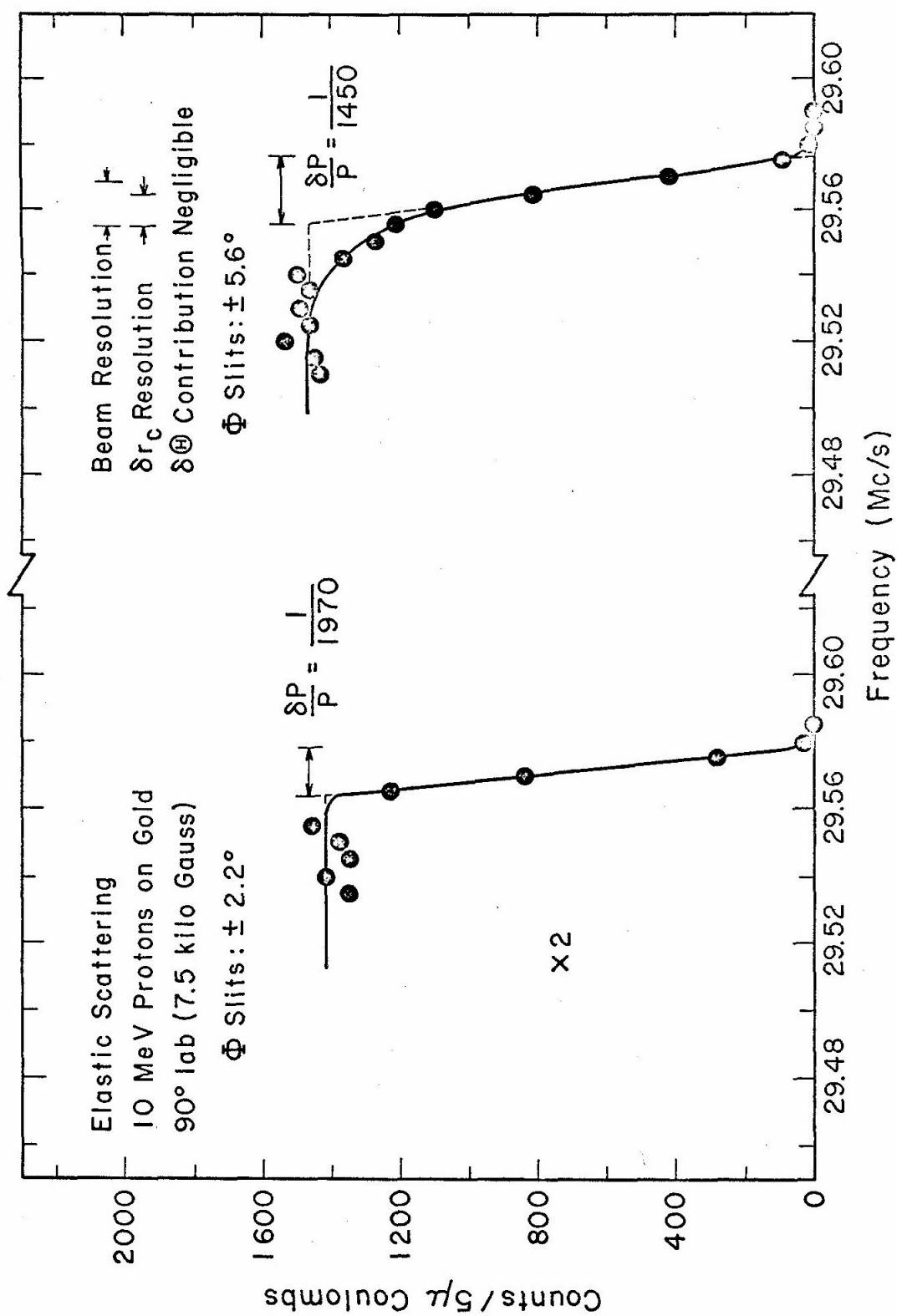


Fig. 34

-117a-

Figure 35. Elastic Scattering of 10-Mev Deuterons from Gold.

See Figure 33 for a discussion of these measurements.

See text: page 36.

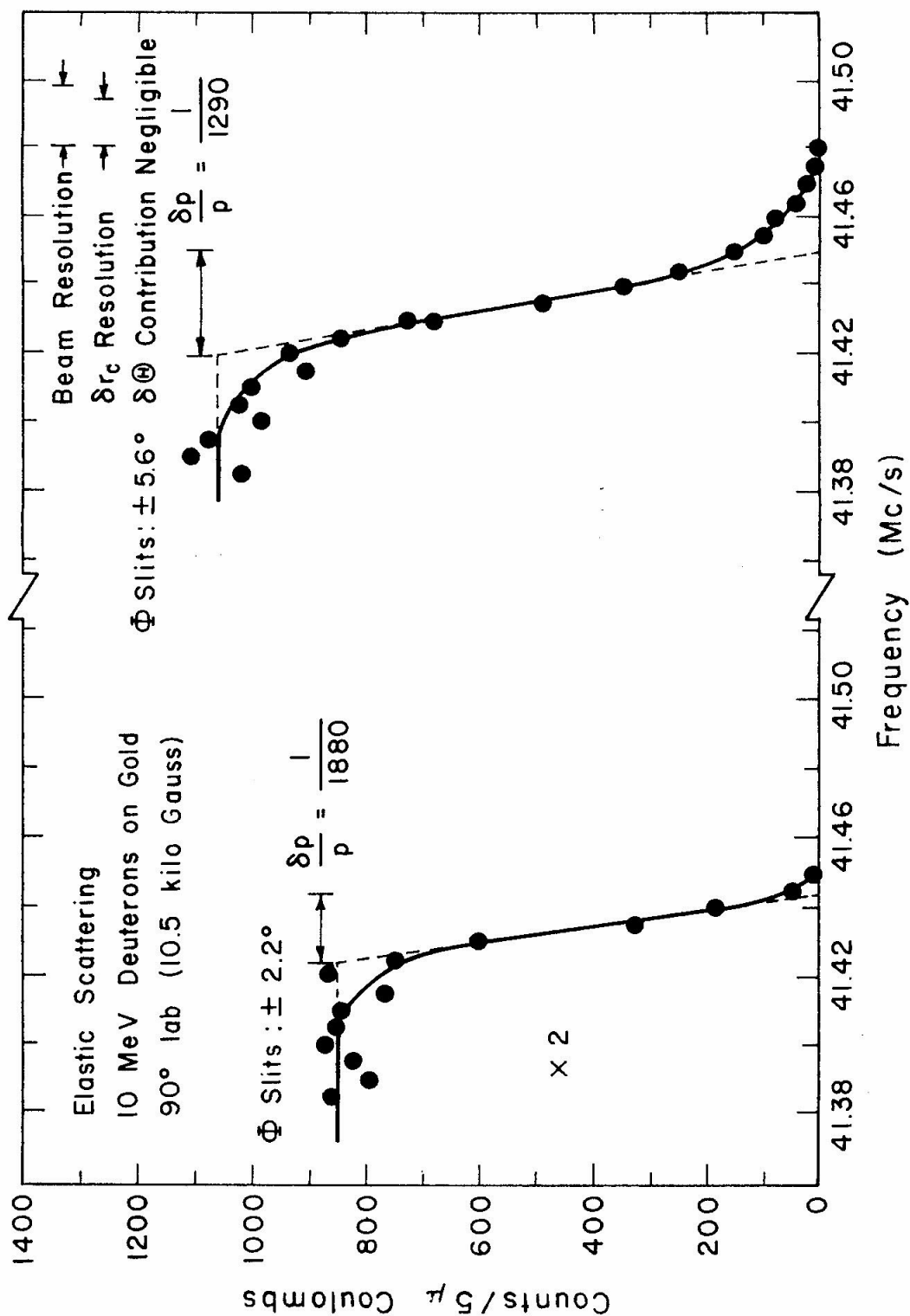


Fig. 35

Figure 36. Isobars: $A = 11$.

Energy level diagrams for three members of the mass 11 isotopic quartet are shown (Ajzenberg-Selove and Lauritsen, 1960). The fourth member, N^{11} , has not been observed experimentally. The energy level diagrams have been shifted relative to each other. This shift was composed of the $(n - H^1)$ mass difference and the coulomb energy difference based on a uniform charge distribution with a radius given by $1.45 A^{1/3}$ fermi. See text: page 41.

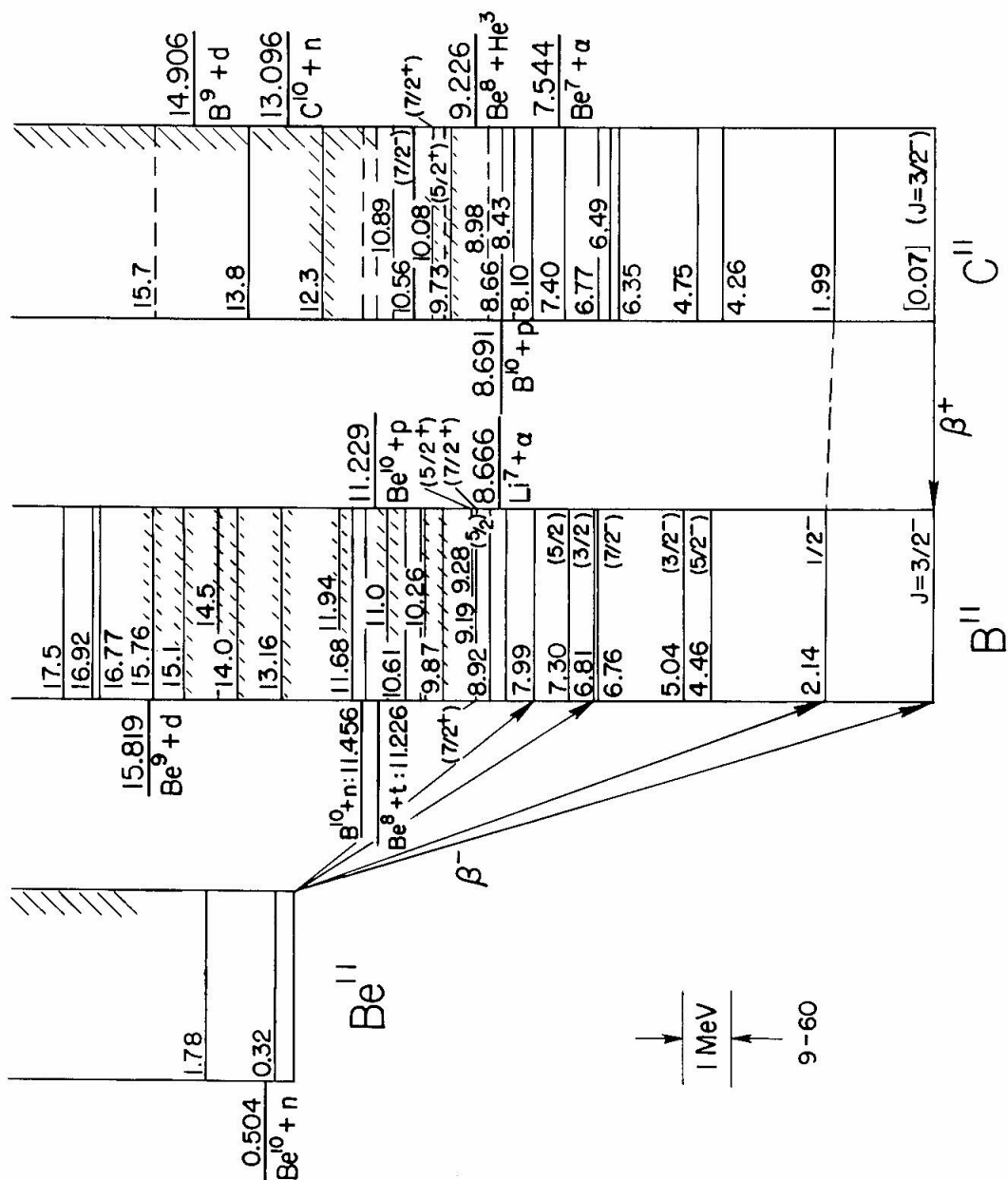


Fig. 36

Figure 37. Energy Level Diagram for B^{11} .

The energy level diagram for B^{11} (Lauritsen and Ajzenberg-Selove, 1962) is shown. Some details not relevant to this experiment have been left out. See text: page 43.

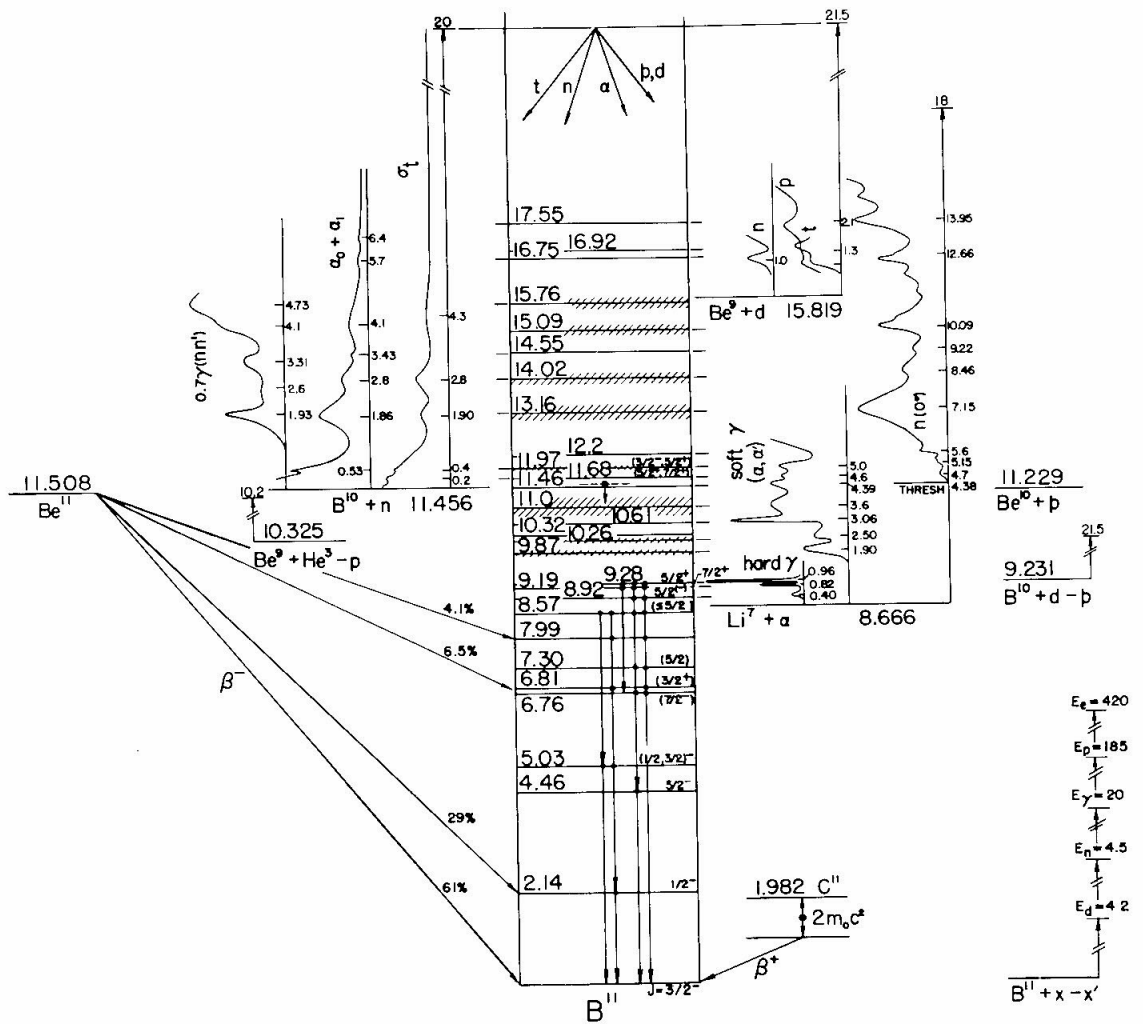


Fig. 37

Figure 38. Proton Momentum Spectrum from $\text{Be}^9(\text{He}^3, \text{p})\text{B}^{11*}$.

A proton momentum spectrum from the reaction $\text{Be}^9(\text{He}^3, \text{p})\text{B}^{11*}$ at 10-MeV He^3 energy and 30° laboratory angle is shown for excitation energies in B^{11} between 8.9 and 14.6 MeV. All identified peaks are labelled with the final residual nucleus and the excitation energy in MeV. The scale of the abscissa is the nuclear magnetic resonance magnetometer frequency; but also the corresponding proton energy is given. See text: page 45.

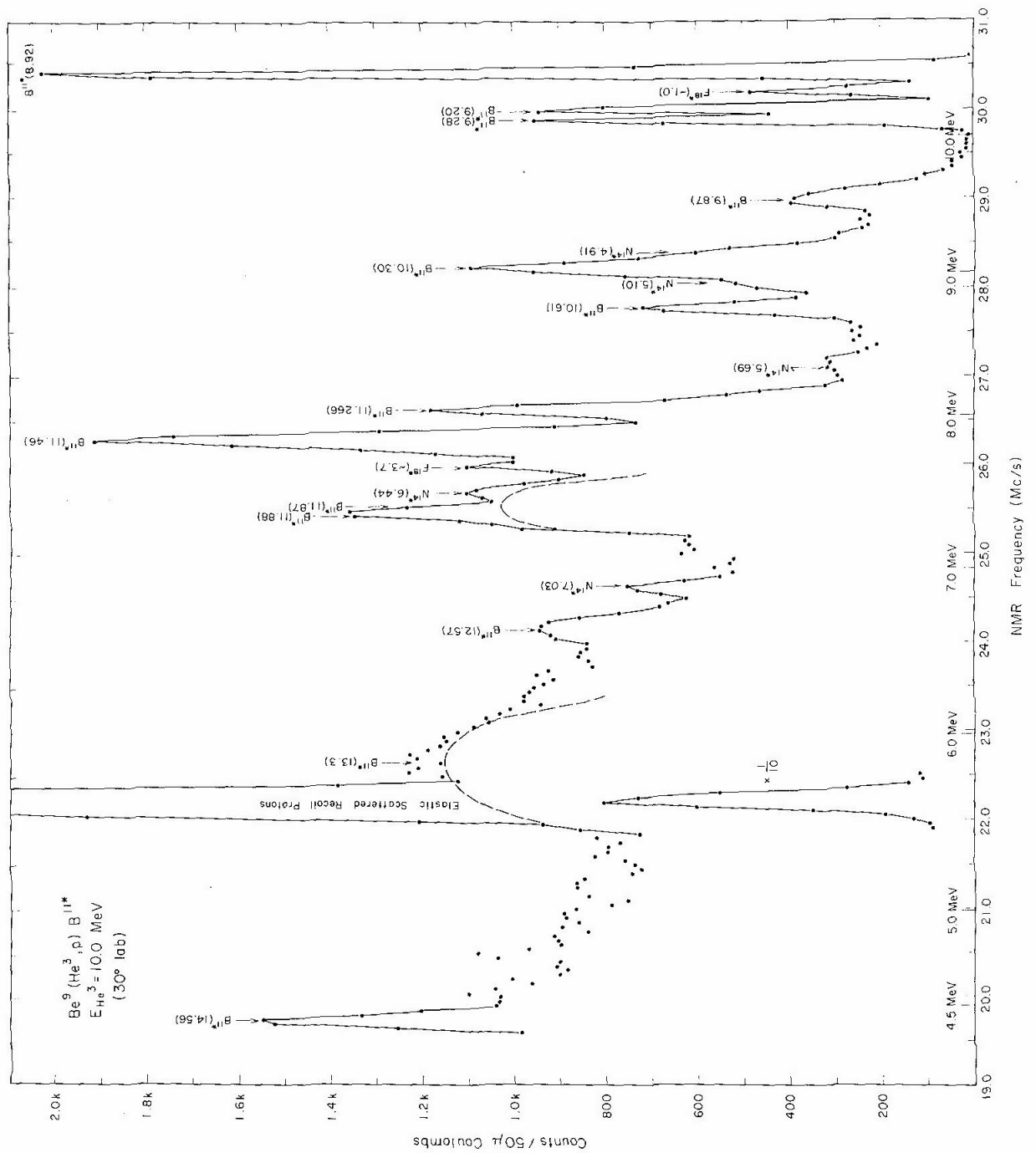


Fig. 38

Figure 39. Comparison of Proton Spectra from $B^{10}(d,p)$ and $B^{11}(d,p)$.

A comparison of the proton momentum spectrum for two different boron targets is shown for 10-MeV deuteron energy at 30° laboratory angle. The target used for the upper spectrum was enriched to 92 per cent in B^{10} . The other target was natural boron (20 per cent B^{10}). The dashed lines under the peak near 23 Mc/s were the assumed background used for the comparison of the two spectra. See text: page 46.

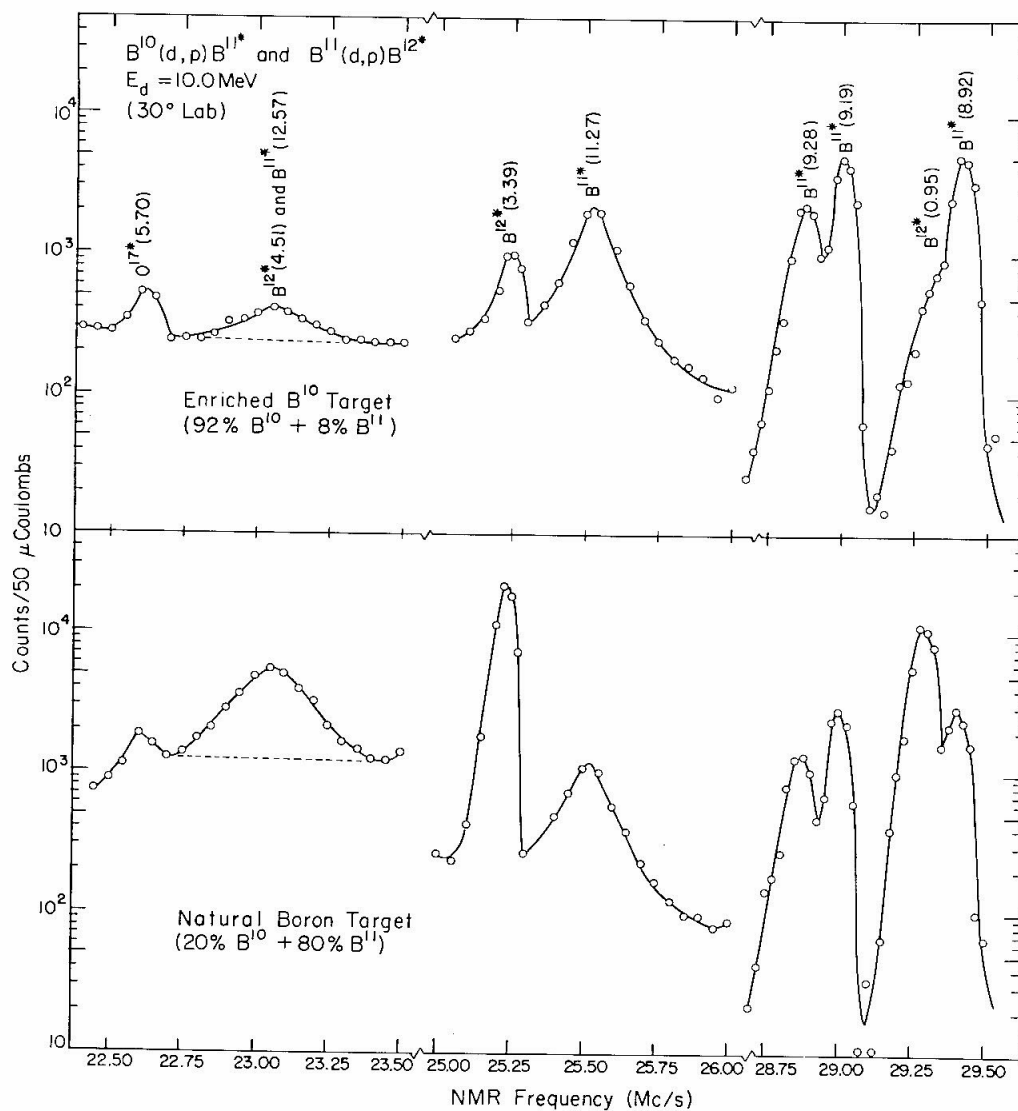


Fig. 39

Figure 40. Energy Level Diagram for Li^6 .

The energy level diagram for Li^6 (Lauritsen and Ajzenberg-Selove, 1962) is shown. Some details not relevant to this experiment have been left out. See text: page 52.

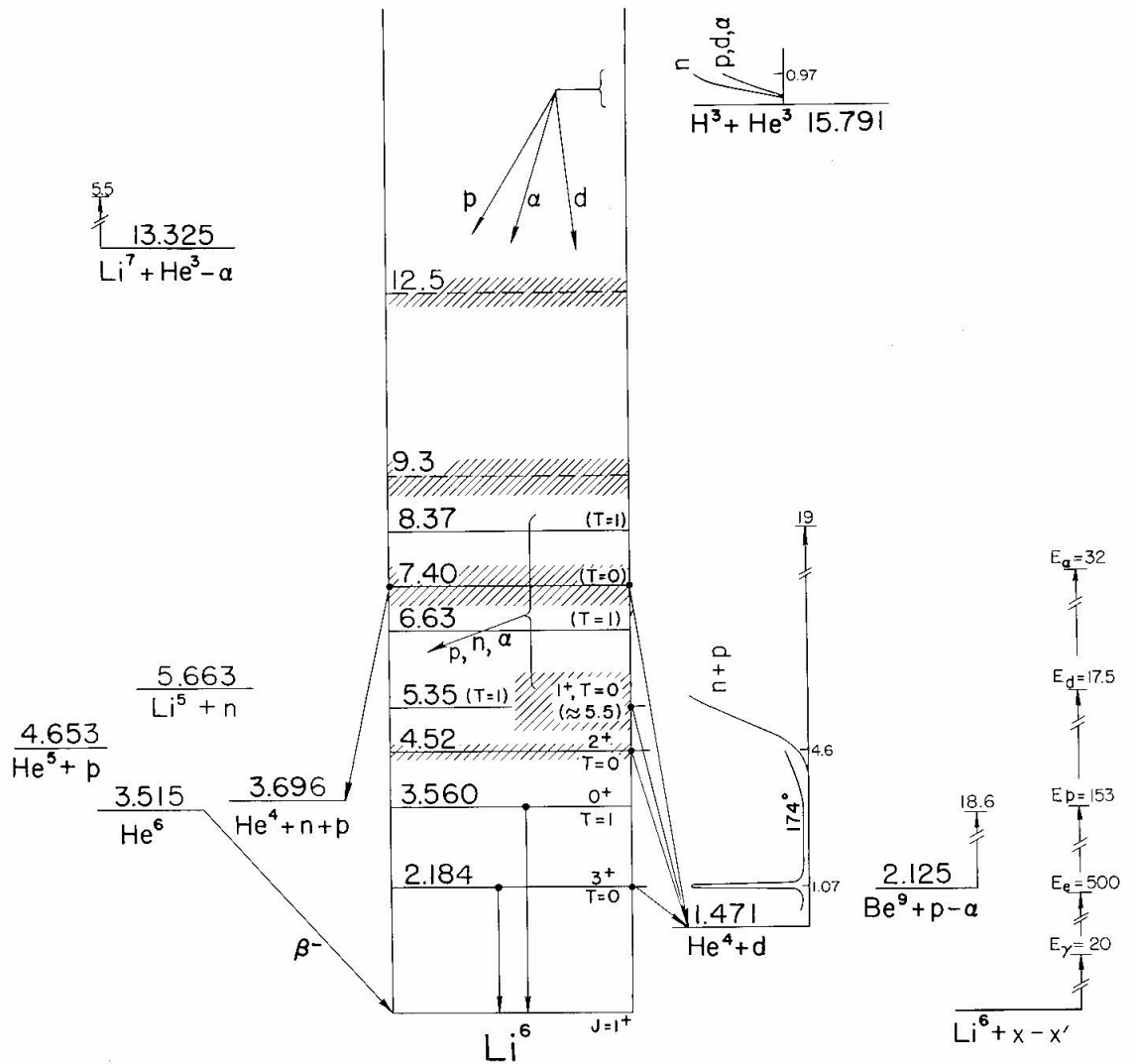


Fig. 40

Figure 41. Alpha-Particle Momentum Spectrum from $\text{Be}^9(p, \alpha)\text{Li}^{6*}$.

An alpha-particle momentum spectrum from the reaction $\text{Be}^9(p, \alpha)\text{Li}^{6*}$ at 10-MeV proton energy and 90° laboratory angle is shown for excitation energies in Li^6 up to 7 MeV. All identified peaks are labelled with the Li^6 excitation energy in MeV as given by Ajzenberg-Selove and Lauritsen (1962). The previously reported state at 6.63-MeV is not observed above the large background from the in-flight breakup of Li^{6*} , Be^8 , Be^{9*} , and B^{9*} . The scale of the abscissa is the nuclear magnetic resonance magnetometer frequency, but also the corresponding alpha particle energy is given. See text: page 53.

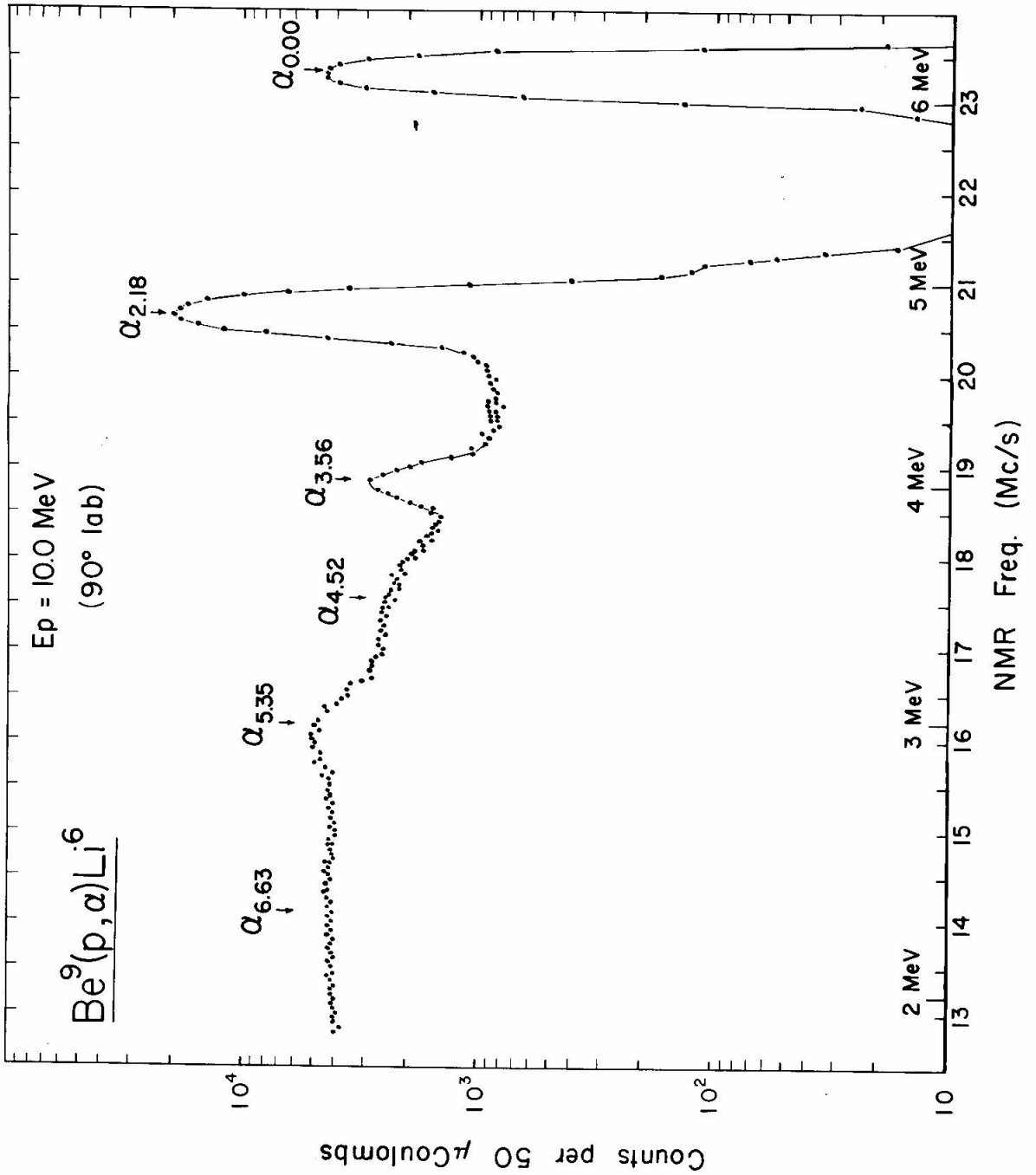


Fig. 41

Figure 42. Alpha-Particle Momentum Spectrum from
 $\text{Be}^9(p, \alpha)\text{Li}^{6*}$.

An alpha-particle momentum spectrum from the reaction $\text{Be}^9(p, \alpha)\text{Li}^{6*}$ at 10-MeV proton energy and 30° laboratory angle is shown for excitation energies in Li^6 up to 10 MeV. All identified peaks are labelled with the Li^6 excitation energy in MeV as given by Ajzenberg-Selove and Lauritsen (1962). None of the previously observed states above 6-MeV excitation are seen above the large background from the in-flight break-up of Li^{6*} , Be^8 , Be^{9*} , and B^{9*} . The broad peak near 14.5 Mc/s is elastic scattered Be^{9+++} recoils. For the purposes of determining Q-values and widths, the background was assumed as in the dashed lines under the states at 4.5 and 5.4 MeV. The scale of the abscissa is the nuclear magnetic resonance magnetometer frequency, but also the corresponding alpha particle energy is given. See text: page 53.

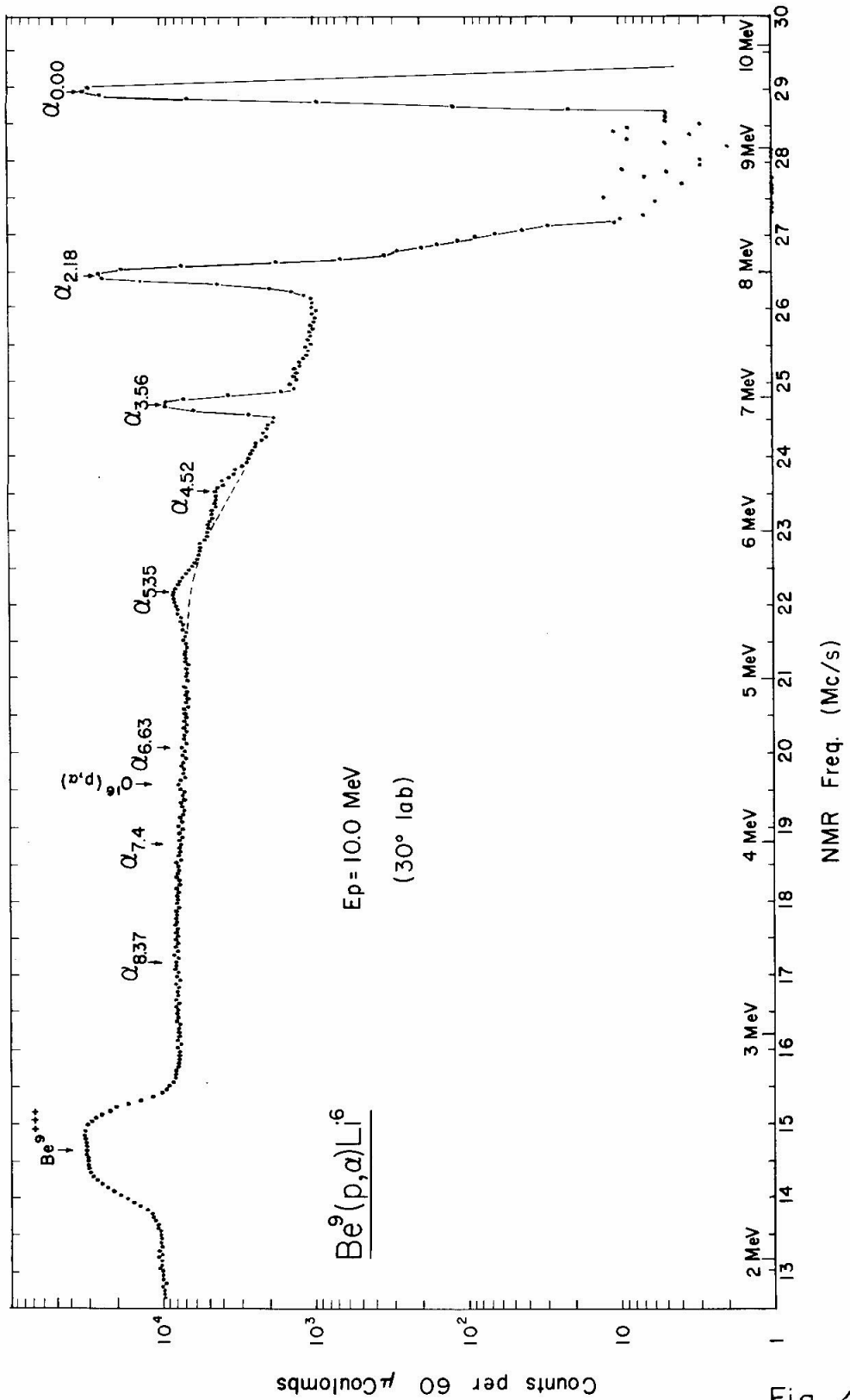


Fig. 42

Figure 43. Total Particle Spectrum from Be^9 Plus Protons.

A momentum spectrum of all the particles detected at the image of the spectrometer from 10-MeV protons on Be^9 at 30° laboratory angle is shown. All identified peaks are labelled with the contributing reaction and the excitation energy of the residual nucleus in MeV. The scale of the abscissa is the nuclear magnetic resonance magnetometer frequency in Mc/s. See text: page 53.

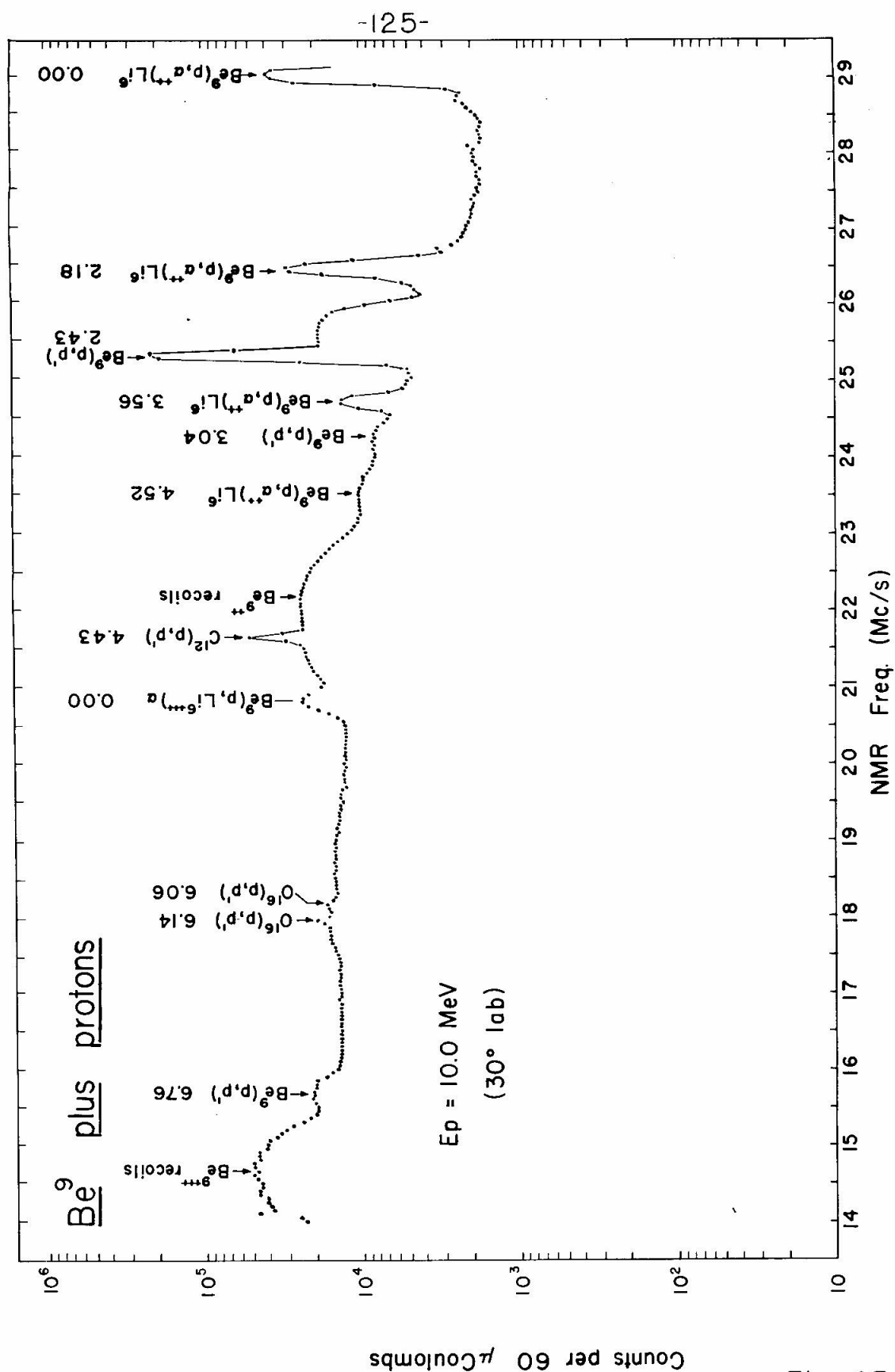


Fig. 43

Figure 44. Three-Body Decay from Be^9 Plus Protons.

A velocity vector diagram for the breakup of B^{10*} into two alpha particles and a deuteron through three intermediate processes is shown. Each decay will produce the three particles at the same laboratory angles and with the same energies. The numerical values were chosen so that $(\text{Li}^{6*})_1$ has 5.36-MeV excitation and that the alpha particles were observed at 20° and 90° laboratory angles. See the text for a complete discussion of this figure (page 55).

THREE BODY DECAY

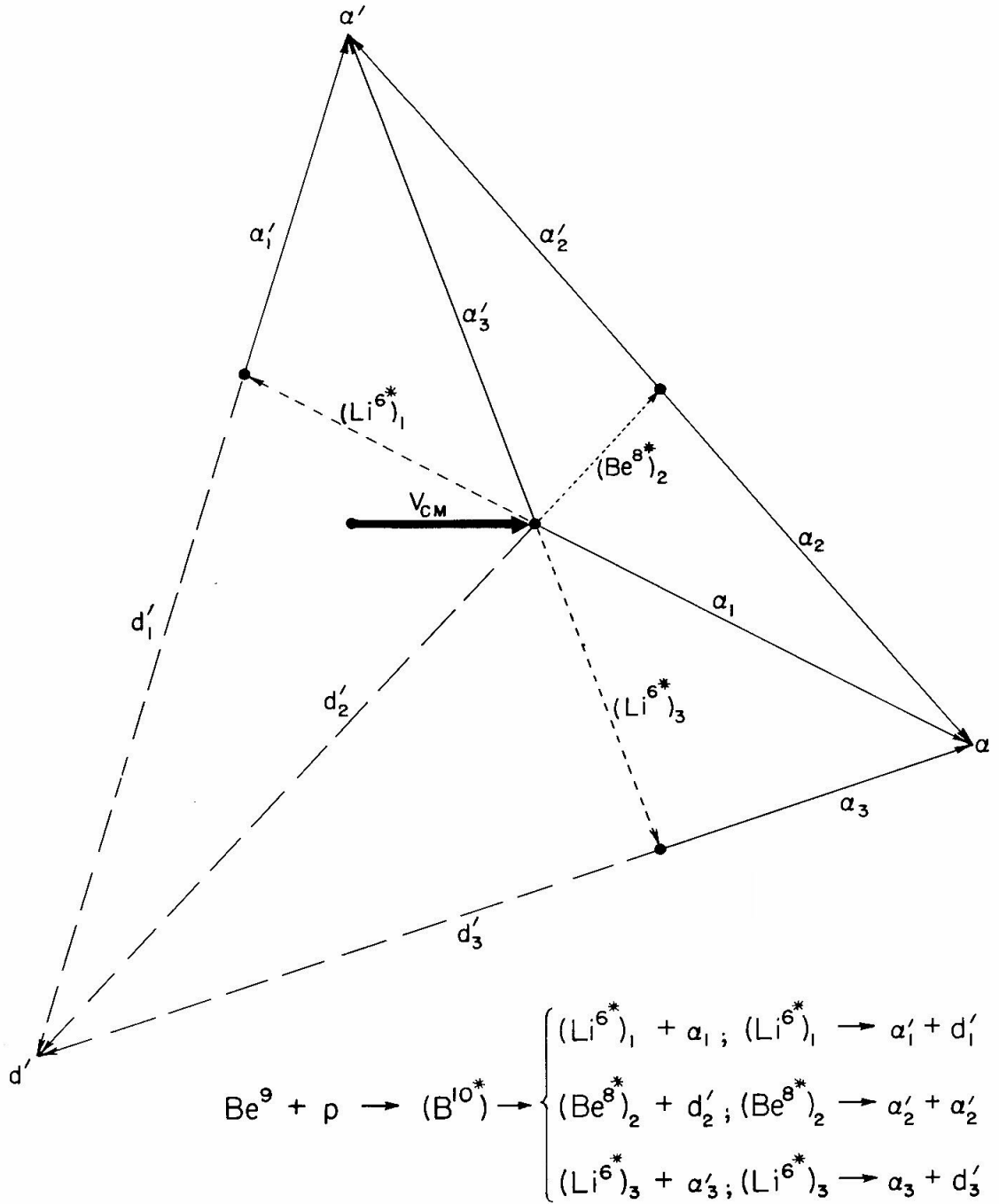


Fig. 44

Figure 45. 180° Reactions.

A preliminary analysis of the possibility of observing charged particle reactions at angles near 180° is shown for the case where the analyzed rigidity is 1.4 times the incident rigidity. From the fringing field measurements on the 16-inch radius magnetic spectrometer, an estimate was made of the fringing field expected on the 24-inch radius spectrometer. The beam could enter through the back of the spectrometer and be bent into the target at various angles depending on the initial angle and position. A bending magnet could be placed at the approximate focus to accomplish this. See Appendix 3.

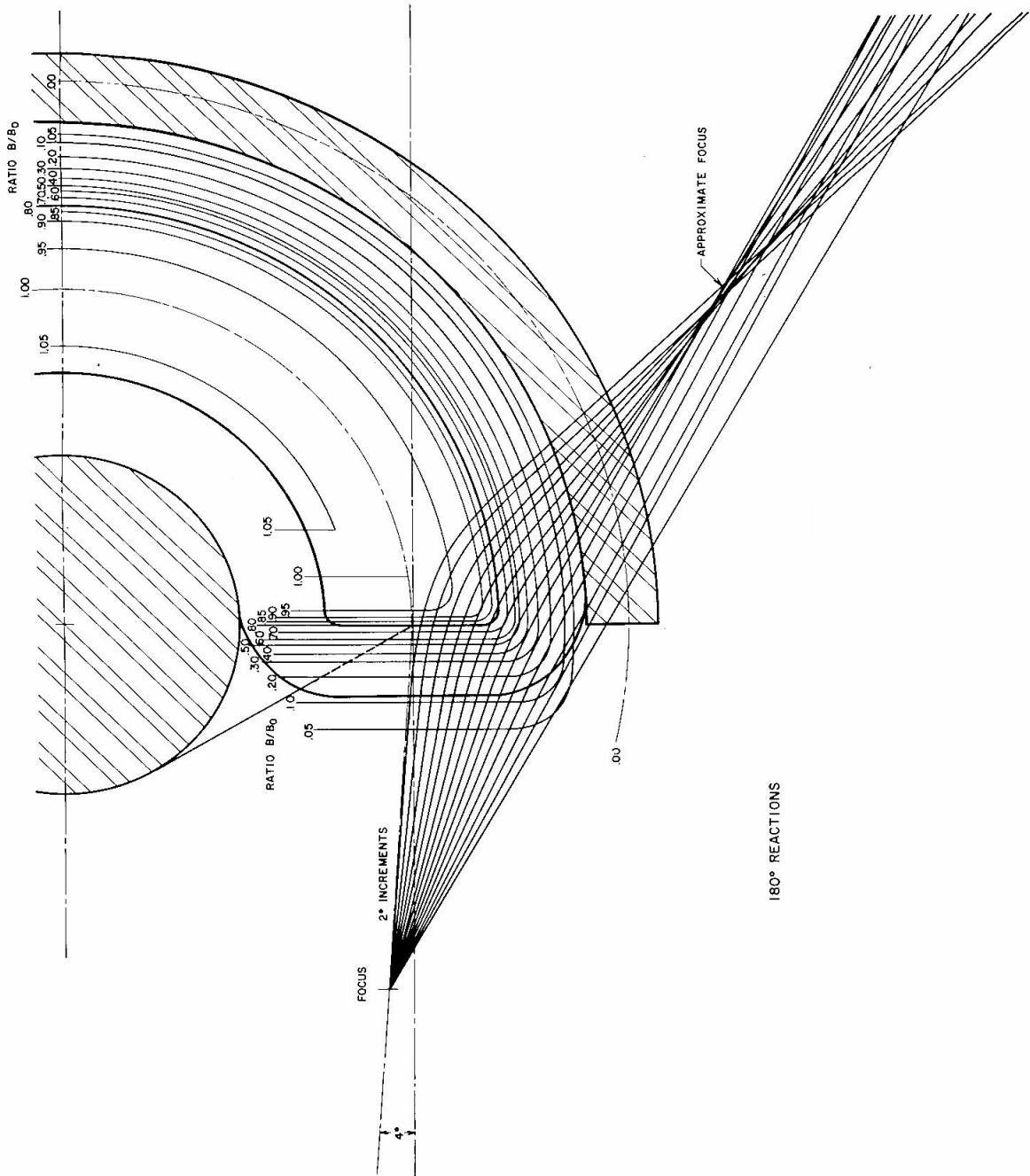


Fig. 45